Aus dem Max-Planck-Institut für Kolloid- und Grenzflächenforschung

Thin Liquid Films with Nanoparticles and Rod – Like Ions as Models for Nanofluidics

Dissertation
zur Erlangung des akademischen Grades
”doctor rerum naturalium”
(Dr. rer. nat.)
in der Wissenschaftsdisziplin ”Physikalische Chemie“

eingereicht an der
Mathematisch – Naturwissenschaftlichen Fakultät
der Universität Potsdam

von
Silke Stöckle
geboren am 30.05.1979 in Karlsruhe

Potsdam, den 12. Mai 2010

This work is licensed under a Creative Commons License:
Attribution - Noncommercial - Share Alike 3.0 Germany
To view a copy of this license visit
http://creativecommons.org/licenses/by-nc-sa/3.0/de/

Published online at the
Institutional Repository of the University of Potsdam:
URL http://opus.kobv.de/ubp/volltexte/2010/4637/
URN urn:nbn:de:kobv:517-opus-46370
http://nbn-resolving.org/urn:nbn:de:kobv:517-opus-46370

TABLE OF CONTENTS

TABLE OF CONTENTS i

ACKNOWLEDGEMENTS iv

LIST OF ABBREVIATIONS AND SYMBOLS v

1 INTRODUCTION 1

2 SCIENTIFIC BACKGROUND 4

2.1 Liquid / Gas Interfaces 4

2.1.1 Introduction 4

2.1.2 Surface Tension 4

2.1.3 Adsorption to Liquid / Gas Interfaces 5

2.1.4 Adsorption Isotherms 5

2.1.5 Diffusion 6

2.1.6 Surface Active Agents (Surfactants) 7

2.1.7 Charges at Liquid / Gas Interfaces 8

2.2 Interfacial Forces 8

2.2.1 Introduction 8

2.2.2 Repulsive Electrostatic Forces 8

2.2.3 Van der Waals Dispersion Forces 11

2.2.4 DLVO Theory 12

2.3 Thin Liquid Films 13

2.3.1 Structure 14

2.3.2 Capillary Pressure 14

2.3.3 Film Thickness 15

2.3.4 Film Stability and Rupture Mechanisms 16

2.4 Fluid Dynamics 17

2.5 Nanoparticles Confined in Thin Liquid Films 19

3 METHODS AND MATERIAL CHARACTERIZATION 21

3.1 Experimental Methods 21

3.1.1 Microinterferometric Thin Liquid Film Analysis 21

3.1.2 Neutron Reflectometry 23

3.1.3 Grazing Incidence Small – Angle X – Ray Scattering 26

3.1.4 Tensiometry 28
3.1.5 Transmission Electron Microscopy 28
3.1.6 Dynamic Light Scattering 29
3.2 Stability Study of Particle Dispersions 30
3.2.1 Motivation 30
3.2.2 Stability (Short Term) 31
3.2.3 Stability (Long Term) 32
4 RESULTS AND DISCUSSION 34
4.1 Thin Liquid Films in Nanofluidics – Dynamics of Thinning of Films from the Non – Ionic Surfactant $\beta - C_{12}G_2$ 34
4.1.1 Introduction 34
4.1.2 Characterization of the Film Forming Solution 34
4.1.3 Dynamics of Thinning 35
4.1.4 Theoretical Approach to Analyze the Thinning of TLFs 36
4.1.5 Fitting Results 39
4.1.6 Interpretation of the Diffusion Coefficient according to the Free Volume Model 44
4.1.7 Conclusions 45
4.2 Effect of Ionic Geometry on the Force Balance (Stability) in Thin Liquid Films 46
4.2.1 Introduction 46
4.2.2 Stability and Equilibrium of TLFs from $\beta - C_{12}G_2$ and Ions 47
4.2.3 Classical Theory on Film Stability and Critical Rupture Thickness 54
4.2.4 Activation Energy E_a and Energy for Hole Nucleation 56
4.2.5 Influence of Yttrium Chloride (YCl_3), another Trivalent Ion on the Transition CF / NBF 57
4.2.6 Influence of the Sign of the Charge of the Film Surfaces on the Electrostatic Action of Spermidine Ions 58
4.2.7 Conclusions 60
4.3 Nanosized Particles in Aqueous Free Standing Thin Liquid Films: Fluid Dynamics and Structure 62
4.3.1 Introduction 62
4.3.2 Influence of Particles on Film Interfaces 63
4.3.3 Dynamic Conditions of Dispersions in Nano Confined TLFs 65
4.3.4 Quantitative Analysis of Outflow 68
4.3.5 Static Conditions 72

4.3.6 Conclusions 73

4.4 Preliminary Results to the Structure of Free Standing Liquid Films from β – $C_{12}G_2$ Containing Fe_3O_4 Nanoparticles using Neutron Reflectometry (NR) and Grazing Incidence Small Angle X – Ray Scattering (GISAXS) 75

4.4.1 Introduction 75

4.4.2 Profile analysis of complex foam films via Neutron Reflectometry 75

4.4.3 Study of In – plane Structure and Arrangement of Particles via Grazing Incidence Small Angle X – Ray Scattering (GISAXS) 79

5 SUMMARY AND OUTLOOK 83

6 EXPERIMENTAL DETAILS 86

6.1 Solvents, Surfactants, Ions, Materials 86

6.1.1 Overview 86

6.1.2 Solvents 86

6.1.3 Surfactants 87

6.1.4 Ions 87

6.1.5 Preparation of Solutions and Dispersions 87

6.2 Methods 88

6.2.1 Microinterferometric Thin Liquid Film Analysis 88

6.2.2 Neutron Reflectometry 89

6.2.3 GISAXS 89

6.2.4 Tensiometry 89

6.2.5 TEM 90

6.2.6 DLS 90

7 DEUTSCHE ZUSAMMENFASSUNG 91

LITERATURE 93

ACKNOWLEDGEMENTS

It's a pleasure to thank those who made this thesis possible. First of all I want to express my gratitude to Prof. Dr. Helmuth Möhwald for his scientific guidance and financial support. I would like to thank my supervisor Dr. Rumen Krastev for sharing his scientific routine and creativity with me in innumerable discussions. I much appreciated getting to know the person behind the scientist and drifting off into political discussions.

I am indebted to many of my colleagues to support me, especially thanks to all members of the "Thin Soft Films" group, Marta Kolasinska, Ralf Köhler, Pedro Blecua, Jeni Blacklock, Liu Xin, Dmitry Volodkin, Jiangshan Chen, and Johannes Früh (the kid) for inspiring scientific and cultural discussions. Special thanks to our frequent guest Ass. Prof. Dr. Klemen Bohinc, who introduced us to the idea of ion – bridging and to Pedro Blecua for developing the fitting routine used in this work.

Without the following colleagues, who provided assistance in numerous ways, this work would not have been possible. First I would like to thank the heart and soul of our lab, Renate Emrich. For preparation of the glass cells I would like to thank Cliff Janiszewski. Thanks to the mechanical workshop, especially to Andreas Kretschmar and Marco Bott for professional preparation of experimental equipment. Todor Krastev is acknowledged for the algorithm for film thickness measurements and Irina Berndt for support during lab courses. Thanks to Heidemarie Zastrow for DLS measurements and discussion and to Rona Pitschke and Munish Chanana for TEM measurements. Thanks to Gerald Brezesinski and Dimitri Grigoriev for discussion about oleic acid and oleic acid stabilized particles. Dr. Jan Perlich, Dr. Jean – Francois Moulin and Prof. Dr. Müller – Buschbaum are acknowledged for support during GISAXS measurements and analysis, Dr. Thomas Gutberlet and Dr. Andrew Wildes for supporting during Neutron Reflectometry experiments.

I would like to thank all those colleagues especially who created such a great working atmosphere at MPI: Nicole, Ali, Anja, Ana, Anna, Annabelle, Antje, Antonio, Audrée, Caro, Cécile, Clara, Claudia, Clemens, Conny 1-3, Daria, Dirk, Dmitri, Doro, Hans, Ingo, Janos, Janina, Jeni, Jens, Jörg, John B&D, Juan, Julia, Laura, Madeleine, Magda, Marc, Marco, Marta, Matt, Micha, Michelle, Mihaela, Munish, Nick, Pedro, Ralf, Reni, Rocio, Ruben, Sasha, Stefan, Stefanie, Steffi, Stephan, Tanja, Tatjana, The Thorstens, Torsten, Vasana, Veneta, Virginia, Viviane, Vroni, Yael, Yaru, Xin
I am glad that some colleagues became very good friends, so that MPI-KGF will surely find its niche in my future life, not only in my memories.

LIST OF ABBREVIATIONS AND SYMBOLS

ABBREVIATIONS

$\beta - C_{12}G_2$	n – Dodecyl β – D – Maltoside
CF	Common Film
CBF	Common Black Film
CTAB	Cetyl Trimethyl Ammoniumbromide
DLS	Dynamic Light Scattering
DLVO	Derjaguin – Landau – Verwey – Overbeek
Fe_3O_4	Magnetite
GISAXS	Grazing Incidence Small Angle X – Ray Scattering
IF	Interface
NaCl	Sodium Chloride
NBF	Newton Black Film
NR	Neutron Reflectometry
OA	Oleic Acid
PDI	Polydispersity Index
PTFE	Polytetrafluorethylen
Ref	Reference
SLD	Scattering Lengt Density ($\equiv N_b$)
TEM	Transmission Electron Microscopy
TLF	Thin Liquid Film
YCl_3	Yttrium (III) Chloride

SYMBOLS (A-I)

A	Area
A_H	Hamaker Constant
a	Langmuir Adsorption Constant
a_f	Effective Mean Free Area
$\bar{a}$	Average Molecular Area
a_0	Minimum Required Area per Surfactant Molecule
b	Fitting Parameter – Bulk
c	Concentration
cmc	Critical Micellar Concentration
d	Layer Thickness
D_b	Bulk Diffusion Constant
D_s	Surface Diffusion Constant
E_a	Activation Energy
e	Elementary Charge
F	Force
G	Gibbs' Free Energy
h	Film Thickness
h_{cr}	Critical Film Thickness
h_s	Fitting Parameter – Surface
h_w	Equivalent Film Thickness
I	Intensity
I_B	Ionic Strength

SYMBOLS (J-Z)

j_b	Bulk Diffusion Flux
j_c	Convective Flux
j_s	Surface Diffusion Flux
k	Wave Vector
k_B	Boltzmann Constant
L	Perimeter of Wilhelmy Plate
N_A	Avogadro Constant
N_b	Scattering Lengt Density (SLD)
n	Refractive Index
P_c	Capillary Pressure
P_{ext}	External Pressure
q	Wave Vector Transfer
R	Gas Constant
R_f	Radius of Thin Liquid Film
R_c	Radius of Glas Capillary
T	Temperature
v_s	Surface Velocity
V_{Re}	Reynolds' Velocity
x	Distance
z	Valency
Z	Reflectivity
Z_{ave}	Intensity Dependent Hydrodynamic Diameter
$\varnothing$	Diameter

GREEK SYMBOLS

α_i	Angle of Incidence (X – Ray)
Γ	Surface Excess
δ	Number Density
ε	Dielectric Constant
ε_0	Dielectric Constant of Vacuum
η	(Dynamic) Viscosity
θ	Contact Angle
θ_i	Angle of Incidence (NR)
φ	Double Layer Potential
φ_0	Surface Potential
φ_m	Midplane Potential
κ^{-1}	Debye Length
λ	Wavelength
λ_B	Bjerrum Length
μ	Chemical Potential
Π	Disjoining Pressure
Π_{el}	Electrostatic Double Layer Component of Π
Π_{vdW}	van der Waals Component of Π
σ	Surface Tension
τ_{sp}	Transition Time
ϑ	Volume Fraction of Dispersed Phase
ψ	Out – Of – Plane Scattering Angle

1 INTRODUCTION

The field of microfluidics was developed in the 1990s and has since been path leading in different disciplines of science and engineering. Major advances of this technology were achieved by downscaling microfluidic devices. Downscaling increases the surface to volume ratio of the channel geometry, which in turn introduces major physical changes to flow dynamics. This allows for adjusting the geometry dependent physical properties in order to suit the needs for scientific and industrial applications. For example lab – on – a – chip devices rely on the laminar flow regime and on preset wetting properties of the micro – channels to guide the liquid flow [1].

From the beginning of the 21st century, major advances in nano – technology, have permitted the downscaling of fluid channels to nanometer dimensions. In addition to the development of nano – fabrication technologies, analytical tools have also improved and observations of nanometer flow regimes have become possible [2]. As a consequence, the term “nanofluidics” emerged, describing “the study and application of fluid flow in and around nano – sized objects“ [3]. Nanofluidics research has always been part of fundamental interface science. Fluid interfaces and wetting properties have proven to be of vital importance for nearly all modern technologies with impact on the natural sciences, medicine and engineering [3]. The perspectives and potential of nanofluidics lie in creating high – performance nanofluidic devices, which stick out due to their size, operating and economic efficiency. Limits to nanofluidics in the nearer future can be seen in the remaining technological limits and that fundamental aspects of the complex research field are still not explained, thus, more studies on nanofluidic systems are necessary [2].

Nanofluidic processes in nature, like intracellular fluid flow or flow through capillaries, are characterized by fluid flow between non – rigid interfaces. One important question is, how the mobility of the interfaces determines the fluid flow and if it affects the stability of the nano – channel. Moreover, natural aqueous systems are very complex, e.g. the effect of charged or differently shaped colloids is far from being completely understood. Interesting questions arise with regards to the confinement of such complex fluidic systems how the size, shape and charge of the colloids influence the systems.

A systematic study of nanofluidic processes requires designing experimental nano – channels with precise interfacial characteristics. Liquid and gaseous interfaces (IFs) are well known for purity and lack of defects, therefore the present work employs

thin liquid films (TLFs) as experimental models. They have proven to be useful experimental tools because of their simple geometry, reproducible preparation, and well defined interfaces [4]. Thin liquid films offer the possibility to confine differently shaped ions and molecules to very small spaces, or to subject them to controlled forces. The TLF experimental system gives the possibility to deal with various particle and ion concentrations. This allows us to imitate a number of biological conditions, for example intracellular processes, like the condensation of DNA, or transport mechanisms through biological cell wall channels. To study the underlying phenomena of such processes, requires evaluating how closely we can imitate natural nanofluidic systems with TLFs and that studying the properties of TLFs reveals confinement effects in fluid systems.

In order to understand the impact of fluid IFs on liquid flow in nano – confinement, the dynamics of thinning of aqueous TLFs are studied in the first part of this work using a micro – interferometric method. The films are stabilized with different concentrations of the non – ionic surfactant $\beta - C_{12}G_2$, which is non – toxic and thus widely used in bio – medical research. The experiments are conducted with focus on the effect of the surfactant concentration on the thinning velocity. This provides us with the ability to classify the film interfaces in fluid and rigid – like, according to the surfactant concentration. A sufficient amount of ions suppresses the electrostatic double layer repulsion between the film interfaces. In this way, we can follow the thinning of the films until the formation of the very thin Newton black films (NBFs). Classical mechanical models do not suffice to describe fluid flow in nano – confinements. The thinning behavior is analyzed with a combination of existing theoretical models and analytical and numerical methods, which incorporate interfacial processes. We obtain quantitative information on the mobility of interfacial surfactant molecules, from that we can then draw information to their distribution and design more complex TLF systems.

The stability of a nanofluidic system depends on the interfacial and bulk properties. This is studied in the second part of this work with a similar experimental setup. TLFs containing rod – like, multivalent ions are compared to systems with monovalent ions. We find an unexpected and significant difference of film stability, whereas films containing monovalent ions remained substantially longer in the metastable Common Film (CF) state compared to films containing a comparable concentration of rod – shaped ions. This is discussed with respect to the impact of rod – like ions on the condensation process of DNA. The experimental results are compared to theoretical predictions and a quantitative agreement on the systems energy gain for the change from CF to NBF can be obtained. A new attractive component of the disjoining pressure is predicted.

In the third part of the work, the behavior of nanoparticles in confinement is investigated with respect to their impact on the fluid flow velocity. We apply the above mentioned theoretical model for quantification of the flow velocity. The particles alter the flow velocity by an unexpected high amount, so that the resulting changes in the dynamic viscosity cannot be explained by a realistic change of the fluid viscosity. Only aggregation and clogging can explain the experimental results.

Finally, the location of the particles with respect to their lateral and vertical arrangement in the film is studied with advanced reflectivity and scattering methods. Neutron reflectometry studies are performed to investigate the location of nanoparticles in the TLF perpendicular to the IF. For the first time, we study TLFs using grazing incidence small angle X – ray scattering (GISAXS), which is a technique sensitive to the lateral arrangement of particles in confined volumes. This work provides preliminary data on a lateral ordering of particles in the film.

In summary, this work shows that natural nanofluidic systems can be modeled and successfully studied using free standing thin liquid films as experimental systems.

2 SCIENTIFIC BACKGROUND

2.1 Liquid / Gas Interfaces

2.1.1 Introduction

The channel walls control fluid behavior in nano – channels not only via interfacial forces, but also the character and quality (e.g. roughness) of the interfaces play a significant role. A systematic study of nanofluidic processes requires designing nano – channels with precise interfacial characteristics. Liquid and gaseous IFs are well known for purity and lack of defects, since the quality of the IF solely depends on the purity of the fluid, which is controllable. Even small amounts of impurities in the liquid adsorb to the IFs, changing their quality and physical and chemical properties. Characteristic properties of liquid IFs, like the surface tension, the surface charge density, or the mean free space of adsorbed species depend on the properties of the liquid.

2.1.2 Surface Tension

Molecules located at liquid / gas IFs face stronger attractive dispersion forces than molecules in the liquid bulk. The result is a higher energy state of interfacial molecules, which makes the location of molecules more favorable in the bulk. This explains the trend of liquids to minimize their interfacial area, which can be seen in the formation of water droplets. The surface tension σ describes the interfacial energy. Thermodynamically, σ equals the change of the Gibbs free energy G in relation to a change of the surface area A, which is needed to increase an interface by a certain area at constant absolute temperature T, pressure p and chemical potential μ [5].

$$\sigma = \left(\frac{\partial G}{\partial A} \right)_{T,p,\mu} \qquad \textit{Equation 2.1}$$

The surface tension of a liquid can be influenced by the adsorption of surface active molecules at the interface. The properties of the surfactants determine their specific effect on σ, which decreases with increasing amount of adsorbed surfactant. The measurement of surface tension of a liquid can be measured via a variety of different methods. The drop formation of liquids is used in the drop – shape analysis, where the shape of a drop at the end of a capillary is directly related to σ, and the drop – volume method, where the maximum volume of liquid, forming a free hanging drop is related to σ. The force, which counterbalances σ, is measured by the ring or Wilhelmy – plate

methods. Probes (a ring or a plate) are mounted on a balance and are brought in contact with the liquid / gas IF. The force, which is experienced by the probe relates directly to σ.

2.1.3 Adsorption to Liquid / Gas Interfaces

The adsorption describes the enrichment of surfactant at the interface in respect to the concentration of surfactant in the bulk. The adsorption process, the spontaneous change of a molecule from the bulk to the interface in terms of location and energy, is reversible and the change of an interfacial molecule to the bulk is called desorption. The surface excess Γ is defined as

$$\Gamma = \frac{N}{A} \qquad \textit{Equation 2.2}$$

where N is the number of molecules at the IF and A is the interfacial area. The driving force for adsorption or desorption processes is the thermodynamic equilibrium of the system. Changes in the bulk concentration of surfactant result in changes of the interfacial molecular concentration and vice versa. The amount of adsorbed molecules at the IFs increases with the concentration of molecules in the bulk until a maximum coverage of the IF is reached, and the surface tension reaches its lowest point. The relation between σ and Γ for a system is found in experimentally obtained adsorption isotherms where the surface tension σ is measured at constant temperature T for a systematic variation of the surfactant concentration c.

2.1.4 Adsorption Isotherms

The Gibbs adsorption equation describes thermodynamically how a change in the surface tension is related to the change in the chemical potentials of all substances. A simplification yields

$$\left(\frac{d\sigma}{dc}\right)_T = -\frac{\Gamma RT}{c} \qquad \textit{Equation 2.3}$$

which relates the change of the surface tension ($d\sigma$) to the change of surfactant concentration in the bulk (dc). The simplified Gibbs adsorption equation, with R as the gas constant, is applicable only for highly diluted bulk solutions and the formation of monolayers of molecules at the IFs (in contrast to bilayers or more complex structures).

The shape of adsorption isotherms differ with the adsorption properties of the molecules. Various empirical equations have been developed to relate the shapes of the isotherms to the surfactants.

The Langmuir – Szyskowski model [6-7]

$$\sigma - \sigma_0 = -RT \cdot \Gamma_\infty \ln\left(1 - \frac{\Gamma}{\Gamma_\infty}\right)$$

Equation 2.4

$$\frac{\Gamma}{\Gamma_\infty} = 1 + \frac{a}{c}$$

with a, the Langmuir adsorption constant, which describes the affinity of molecules to be adsorbed at the surface. σ_0 is the surface tension of the pure solvent and Γ_∞ is the maximum adsorption capacity of molecules at an IF. Via Equation 2.2 the minimum space of a molecule at maximum surface coverage can be determined. The Langmuir – Szyskowski isotherm is used to derive information on the critical micellar concentration of the respective surfactant. This is the concentration, above which the molecules self assemble in the bulk to form micelles. Thus, the study and interpretation of adsorption isotherms is essential for liquid IFs and TLF studies, because it provides a way for characterizing different surfactant systems.

2.1.5 Diffusion

For dynamic considerations of liquid – gas interfacial systems, the transport of molecules to and from the proximity of IFs by diffusion has to be taken into account. Since the time scale for adsorption (and desorption) processes is up to several orders of magnitude higher than the diffusion processes of molecules in an aqueous system, the diffusion of molecules is the limiting factor (Figure 2.1).

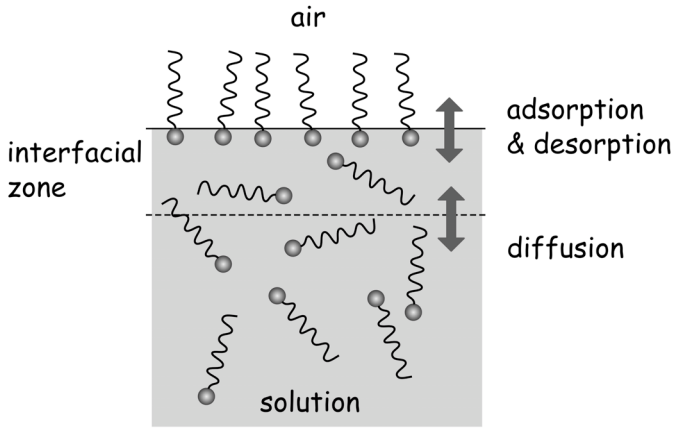

Figure 2.1 Adsorption and desorption processes close to an IF. The transport of molecules to the interface is diffusion controlled. The large differences in the time scale between adsorption and diffusion processes (up to several orders of magnitude) make diffusion the time limiting factor for the equilibrium between IF and bulk.

The kinetics of the processes like the attainment of equilibrium of an aqueous system are limited by the diffusion speed of the molecules.

The driving force of diffusion is a concentration gradient of molecules over a distance (x). Fick's first law of diffusion shows how the diffusion constant (D) relates the flow of the molecules (j) to the concentration gradient (dc/dx)

$$j = -D\frac{dc}{dx} \qquad \textit{Equation 2.5}$$

Diffusion at IFs also follows Fick's law with the difference that the surface excess Γ is considered instead of c. Thus we can use Fick's law to interpret interfacial movement of surfactants. This will be applied in results chapter 4.1.4.

2.1.6 Surface Active Agents (Surfactants)

Surfactants can be classified into different categories. Molecular surfactants are usually of amphiphilic character and consist of a hydrophilic (polar) head group and a hydrophobic (non – polar) hydrocarbon chain. The head groups are anionic, cationic or non – ionic, the hydrocarbon chains can be single or multiple. At air / water IFs, such molecules are adsorbed in a way that they expose the hydrophobic chain to the air and the hydrophilic part to the aqueous phase, the energetically most suitable constellation.

Above the critical micellar concentration (cmc) of surfactant molecules in the solvent, the molecules self – assemble in the bulk to micellar aggregates. In aqueous solvent, the hydrophobic tails point to the center of the micelle. Dependent on the character of the molecules, they form spherical or ellipsoidal micelles.

During the last decade, nanoparticles have been found to change IFs similarly [8]. Their ability of stabilizing foam and emulsion films has become a focus of research. Dependent on their wettability (contact angle between solvent and particle) they have a greater or lesser affinity to the surface. For particles, as well as for surfactant molecules the question on toxicity and bio – compatibility is crucial, especially in the application field of life – science.

The ever – increasing environmental concern about surfactants triggers an interest in natural surfactants. Sugar – based "natural" surfactants are gaining ever – growing awareness [9-10]. They are of low toxicity, biodegradable, and are widely used in protein solubilization and membrane studies [11]. The non – ionic surfactants have been proven to be rather non – sensitive to changes in temperature or pH of the solution. The non – ionic, sugar based surfactant used in the present study is n – dodecyl β – maltoside ($\beta - C_{12}G_2$) and several investigations on foam films stabilized by

$\beta - C_{12}G_2$ have been performed [12]. Quantitative values of the disjoining pressure Π [13], the thickness h [13], the gas permeability [14], the pH – dependence [15], and the contact angle θ [16] are available in literature. Moreover, temperature -, surfactant -, and electrolyte – concentration dependent equilibrium thickness and disjoining pressure measurements were reported [16].

2.1.7 Charges at Liquid / Gas Interfaces

The surface potential of liquid / gas IFs is dependent on the type and concentration of adsorbed surfactants. It has been established, that a plain air / water IF has a negative surface potential. A widely accepted explanation suggests, that in the absence of a surfactant, the charge of the air / solution interface is determined by the adsorption of OH^- ions at the interface [17]. The liquid / gas IF of water containing (indifferent) electrolytes is negatively charged. The same applies for the solutions of non – ionic surfactants. However, the adsorbed surfactant molecules reach for the same places at the IF as the OH^- ions, which effectively reduces the absolute value of the negative charge. The IF is either positively or negatively charged for cationic and anionic surfactants. This has been shown experimentally, indicating the charge reversibility of the IF when a positively charged surfactant adsorbs to the IF [18].

2.2 Interfacial Forces

2.2.1 Introduction

The downscaling of channel dimensions from micro to nanometer geometries implies that nearly all liquid molecules inside the nanochannels are affected by interaction with the channel interfaces. Thus, understanding interfacial forces, which act at nanometer distances to surfaces, is essential for all nanofluidic applications. Such forces have been investigated since the 1930s and the experimental methods capture forces in solid / liquid IFs as surface force apparatus [19] to liquid / liquid or gas / liquid IFs in emulsion or foam thin liquid films (TLFs) [20]. Experimental findings gave evidence to the existence of several forces for two interfaces at nanometer separations.

2.2.2 Repulsive Electrostatic Forces

Charged liquid / gas IFs induce a distance – dependent distribution of oppositely charged ions in the liquid phase. According to the Stern model, a number of (counter) ions adsorb at the IF and form a fixed layer, the Helmholtz layer. The diffuse

double layer represents the region near the IF where the ions are arranged as a cloud according to the model.

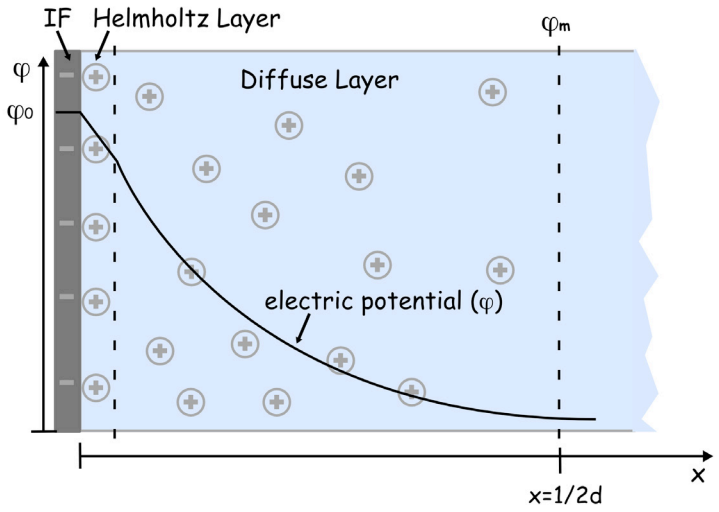

Figure 2.2 Stern model of negatively charged IF. A fixed layer of counterions (Helmholtz layer) at the IF and diffuse, cloud – like distributed ions close to the IF. The interfacial potential φ_0 decreases linearly in the Helmholtz layer and follows an exponential decay in the diffusive layer with distance x from the IF. For a symmetrical setup with two opposite IFs, the midplane potential φ_m is defined at the position x=1/2d, for the distance d of the IFs.

When two charged interfaces approach, a repulsive force between the IFs can be measured because their diffuse double layers overlap. The repulsive force acting on a unit area is defined as Π_{el}, the pressure of electrical double layer repulsion.

The quantity of Π_{el} can be derived from the Poisson – Boltzmann equation, which describes the potential $\varphi(x)$ for an electric field $E = \partial\varphi / \partial x$ at any distance x between two charged IFs and the midplane located at $x = \frac{1}{2}d$ with d, the interfacial distance (compare Figure 2.2).

$$\frac{d^2\varphi(x)}{dx^2} = -\frac{-z \cdot e \cdot \delta(x)}{\varepsilon\varepsilon_0} = -\left(\frac{z \cdot e \cdot \delta_m}{\varepsilon\varepsilon_0}\right)\exp\left(\frac{-z \cdot e \cdot \varphi(x)}{k_B T}\right) \qquad \textit{Equation 2.6}$$

where z is the valency of the ions, $\delta(x)$ is the number density ($\delta = c \cdot N_A$) of counter ions in the bulk and δ_m at the midplane, N_A is the Avogadro constant, e is the electronic charge, ε and ε_0 are the dielectric permitivities of the medium and vacuum, T is the absolute temperature and k_B is the Boltzmann constant. By solving the Poisson – Boltzmann equation at different boundary conditions, the ion concentration in the mid-

plane between two symmetrical charged surfaces can be obtained, from which the double layer repulsion Π_{el} can be determined.

Following the weak overlap approximation [20 (p.405)], Π_{el} between two planar IFs can be related to the surface potential of TLFs, the distance d of the IFs, and the density and the valency z of ions in the liquid core of the film.

$$\Pi_{el} = 64 k_B T \delta_{el} \tanh^2\left(\frac{ze\varphi_0}{4k_B T}\right) \cdot \exp(-\kappa d)$$

Equation 2.7

$$\kappa^{-1} = \sqrt{\frac{\varepsilon\varepsilon_0 k_B T}{8\pi\delta_{el} e^2 z^2}}$$

where δ_{el} is the number density of ions in the film forming solution and φ_0 the double layer potential at the interfacial interaction plane. The position of the interaction plane in TLFs is very important for the precise definition of the electrostatic disjoining pressure. We assume that the plane is positioned in the region occupied by the head groups of the surfactant molecules, therefore φ_0 is the electrostatic double layer potential at the surfactant head group layer in the film. The characteristic Debye length κ^{-1} describes the thickness of the diffuse layer, thus the interaction distance of the charged IFs [4]. The length decreases with increasing counter ion concentration, i.e. with increase in electrolyte concentration. The typical diffuse double layer thickness for room temperature ranges from 1 - 100 nm, depending on the electrolyte type and concentration. Equation 2.7 is valid for univalent electrolytes, large separation and small surface potentials. For multivalent asymmetrical electrolytes no simplifications can be made for the calculations of Π_{el} (see chapter 4.2.3, p.54).

Multivalent ions are different from monovalent ions by the fact that more than one charge is located at the same position. The Bjerrum length λ_B (Equation 2.8) describes the distance where the electrostatic interaction energy is equal to k_BT.

$$\lambda_B = \frac{e^2}{4\pi\varepsilon\varepsilon_0 k_B T}$$

Equation 2.8

where *e* is the elementary charge, ε is the relative dielectric constant of the medium and ε_0 is the vacuum permittivity. For water at room temperature, we obtain λ_B = 0.7 nm.

2.2.3 Van der Waals Dispersion Forces

Dispersion, or van der Waals (vdW) Forces describe the noncovalent attractive or repulsive forces acting between all atoms and molecules in a system. Also in thin liquid films of thickness smaller than 100 nm, interfacial dispersion forces are active between the film surfaces. The forces originate from the interaction between existing or induced dipoles among the neutral or charged molecules [4].

The vdW forces between macroscopic objects can be described on the basis of two different models. The microscopic approach [21] is based on the pairwise additivity of individual dispersion forces among molecules and reveals shortcomings at very small distances (between atoms when their wave functions overlap), or at large distances > 100 nm (when electromagnetic retardation must be considered). In contrast to the microscopic approach, the macroscopic theory combines the interactions between single atoms or molecules to a force between continuous media. All molecules in the system experience the same field which originates from all involved single atoms and molecules. This theory considers two dielectric half – spaces and uses Maxwell's equations to calculate the fields [22]. For the interaction between two plane parallel (semiinfinite) plates (or phases) of distance h separated by a medium, the simplified macroscopic approach [4]

$$\Pi_{vdW} = -\frac{A_H}{6\pi h^3} \qquad \textit{Equation 2.9}$$

describes the van der Waals dispersion force on a unit area with the van der Waals component of the disjoining pressure Π_{vdW} and the material specific Hamaker constant A_H.

The dispersion forces between two equally condensed phases in vacuum or in air is attractive, thus Π_{vdW} is noted by definition with a negative sign (compare Equation 2.9). The interactions between two film interfaces are a sum of all pair interactions between the single molecules at the interfaces and can be theoretically calculated. A TLF can be described according to the macroscopic approach as a symmetrical air / water / air system, with the liquid filling the gap between two air phases. A_H for such a system has been determined to be ca. 10^{-20}J, whereas the influence of the film stabilizing adsorbed surfactant layer at the gas / liquid IFs on the value of A_H plays a smaller role [4].

2.2.4 DLVO Theory

The Derjaguin, Landau [23] and Verwey, Overbeek [24] (DLVO) theory, was originally developed to describe the colloidal stability determined by a balance between electrostatic repulsion of diffuse layers of ions and the molecular interaction between two separated phases of distance h (van der Waals attraction). It was also successfully applied to describe the interaction forces between interfaces of thin liquid films [20]. The interaction forces per unit area of the film are termed disjoining pressure (Π).

For symmetrical TLFs, the vdW force Π_{vdW} acts attractively, against the disjoining work of the electrostatic repulsion Π_{el}. The film IFs are in equilibrium distance when external and internal forces are equal: $P_{ext} = \Pi_{vdW} + \Pi_{el}$, where $P_{ext} = P_c$, the capillary pressure (chapter 2.3.2) in the case of TLFs. The resulting force on the TLF (per unit area) is defined as the disjoining pressure $\Pi(h) = P_c = -\Pi_{vdW} + \Pi_{el}$ [4, 20]. The disjoining pressure isotherm (Figure 2.3) shows schematically the shape of $\Pi(h)$ for a symmetrical TLF system.

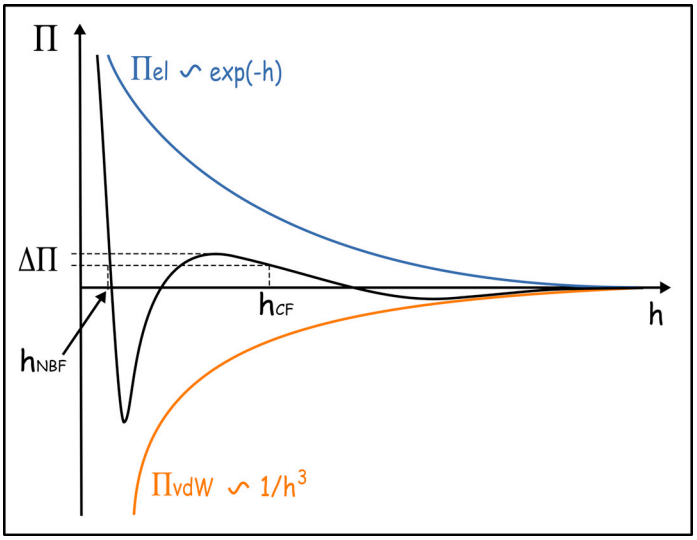

Figure 2.3 Disjoining Pressure Isotherm: The disjoining pressure Π versus the distance of the film interfaces h; Π_{el} in blue describes the electrostatic repulsion and Π_{vdW} in orange describes the van der Waals attraction force. The distance h_{CF} is a metastable state, a pressure in the size of $\Delta\Pi$ is necessary to reach the thinnest possible equilibrium state h_{NBF} .

At an interfacial distance h (film thickness) larger than ~ 100 nm, the influence of Π is not significant. The TLFs, which are considered in this work as nanofluidic systems are with thicknesses from 5 to 100 nm in the influential range of the interfacial

forces. In this thickness range, Π shows characteristic features which explain experimentally observed states. At the film thickness h_{CF} the Common Film (CF) is formed. The barrier of size $\Delta\Pi$ hinders the CF to transition to the smaller thickness h_{NBF} of a Newton black film (NBF) [25 (p.168 f.)] or ruptures. CF and NBF are the two states with an energy minimum. The height of the separating energy barrier can be influenced by the concentration of electrolyte in solution or by applying an external pressure.

The DLVO theory is sensitive to the charge density at interfaces, to the concentration of ions at IFs, but not to the specific interactions and ion properties like the shape of the ion. The DLVO theory describes forces which act on average in a direction perpendicular to the IFs, but does not cover forces, which act in the plane of the IFs or local structural changes at the IFs, like surfactant density fluctuations.

The extended DLVO theory also takes into account various additional forces contributing to the disjoining pressure. Steric repulsion forces, hydrophobic attractive forces, or hydration forces have been introduced to explain the stability of colloidal systems or the thinning behavior of thin liquid films [4].

2.3 Thin Liquid Films

TLFs have proven to be suitable experimental tools because of their simple geometry, reproducible preparation, and well defined interfaces [4]. The practical interest in these films stems from the fact that several of their properties are determined by the same forces, which also govern the stability of colloidal dispersion systems like foams, emulsions and sols. The fundamental interfacial and bulk properties of TLFs have already become subject of research since the middle of last century. The studies aimed on properties of fluid interfaces and the role of the surface interaction forces. Properties of foam films like the equilibrium film thickness h allow the calculation of the interaction forces between the film surfaces. The contact angle between film and meniscus gives insight into the interaction free energy per unit of film area [25-26]. Gas permeability measurements yield information on the density of the surfactant layers stabilizing the foam film and thus on long term foam stability [26]. The main part of these studies has been summarized in books and reviews [20, 25, 27-32]. These studies complement investigations of liquid confined between solids performed with the colloidal probe Atomic Force Microscope, and the modern surface force apparatus [4, 33-35].

2.3.1 Structure

Foam films are free standing TLFs which separate the bubbles in foams. They are composed of a thin layer of liquid with adjacent liquid / gas interfaces. In nanofluidic terms, the IFs would resemble the channel walls which confine the liquid bulk. The schematic cross – section of a foam film is visualized in Figure 2.4 with respect to its molecular setup (a) and relevant forces (b).

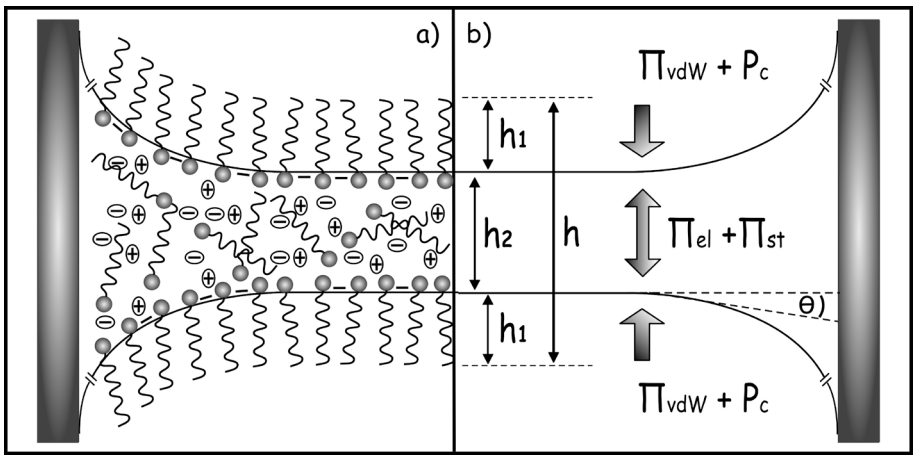

Figure 2.4 Cross section of a free standing liquid film prepared in the glass capillary cell according to Scheludko – Exerowa [25] (a) Surfactant molecules adsorbed at the film interfaces, electrolyte and free surfactant molecules in the core and meniscus of the film. (b) Indication of the thickness of the film h. The arrows show the forces acting in and on the film. Attractive van der Waals forces (Π_{vdW}) and capillary pressure (P_c) counteract repulsive electrostatic (Π_{el}) and steric forces (Π_{st}). θ is the contact angle between film and meniscus.

At the film IFs, the characteristic negative charges and adsorbed surfactant molecules are indicated. The aqueous core (bulk) contains surfactants and ions in the same amount as the film forming solution. The flat, central area of the TLF is much smaller than the curved meniscus region, which connects the film and the capillary wall. Realistic numbers are ~ 50 - 70 µm for the film radius and ~ 4 mm for the capillary radius.

2.3.2 Capillary Pressure

The IF of the meniscus region in Figure 2.4 shows a characteristic curvature towards the capillary walls (enlargement in Figure 2.5). The curved IFs induce a pressure difference between air and liquid, where the pressure inside the liquid is larger than outside. The resulting capillary pressure P_c, dependent on the capillary radius R_c

and the surface tension of the liquid σ for completely wetted capillary walls is described by the Laplace equation

$$P_c = \frac{2\sigma}{R_c} \qquad \textit{Equation 2.10}$$

which gives the value of the capillary pressure which is the primary external driving force for the first phase of liquid outflow from TLFs. The equation is valid only for completely wetted capillary walls when the radius of the film is much smaller than the radius of the capillary ($R_f << R_c$).

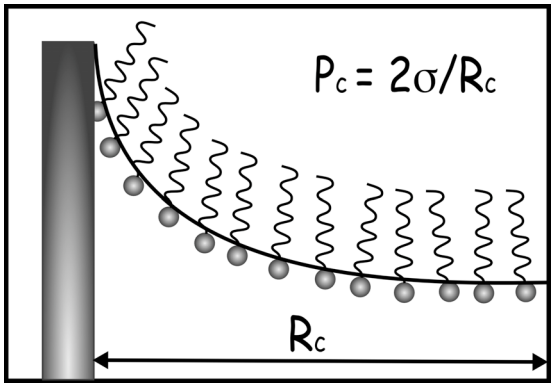

Figure 2.5 Characteristic curvature of film IF in meniscus region towards the capillary wall

2.3.3 Film Thickness

The thickness of a TLF can be described by the three layer model with respect to the film structure [36]. As illustrated in Figure 2.4 (b), the two surfactant monolayers with thickness h_1 and the aqueous core of thickness h_2 add up to the film thickness h:

$$h = h_2 + 2h_1 \qquad \textit{Equation 2.11}$$

Common Films consist of an aqueous bulk phase with monolayers of surfactant molecules at the IFs and the thickness is in the range of 10 - 100 nm. The thinnest CFs appear black, similar to NBFs, and therefore the term common black film (CBF) is often found in literature. NBFs possess the smallest possible thickness, in the range of about 4 - 10 nm, depending on the type of surfactant molecules. These films are practically bilayers of surfactant molecules with almost no free water. They are stabilized due to the balance between steric repulsions in the film, caused by a direct contact between the hydrophilic heads, or respectively, the hydration shells of the surfactant molecules, and the van der Waals attraction [25, 27].

2.3.4 Film Stability and Rupture Mechanisms

Under stable TLFs, we understand films, which are stable in the limits of the experiments. Strictly, all foam films are non – equilibrium meta – stable structures, which will eventually break, reaching a more stable (lower energy) state after a certain time. Different rupture mechanisms of foam films have been suggested and various theories established for the description of film stability. All explanations include local thickness variations of the film IFs (Figure 2.6). The amplitude of the deformations is Δh, the wavelength of the surface fluctuation is λ.

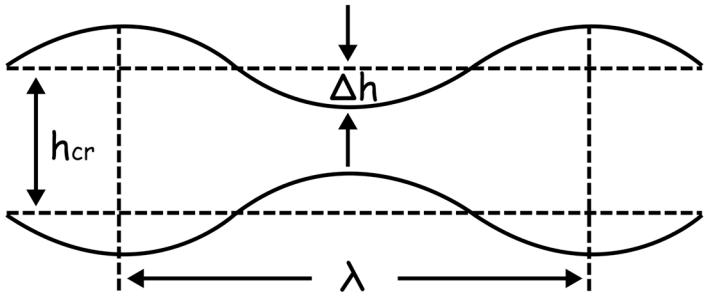

Figure 2.6 Model of critical film thickness h_{cr}. The film interfaces show local deformations of the amplitude Δh in distance of λ. The rupture occurs at the moment when Δh grows up to the order of the ciritcal film thickness h_{cr}.

The accepted rupture mechanism for foam films assumes the existence of surface corrugations with stable, growing surface fluctuation waves of various wavelengths. If surface wave amplitudes Δh at both interfaces grow symmetrically, the growth of Δh is related to an increase of local attractive disjoining pressure $\Pi_{vdW} = -A_H / 6\pi(h + \Delta h)^3$ due to the decrease of the local film thickness. The TLF loses its stability at the moment when the film thickness approaches h_{cr}. At this point, the film either ruptures or a step – like local thinning occurs. The mechanism of rupture by local thinning is applicable to films of a certain thickness, which are considered as liquid structures. The thinner spherical regions appear black when observed optically, and thus this process is called black spot formation. This mechanism cannot be applied to ultrathin NBFs of a fixed bilayer structure of surfactant molecules with bound hydration water. Such thin films cannot thin locally but can rupture by direct nucleation of holes or mediated nucleation of holes through vacancy aggregation according to Refs [37-38]. The role of the interfacial visco – elasticity for stability was also investigated and found that a high viscosity and elasticity dampen surface fluctuations and always increase the

foam film stability. The viscosity of the film forming solution determines the stability of thinning films whereas surface elasticity is decisive for the strength of the surface fluctuations of CFs. The discussion on film stability influenced by surface visco – elasticity is reviewed in Ref [31]. It has been found that the rupture of unstable films and the formation of black spots occur at the same critical thickness h_{cr} [25]. Thus, the theory of rupture is not only applicable to film rupture, but also to the formation of stable NBFs, and is therefore a significant theory for film stability.

A first approximation of the amplitude of thermal surface corrugations at room temperature for a solution of σ = 50mN/m gives the equipartion law

$$|\Delta h| \approx \sqrt{\frac{k_B T}{\sigma}} \approx 0.3nm\,. \qquad \textit{Equation 2.12}$$

Assuming the absence of the electrostatic repulsive force due to high electrolyte concentration, the disjoining pressure is defined as $\Pi = -\Pi_{vdW}$. Under these conditions, h_{cr} can be derived to follow

$$h_{cr} = \left(\frac{A_H}{8\pi^3\sigma}\lambda^2\right)^{1/4} \qquad \textit{Equation 2.13}$$

where A_H is the Hamaker constant, λ stands for the surface wave length, and σ is the surface tension of the solution from which the film is formed [20, 25 (p.116)].

Local thickness fluctuations have been attributed to thermal surface corrugations since the 1960s [39]. This concept has been object of discussion and another explanation has emerged in the context of explaining thickness artifacts at the film / meniscus border namely marginal regeneration. Local surface tension fluctuations are held responsible for the thickness differences [40]. Earlier explanations for rupture took the spontaneous formation of thinner areas in the film into consideration, i.e.: hole – nucleation [41-42] . The mechanism of rupture by local thinning is applicable to films of a certain thickness, which are considered as liquid structures. In this work we will not discuss origins of surface fluctuations but rather their effects on the stability of TLFs.

2.4 Fluid Dynamics

The interfacial forces act over the whole geometry range of our model nanofluidic channel diameters (5 – 100 nm). This explains that there is practically no fluid in the channels which is not in the sphere of influence of the surface forces. For the theoretical description of liquid flow through nano – channels, this implies that the behav-

ior of liquid in nm distance to the IF cannot be described according to classical macroscopic laws, as it is usually sufficient for macro- or microfluidic calculations. Special theories and models need to be derived to incorporate interfacial processes.

Fluids are categorized in gases and liquids, dependent on the intermolecular distance, and thus, their compressibility. Qualitatively, gases and liquids show similar flow behaviors at the same conditions (pressure, temperature), but due to their unequal physical and chemical properties (density, compressibility, viscosity), there are substantial quantitative differences. The assumptions for the description of ideal fluids are no friction between fluid molecules, no influence by the surfaces (e.g. by surface tension) on the fluid, no influence of gravity (only valid for ultra small liquid volumes), and a uniform pressure distribution. This yields to a constant viscosity of ideal, Newtonian fluids.

The dynamics of fluid flow on the macroscopic scale is successfully described by the Navier – Stokes equations for classical continuum hydrodynamics. The lubrication approximation by Stefan [43] and Reynolds [44]

$$V_{Re} = \frac{2}{3} h^3 \frac{P}{\eta R_f^2} \qquad \textit{Equation 2.14}$$

with the outflow velocity V_{Re} and the dynamic viscosity of the liquid η, is a special case of the Navier – Stokes equations to describe the outflow of a fluid from in between two rigid disks of distance h and radius R for h << R.

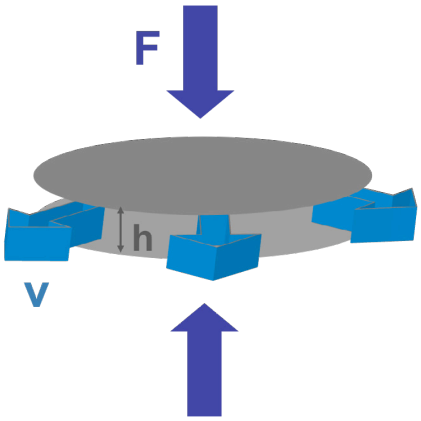

Figure 2.7 Liquid outflow from rigid, plane parallel discs, with radius R and distance h. The liquid has the velocity V_{Re} according to the lubrication approximation.

The theory is valid (amongst other criteria [31]) for a Newtonian liquid and limited to zero flow velocity at the interfaces and to a constant force applied on the disks. When the Reynolds theory of liquid outflow from solid plates was applied to foam films,

it was found that they drain faster than predicted by the theory. This phenomenon could be explained with additional forces, expressed in the disjoining pressure Π(h), acting on the film interfaces due to their sub – micrometer separation. This is formulated in the modified Stefan – Reynolds equation for film thinning [20]

$$V_{Re} = \frac{2}{3} h^3 \frac{P_c - \Pi(h)}{\eta R_f^2} \qquad \textit{Equation 2.15}$$

where V_{Re} is the thinning velocity, h is the average film thickness, η is the dynamic viscosity of the film forming solution (assumed to be equal to η *of water*), and R_f is the film radius. Numerous studies of Π(h) and its impact on film thinning for various surfactant TLF systems have been conducted, because knowledge on the drainage of foam films is essential for accurate predictions of the stability and lifetime of a film [25, 31, 45-50]. Despite the existence of a large body of information on the drainage of thin films, significant uncertainties remain in the ability to predict thinning velocities using basic physicochemical properties [51].

2.5 Nanoparticles Confined in Thin Liquid Films

In medical research there is an increased interest in introducing nanoparticles and nanocapsules within human bodies for example as contrast media in magnetic resonance imaging and as targets for the observation of intracellular processes, or as drug delivery containers for medicine [52]. In order to study the flow of these particles through nano – sized cell wall channels or the finest blood capillaries, models for nanofluidic channels, as in our case TLFs, have to be designed. We expect molecules in the size range of the channels like large ions, biomolecules or nanoparticles, to show effects on the thin liquid film system due to repulsive forces or conformation changes.

In the past, studies of micelles in TLFs have been reported [53-54] as well as macromolecules confined in TLFs were studied [30, 55-57]. Nanoparticles have become recently famous as efficient stabilizers of foam films [58] and emulsion films [30] without additional surfactant. A comparison between common surfactants and solid particles as stabilizing agents has been summarized in literature [8].

In contrast to their ability of stabilizing TLFs, hydrophobically modified particles can be found in most antifoaming formulations, dispersed in (PDMS) oil. Despite systematic studies [59-60] the actual mechanisms how the particle – oil mixtures destroy foams, have remained unclear.

Studies on the dynamics of particles in TLFs showed, that above a certain concentration of nanoparticles in the film forming solution, the particles show a tendency to form a layered structure and produce stepwise film thinning (stratification) [61]. Layer by layer of particles leave the film. Scientists claim that with such a controlled stratification process well ordered particle arrays can be produced [62].

The theoretical understanding of the behavior of particles in TLFs is not satisfying, and it has even been suggested that in these systems, the sizes and strengths of the forces between the nanoparticles make the system fall into a regime where equilibrium thermodynamics may no longer apply at the time scales of the measurements. It was found that parts of the systems appear to be in (local) equilibrium, while others, such as jammed regions, are not [63].

3 METHODS AND MATERIAL CHARACTERIZATION

3.1 Experimental Methods

3.1.1 Microinterferometric Thin Liquid Film Analysis

Numerous fundamental studies of thin films have been conducted with different measurement setups. One often used experimental system to study thin liquid films is the specially designed capillary glass cell, referred to as Scheludko – Exerowa glass ring cell [25]. The reservoir of the glass ring cell (Figure 3.1 [64] (d)) is filled from top with the film forming solution. In this way, also the connected glass capillary ring (e and t_1) fills up. With a piston (f), the reservoir can be closed at the top. The cell (a) is placed in a closed vessel (b), which is connected to a thermostat and kept at constant temperature in the device support (c).

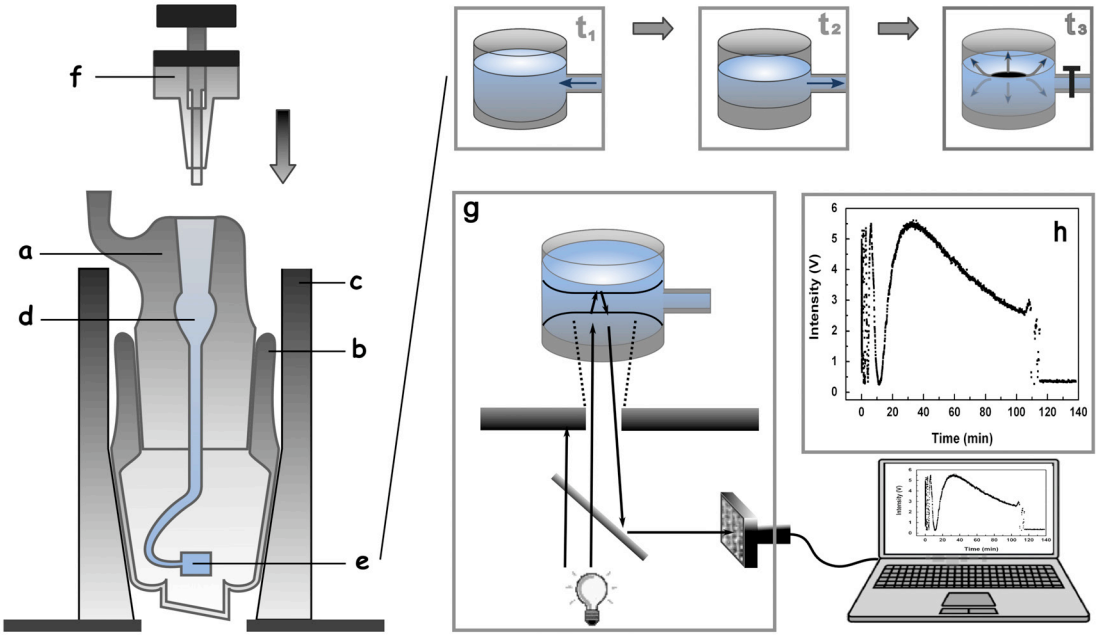

Figure 3.1 Measurement setup for thin film studies with the Scheludko – Exerowa measurement cell setup (a-f), the schematic transformation of the drop into a flat ultra thin film (t_1-t_3), the interferometric measurement of the light intensity and thus the film thickness (g, h)

By turning the rotary knob of the piston, the liquid can be sucked from the capillary and the drop turns into a horizontal, biconcave, very thick film (t_2). It starts thinning spontaneously, driven by the capillary pressure. When the film thickness de-

creases to a certain value, additional interfacial forces between the two surfaces of the film come into play as described in chapters 2.2 and 2.3. These forces expel the liquid from the film until equilibrium is reached (t_3).The film thinning is obtained in situ with a micro – interferometer measurement setup. A small area of the film is illuminated and the light reflects back from both film interfaces (g). The reflected light intensity I(t) with thickness dependent interference patterns is detected and recorded digitally over time (h).

The interference of the reflected light is in direct relation to the distance between the film interfaces, i.e. to the film thickness. The recorded, back reflected light intensity can be translated into the thickness of the film

$$h_w = \frac{\lambda}{2\pi n}\left(k\pi \pm \arcsin \sqrt{\frac{I(t)/I_{\max}}{1+\left[\left(n^2-1\right)/2n\right]^2\left(1-I(t)/I_{\max}\right)}}\right) \qquad \textit{Equation 3.1}$$

$$h_w = h_2 + 2h_1\frac{n_1^2-1}{n_2^2-1} \qquad \textit{Equation 3.2}$$

with h_w, the so called equivalent thickness of the film as a function of I(t), the light intensity at time t. The last maximum (at k=0 in Equation 3.1) of light intensity of the periodically repeating positive and negative interference of reflected light is the maximum light intensity I_{max}. The experimentally obtained film thickness h_w differs from the before defined film thickness h by the contribution of the optical properties of interfacial layer (h_1, n_1) and bulk layer (h_2, n_2) of the film. The film thickness h is smaller than the experimentally obtained equivalent film thickness of a homogeneous film due to higher refractive index of the hydrophobic tails in contrast to air. The difference of h_w to the absolute thickness $h = h_2 + 2h_1$ is in the case of films thicker than 30 nm below the statistical error of the measurement method. The accuracy of thickness measurements is ± 0.2 nm [65]. The wavelength of the light was filtered at 545.6 nm. Only films with plane parallel surfaces are suitable to be used for observation of the thinning behavior based on the interference of reflected light. It was shown [57], that foam films with a radius below 100 μm fulfill this criterion. We choose the radii of the films in the range of 70 μm ± 3.5.

The introduction of one common origin of time for all data sets is necessary to be able to compare the kinetics of film thinning. The occurrence of I_{max} is defined as the reference point of time where t=0 is set. In this way, a distribution of measured data points is obtained as shown exemplarily for one of the concentrations of surfactant in *Figure 3.2*.

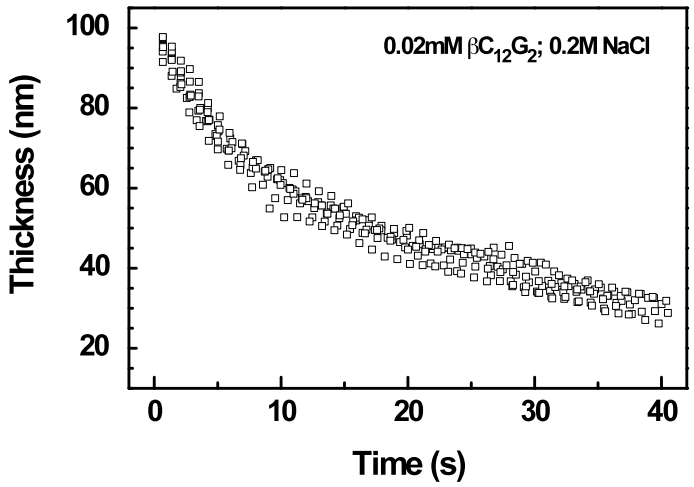

Figure 3.2 Dynamics of thinning of foam films from aqueous solution containing 0.02 mM β-$C_{12}G_2$ and 0.2 M NaCl. The experimentally obtained data from eight measurements are shown as squares [64].

The deviation between individual h(t) curves can be attributed to the fact that the setup does not allow to determine the radius of the film more precisely than ± 7 μm, which leads to small changes in the thinning velocity V_{Re} (Equation 2.14, p.18). Local surface corrugations in small areas of the film can alter the thinning behavior in a way that the h(t) curves are wavy. The last point of the curves is the critical point of rupture, where the film either ruptures or spontaneously transforms into a NBF.

3.1.2 Neutron Reflectometry

Neutron reflectometry (NR) is a technique, which allows gaining material information perpendicular to the surface of planar structures like thin films of a variety of solid and liquid materials. When neutrons impinge on a surface, the interaction of the neutrons and the atomic nuclei can be related to specific material properties. The scattering length density (SLD) is defined as $N_b = n \cdot b$, with b, the average coherent scattering length of n atoms. Similar to visible light and X – rays, neutrons follow the general laws of reflection at interfaces. The reflection of an incident neutron beam from an ideally flat interface is shown schematically in Figure 3.3.

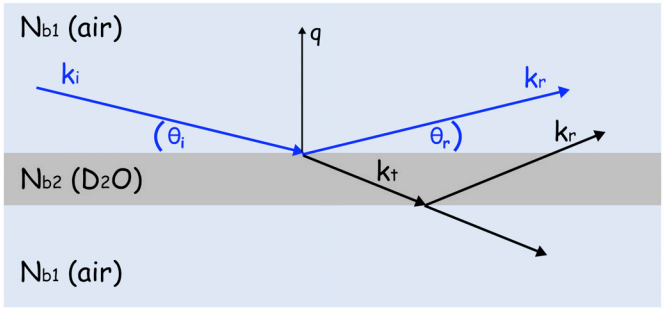

Figure 3.3 Reflection of an incident beam from an ideally flat surface (blue arrows) with θ_i the incident angle and θ_r the angle of beam reflection; k_i and k_r are the wave vectors of incoming and reflected beam; q is the wave vector transfer. N_{b1} and N_{b2} stand for the SLD value of air and D_2O, respectively. The transmission and reflection at the second IF (black arrows) alter the values of k_r and q and thus the intensity of the reflected beam.

The reflection of a neutron is usually described as a function of the momentum transfer q_z of the incident and the scattered wave vectors k_i and k_r along the surface normal z.

$$q_z = \frac{4\pi}{\lambda} \sin\theta_i \qquad \textit{Equation 3.3}$$

with λ as neutron wavelength and θ_i as incident angle.

The ratio of the intensity of the incident beam (I_0) and the intensity of the reflected beam (I) is defined as reflectivity Z.

$$\frac{I}{I_0} = Z \approx \frac{16\pi^2}{q_z^4} N^2 \qquad \textit{Equation 3.4}$$

The reflectivity for the case of total reflection is Z = 1. It decreases for an ideal air / D_2O interface, as illustrated in Figure 3.4 ((a), black line).

The incident beam is reflected and refracted at each interface, leading to a superposition of individual reflectivities. Characteristic fringes show up due to interference of the reflections along q_z. The distance Δq_z between adjacent minima in the reflectivity curve gives the individual layer thickness *d* in the system according to

$$d = \frac{2\pi}{\Delta q_z} \qquad \textit{Equation 3.5}$$

The theoretical reflectivity curve for a neutron beam reflected at the IFs of a 30 nm thin layer of D_2O, surrounded by air is shown in Figure 3.4 ((a), red line). The respective scattering length density profiles are presented in Figure 3.4 ((b), (c)).

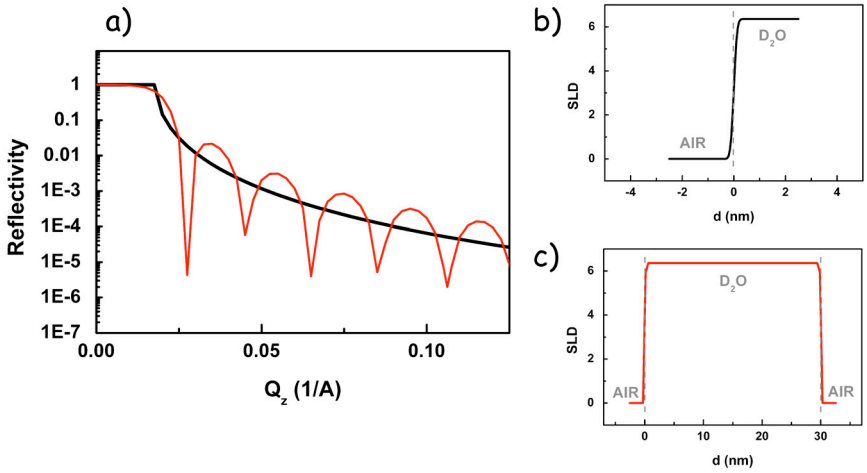

Figure 3.4 (a) Theoretical reflectivity curves of bulk D_2O (black) and a liquid film of D_2O of 30 nm thickness (red) surrounded by air; (b) Scattering length density profile for the air / D_2O IF; (c) Scattering length density profile for the air / D_2O / air thin film system.

Neutron reflectivity experiments can be realized in the monochromatic mode, where the reflectivity is measured as a function of the reflected beam angle $\theta_i = \theta$ and in the time of flight (TOF) mode, where sample and detector are at fixed θ - 2θ positions (Figure 3.5) and the neutron wavelength λ is varied.

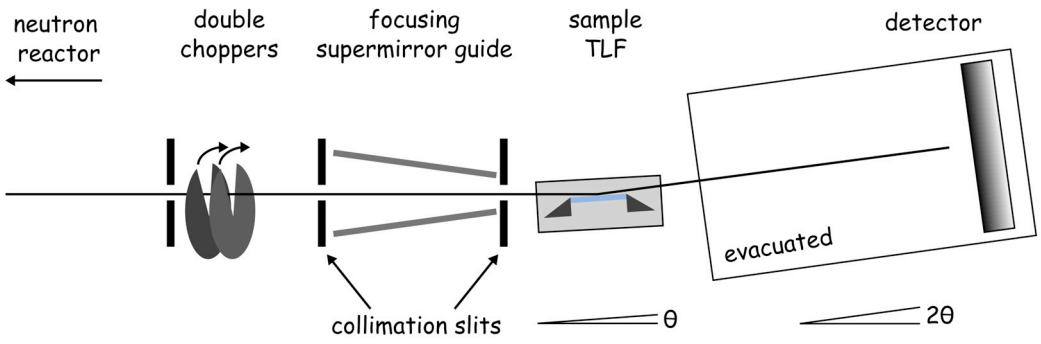

Figure 3.5 A top view of the instrument D17 at the ILL in time of flight (TOF) mode.

The distance between detector and sample can be several meters and the longer this distance, the higher the resolution but the lower is the q_z range. In TOF mode, an entire order of magnitude in q_z can be measured simultaneously in less than a minute, thus kinetic studies are possible.

For data analysis, TOF results in the form of reflection intensities $I(\lambda)$ are transferred to $R(q_z)$. In that way, the usage of standard fitting software is possible, which convert scattering length density profiles into model reflectivity curves and recursively compare those to the experimental data until the best agreement is obtained.

For the experiments, a specially designed experimental cell (Figure 3.6) was used, which can also meet the requirement of horizontal alignment of the sample.

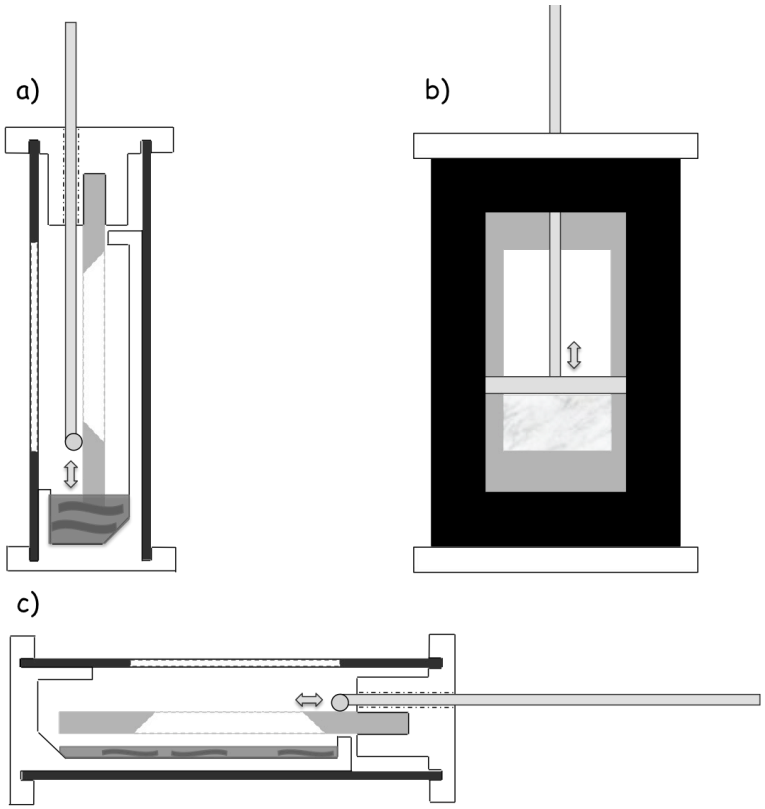

Figure 3.6 Measurement cell for NR (and for GISAXS) experiments. (a) intercept of the measurement cell in side view; a small basin on the bottom contains the film forming solution; (b) film preparation using a glass skewer; (c) cell can be tilted horizontally, the residual film forming solution flows in back part of the same basin.

3.1.3 Grazing Incidence Small – Angle X – Ray Scattering

Grazing incidence small – angle X – ray scattering (GISAXS) emerged to a versatile analysis technique for nanometer thin films with respect to internal film structure and morphology. By selecting an incidence angle on the sample surface close to and even below the critical angle of total external reflection of X – rays, the wavefield penetration depth is decreased down to a few nanometers. This enhances the sensitivity to a thin (surface) layer. Any discontinuity in the local electronic density, induced e.g.

by roughness or particles, scatters either the transmitted or the reflected beam. For valuable measurements, a synchrotron source with its inherent properties of high flux, collimation and multi – wavelength availability, combined with 2D detectors are necessary to have reasonable counting time.

The geometrical setup for a GISAXS experiment is shown in Figure 3.7. The sample is positioned in the x – y plane, and the X – ray beam impinges on the sample surface under a fixed angle of incidence α_i with the wave vector k_i and the wave number $k_0 = 2\pi / \lambda$. The beam is scattered under the exit angle α_{sc} in the scattering plane (x – z plane), and an out – of – plane angle ψ (horizontal scattering angle).

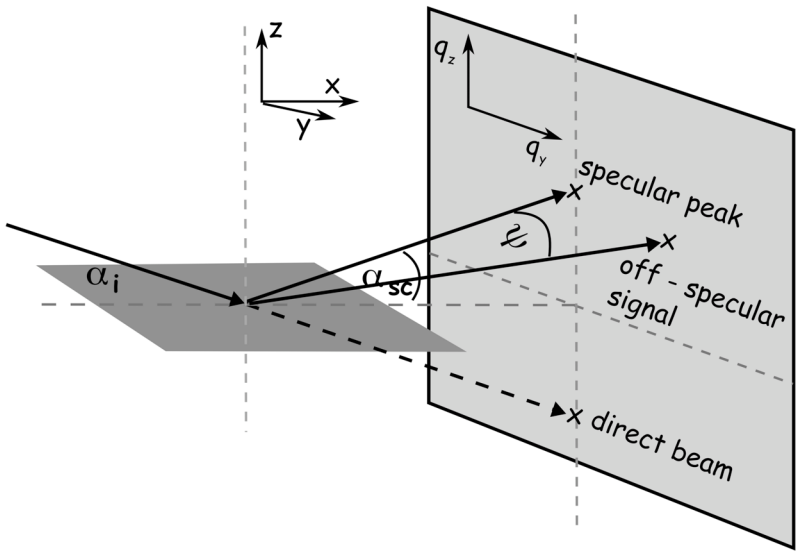

Figure 3.7 Scheme of the basic experimental setup of a GISAXS experiment. The sample is positioned in the x – y plane and the X – ray beam impinges on the sample surface under a fixed angle of incidence α_i. The scattered beam is described by the exit angle α_{sc} in the scattering plane (x – z plane), and the out – of – plane angle ψ (horizontal scattering angle).

In order to block the direct beam, a diode beam stop is used in front of the detector. Furthermore, to avoid saturation of the detector by the scattering signal, a point-like moveable specular beam stop was employed to block the specularly reflected beam on the detector.

As each different sample morphology leads to different GISAXS patterns, appropriate analysis methodologies and models have to be developed for analyzing data. A way of simplifying the data analysis of the 2D intensity image is the effective surface approximation (ESA), where data only have to be analyzed as a function of q_y for cuts

at constant q_z. Using ESA, the out – of – plane scattering can be approximated to depend on the form factor of individual objects and on the structure factor [66-67].

3.1.4 Tensiometry

The interface of solutions or dispersions containing surfactants can be characterized and compared via the value of the experimentally obtained surface tension. The measurement of surface tension with the Wilhelmy plate method is based on the contact of a platinum plate balance with a liquid surface (Figure 3.8).

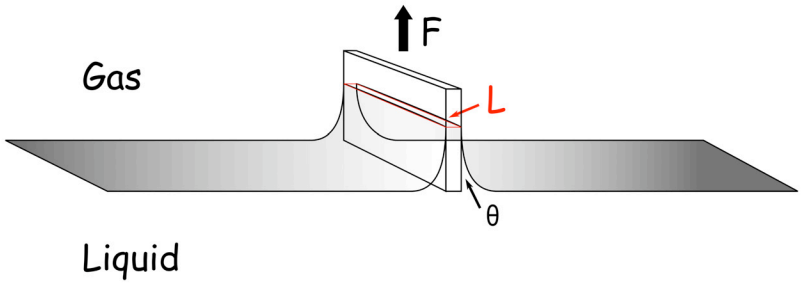

Figure 3.8: Measurement principle of the surface tension with the Wilhelmy plate method. The plate is brought in contact with the liquid interface, and the force (F) experienced by the balance as the probe interacts with the surface of the liquid are related to the perimeter (L) of the plate and the wetting angle (θ) between liquid and plate.

The forces experienced by the balance as the probe interacts with the surface of the liquid are related to the perimeter of the plate and the wetting angle between liquid and plate. The surface tension (σ) is calculated according to

$$\sigma = \frac{F}{L\cos\theta - \rho g V_d} \qquad \textit{Equation 3.6}$$

where F is the force acting on the plate orthogonal to the IF, L stands for the perimeter of the plate, ρ is the fluid density, g the gravitation constant, and V_d the immersed volume of the plate. The contact angle θ of the water or the surfactant solution on a platinum plate is very small and can be regarded as zero.

3.1.5 Transmission Electron Microscopy

The transmission electron microscope (TEM) operates on the same basic principles as a light microscope with electrons instead of photons. The main applications of TEM is imaging of organic or inorganic structures with lateral dimensions be-

low the resolution of light microscopes. In a TEM, electrons travel through vacuum to the sample which is mounted on a special grid. Electromagnetic lenses focus the electrons into a very thin beam. The electron beam travels through the specimen, where some of the electrons are scattered or absorbed by the material. The residual transmitting electrons hit a sensor e.g. a CCD camera at the bottom of the microscope, and create a "shadow image" of the specimen with its different parts displayed in varied darkness according to their density. The sample is moved under the electron beam, so that areas of up to several μm^2 can be scanned, dependent on the enlargement. The recorded image scan can be analyzed with respect to characteristics of interest. The resolution of a light microscope is limited by the wavelength of light; theoretically the smallest observable structure size would be 200 nm. The particle – wave character of electrons makes their wavelengths dependent on the accelerating voltage. For acceleration voltage values around 100 kV the wavelength of electrons are in the range of picometers. Theoretically, resolutions of sub – atomic 1/10 Á could be achieved, but due to the inefficiency of the electromagnetic lenses which focus the beam, resolutions of around 0.2 nm are the maximum reached.

3.1.6 Dynamic Light Scattering

Dynamic Light Scattering (DLS) is one of the most popular methods used to determine the size of colloidal particles or aggregates in suspension. It is based on the fact that colloidal particles in solution undergo Brownian motion which can be detected via intensity fluctuation of backscattered light. The correlation of these intensity fluctuations can be translated into the size of the particles.

During measurements, a monochromatic (laser) light beam is focused onto a colloidal dispersion. Each single particle or aggregate functions as scattering center for the incoming light whilst it undergoes random thermal (Brownian) motion. The fact that the particles move according to their size – the smaller ones faster, the larger ones slower– causes an interference pattern of the backscattered light, which changes in time. Thus, the backscattered light arriving at the detector under a certain angle shows time resolved intensity fluctuations which can be analyzed with respect to the mean relaxation time of these intensity fluctuations using an intensity autocorrelation function.

For a monodisperse sample with polydispersity index (PDI) of one, the time dependent relaxation of a system would follow a single exponential decay and the steepness of the decay would be related to the diffusion coefficient (D) of the particles in medium.

A polydisperse sample, would give rise to a series of exponential decay functions with unlike steep decays. Via the Stokes – Einstein equation

$$R_h = \frac{k_B T}{6\pi\eta D} \qquad \textit{Equation 3.7}$$

D is connected to the hydrodynamic radius (R_h or z_{ave}) of a equivalent sphere in medium of known viscosity (η). Dynamic light scattering can be used for the analysis of samples containing small nanoparticles of around 2 - 5 nm in diameter, as well as for polydisperse samples which contain micrometer – sized aggregates. The method analyses liquid samples non - invasively, thus, it is often used as a complementary technique to TEM, where the samples have to be dried before analysis.

3.2 Stability Study of Particle Dispersions

3.2.1 Motivation

When studying TLFs with NR or GISAXS, the films have to fulfill certain experimental requirements. The surface area of the film has to be substantially larger than the illuminated area (footprint), so that a measurement without border effects can be guaranteed. For the neutron beam with a footprint of about 1 – 2 cm length and 1 cm width, a frame for the film of 2.5 x 3.9 cm is used. The X – ray beam has a comparable smaller footprint of about 3 – 4 mm length and 40 µm width, so the film area is smaller with 1.175 x 2.5 cm. In contrast to the TLFs in the glass ring cells with a diameter no larger than 140 µm, the larger films show substantial differences in terms of mechanical stability, plane parallelism and evaporation of the film due to the larger surface area. The stability of the films is not only challenged by the increased surface area of the films, but also by extreme duration of single measurements of up to 8 h. Evaporation is another factor, which is increasingly dominant in experiments with large TLFs. Low humidity and unstable temperature conditions in the beamline halls, plus occasionally emerging technically induced vibrations motivate the usage of an advanced experimental cell setup. We used the cell presented in Figure 3.6 for the best possible evaporation protection. The realization of the large and stable films was attempted by increasing the viscosity of the film forming solution, thus we decided to add 25 vol. % glycerol to the film forming solutions. In order to see the impact of the glycerol on the system, short and long term stability studies were performed. The main techniques used were DLS and TEM.

3.2.2 Stability (Short Term)

As reference, the Fe_3O_4 particles stabilized by oleic acid (OA) in aqueous solution, were characterized. The focus was put on their average diameter and aggregation. DLS and TEM (Figure 3.9) studies agreed, that the diameter is in average 9 ± 2 nm, but varying in the range from 5 - 16 nm.

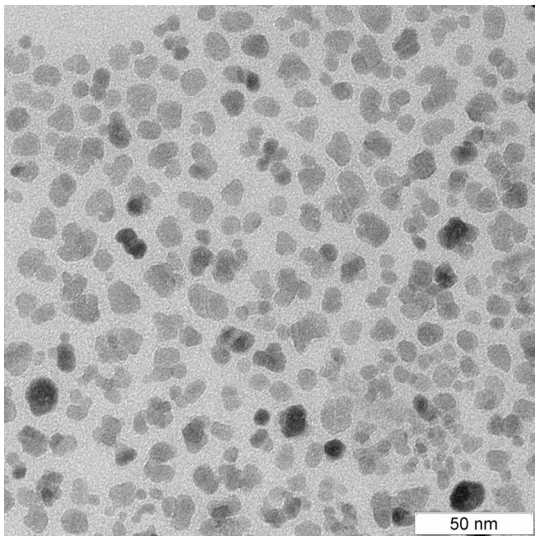

Figure 3.9 TEM image of Fe_3O_4 particles. The average diameter of the particles is 9 nm ± 2, whereas the smallest are 5 nm and the largest up to 16 nm in diameter.

For preparation of the film forming solutions, a specified amount of Fe_3O_4 particles were diluted in water and mixed with the surfactant $\beta - C_{12}G_2$, the electrolyte NaCl, and glycerol. A series of TEM and DLS measurements for all possible combinations of H_2O, 25 vol % glycerol, 0.6 mg/ml Fe_3O_4, 0.4 mM $\beta - C_{12}G_2$ and 0.2 M NaCl always in the presence of Fe_3O_4 was performed. In that way, we can understand the impact of each single ingredient. For the NR and GISAXS measurements all of the above components are part of the film forming solution. The results of the measurement series can be summarized as the following:

- In all samples, separated particles of diameter 5 - 15 nm were found. The sample which is used for NR and GISAXS measurements is shown in Figure 3.10.
- In absence of surfactant (0 mM $\beta - C_{12}G_2$) and presence of electrolyte (0.2 M NaCl) and glycerol (25 vol%), the samples turn cloudy and aggregate.
- In all of the samples containing electrolyte (0.2 M NaCl) aggregation was detected besides the sample containing additional surfactant $\beta - C_{12}G_2$.

- The addition of glycerol destabilizes the samples, and a tendency for increased aggregation can be observed in all of the samples.
- The dispersion used in GISAXS and NR experiments (Figure 3.10) contains, next to single scattered nanoparticles, aggregates in the diameter range of 20 – 83 nm (∅ = 43 ± 18 nm).

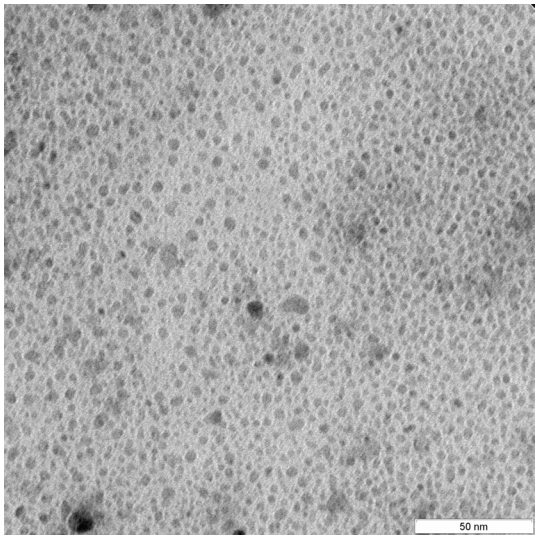

Figure 3.10 TEM image dispersion containing 0.4 mM $\beta C_{12}G_2$, 0.2 M NaCl, 25 % glycerol, and 0.6 mg/ml Fe_3O_4. Next to the single scattered particles, also aggregates can be observed.

The results indicate that $\beta - C_{12}G_2$ is necessary to stabilize the samples, without it large aggregates and instable samples are observed. We attribute the effect to screening of the particle's surface charges and additional detachment of oleic acid from particles. It seems that the surfactant attaches to the particles to "protect" them from aggregation. The addition of glycerol supports aggregation, thus in the sample for NR and GISAXS aggregates with mean diameter of 43 nm were found. This result needs to be kept in mind for interpretation of the thinning behavior of small TLFs containing particles in comparison to results from NR and GISAXS experiments.

3.2.3 Stability (Long Term)

After understanding that glycerol supports aggregation in the film forming solutions, studies on the long term stability of the particulate dispersions were performed. The intention of the study was to find out the maximum time in which the dispersions could be prepared before the NR and GISAXS experiments.

First, the long term stability of the Fe_3O_4 particle sample in the original concentration was studied. It was found that the sample remained stable for more than one

year in the bottle from the company (2007, ∅ = 9.1 ± 2.6 nm, 4.3 ≤ ∅ ≤ 17.4 nm; 2009, ∅ = 9.0 ± 2.5 nm, 5.1 ≤ ∅ ≤ 15.9 nm). After dilution of the Fe_3O_4 sample with H_2O, severe aggregation was observed, depending on the dilution factor.

When we studied the samples for NR and GISAXS experiments, we found that the dispersions were at least 49 days stable (Table 3.1). The predominant species remained the separated scattered particles (99.1 %) and a small percentage (0.9 %) were aggregates in the size of ∅ = 47 – 51 nm, comparable to the sample which was measured one day after preparation and gave ∅ = 43 nm. After 14 days and after 49 days no significant indication for destabilization could be observed.

Table 3.1 DLS study on the long term stability of the dispersion containing 0.6 mg/ml Fe_3O_4 particles, 0.4 mM $\beta C_{12}G_2$ surfactant; 25 % glycerol; 0.2 M NaCl. The period between sample preparation and measurement is given, The mean diameter based on the intensity of scattered ligh z_{ave} ,the polydispersity index (PDI), as well as the particle diameters by number and respective fractions.

			Number	
Time	Z_{ave} *in nm*	*PDI*	*Ø in nm*	*%*
8 days	10.7	0.4	8.1	99.1
			47.5	0.9
14 days	9.6	0.4	10.1	99.4
			51.4	0.6
49 days	9.1	0.3	5.8	99.9
			46.6	0.1

Following from the above results, all samples for NR and GISAXS experiments were prepared not more than eight days before they were used.

4 RESULTS AND DISCUSSION

4.1 Thin Liquid Films in Nanofluidics – Dynamics of Thinning of Films from the Non – Ionic Surfactant $\beta - C_{12}G_2$

4.1.1 Introduction

When using a thin, free standing liquid film as nanofluidic channel, the characterization of the bulk and the interfaces of the film is a basic requirement. The properties of foam films from the non – ionic surfactant n – dodecyl – β – maltoside ($\beta - C_{12}G_2$) in the non – equilibrium state, during the process of film formation (thinning) is presented in the following chapter and can be found in literature [64]. The experiments will be conducted with focus on the effect of the surfactant concentration on the thinning velocity. A sufficient amount of ions, here sodium chloride (NaCl), suppresses the electrostatic double layer repulsion between the film interfaces, so that we can follow the thinning of the films until the formation of the very thin NBF. The thinning behavior will be analyzed with a combination of existing theoretical models and analytical and numerical methods. We aim at quantitative information on the mobility of the surfactant molecules in the air / liquid interfaces, and on their concentration distribution.

4.1.2 Characterization of the Film Forming Solution

The surface tension of the film forming solution, which is specific for each surfactant gives insight into the purity of the system and characteristic numbers, like the critical micellar concentration (cmc). The surface tension measurements of aqueous solutions containing 0.2 M of NaCl and concentrations of $\beta - C_{12}G_2$ surfactant of 0 - $4 \cdot 10^{-2}$ mM are shown in Figure 4.1 and complement already published data from Ref [16].

The experimentally obtained isotherm was fitted with the software IsoFit [68] using the Langmuir – Szyskowski model according to Equation 2.4 (p.6). Considering the length of the hydrophobic chains of the surfactant molecule, the Frumkin adsorption model, which takes into account in – plane attraction or repulsion, was also applied but the resulting fit showed no substantial difference in the fitting parameters, so that we decided for the Langmuir – Szyskowski Model. The surface tension of the surfactant free solvent containing 0.2 M NaCl was determined to be σ_0 = 72.2 mN/m.

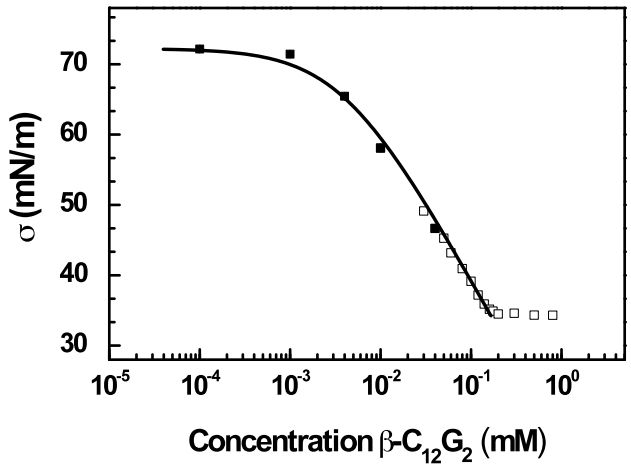

Figure 4.1 Surface tension of aqueous solution containing 0.2 M NaCl and $\beta - C_{12}G_2$: solid symbols, data measured in the present work; open symbols, data from Ref [16]. The solid line indicates the best fit to the data using the Langmuir – Szyskowski isotherm.

We obtain the following values for the fitting parameters: Γ_∞ = 4.09·10^{-6} mol/m^2 and *a* = 3.97·10^{-3} mM. Γ_∞ corresponds to a molecular area of 0.41 nm^2 which is about twice the cross section of an aliphatic chain. Hence, these chains are disordered and the density is determined by the sugar moiety or the surfactant (The structure of the molecule is shown in Figure 6.1, p.87). The critical micelle concentration (cmc) of the surfactant was determined from the kink point of the curve to be 0.16 mM. The values for a, Γ_∞ and the cmc are similar to those found in the literature [49, 69-70].

4.1.3 Dynamics of Thinning

We recorded the dynamics of thinning of foam films stabilized by different amounts of the non – ionic surfactant $\beta - C_{12}G_2$ in the presence of 0.2 M NaCl. In Figure 4.2 we show experimental data sets of the change of the film thickness over the time during the film formation process. Each dataset is an average of eight measurements. The error bars indicate the standard deviation of the average. The theoretical fits are shown as solid lines, the procedure to obtain the fits is explained in the following chapter. The thinning curves are each presented as different graphs for reasons of clarity. We can see that the start of the thinning is the point of I_{max} (t=0), which correlates to the maximum thickness h_{max} of ~ 100 nm. The thinning was followed until the films spontaneously became NBFs at the critical rupture thickness h_{cr}. A trend from lower to higher h_{cr} with increasing surfactant concentration can be observed.

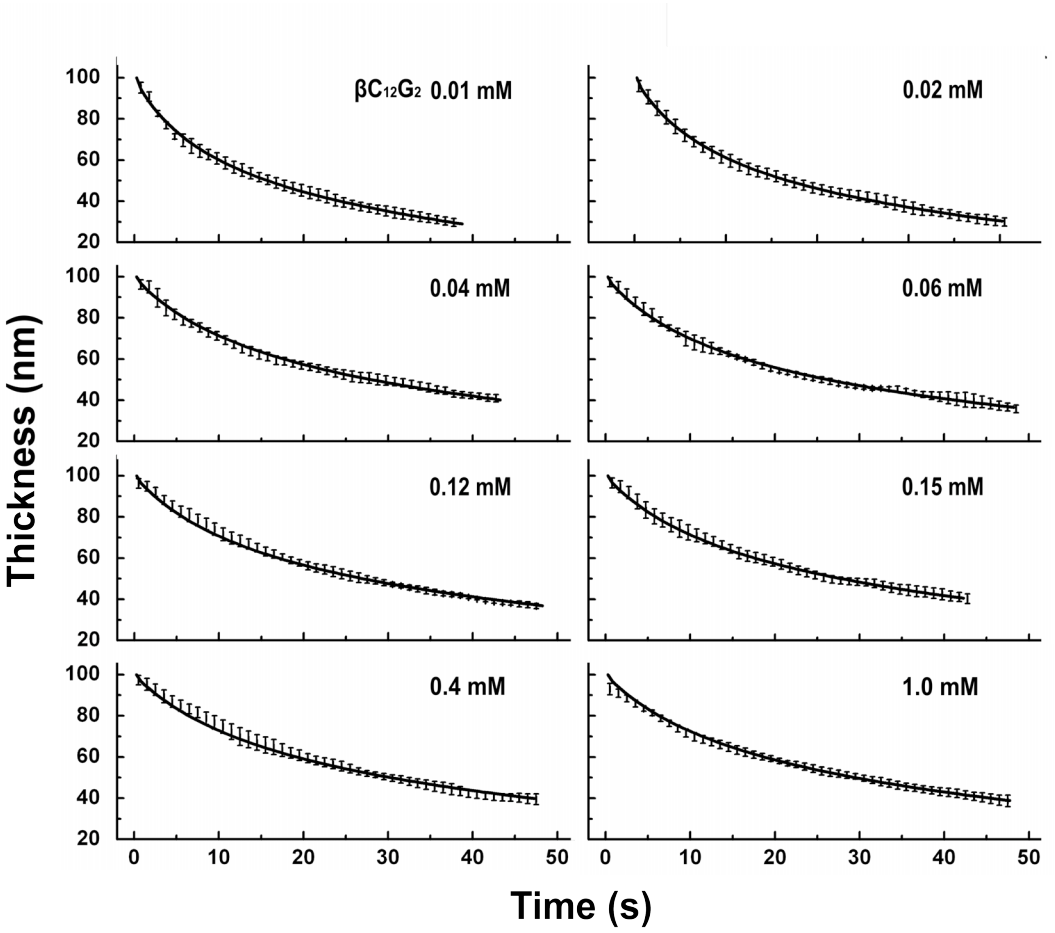

Figure 4.2 Experimentally recorded dynamics of thinning for foam films from solution with 0.2 M NaCl and $\beta - C_{12}G_2$ from 0.01 mM to 1 mM. Each of the curves is an average result of eight measurements. The error bars indicate the standard deviation from the mean. The theoretical fits are shown as solid lines.

We did not perform an in – depth analysis of h_{cr}, which would be necessary to discuss the dependence of h_{cr} from the surfactant concentration. We focused here on the in – depth analysis of the process of film thinning.

4.1.4 Theoretical Approach to Analyze the Thinning of TLFs

A combination of previously developed theoretical approaches for the quantitative analysis of the dynamics of film thinning will be introduced in the following. The aim is a physical fitting function, which can be used to analyze the data in respect of interfacial characteristics. Refs [27, 71-72], as well as references therein, give a more detailed derivation of the theory. Here, a qualitative understanding of the main assumptions and necessary steps are presented in order to be able to obtain a physical fitting function.

We have seen before, that when the Reynolds theory of liquid outflow from solid plates was applied to foam films, the drainage was faster than predicted by the theory (compare chapter 2.4, p.17), and a modified Stefan – Reynolds equation for film thinning was formulated (Equation 2.15, p.19) [20].

It was further found that the conditions under which Equation 2.15 was obtained are not met due to the fluidity of the film interfaces [71]. The interfaces, a fluid mosaic of adsorbed surfactant molecules, are neither necessarily non – deformable nor are the surfactant molecules at the interfaces immobile. At this point, we neglect interfacial deformability according to Ref [72] and explain briefly how the fluidity of the interfaces and resulting fluxes influence the thinning velocity of foam films.

The first assumption is that the amount of surfactant at the surface remains constant during the thinning process [72]. This dynamic equilibrium between surfactant adsorption to and desorption from the film interfaces is assumed to be diffusion controlled according to the bulk diffusion flux j_b with $j_b = -D_b \nabla c$ and D_b the diffusion constant of molecules in the bulk (Figure 4.3 (a)).

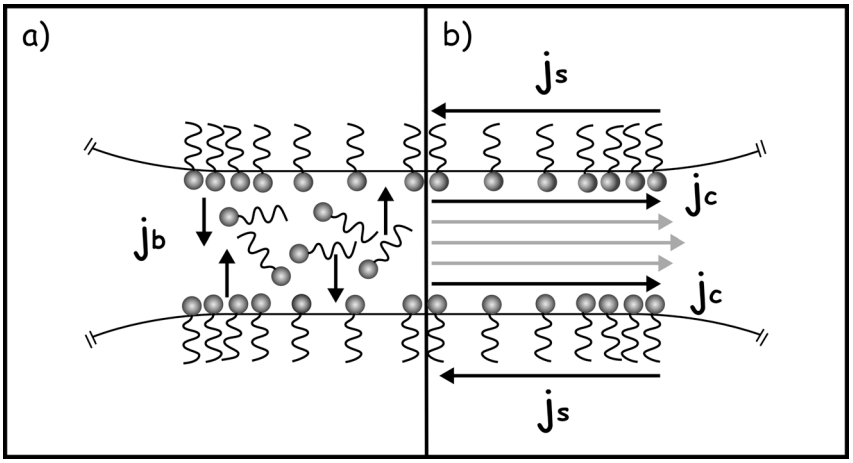

Figure 4.3 Fluxes, which determine the effective velocity of thinning of a thin liquid film. a) Diffusion – controlled adsorption process: the bulk diffusion flux j_b determines the surfactant mass balance between bulk and film surface. b) The convective flux j_c, is a result of the hydrodynamic thinning of the film. It drags surfactant molecules at the interfaces towards the periphery of the film. The gradient in the surface tension is reduced by surface diffusion processes j_s and adsorption processes a).

As shown in *Figure 4.3 (b),* it is further assumed that there are opposing interfacial fluxes: the convective flux j_c and the surface flux j_s. The convective flux j_c is a result of the pressure driven hydrodynamic outflow of liquid from the film. At the inter-

faces, $j_c = v_s\Gamma$ drags surfactant molecules with the velocity v_s towards the periphery of the film if the adsorption density Γ of molecules is low enough and the spacing in between the molecules is high enough. This situation of a non – zero velocity at the interfaces accelerates the thinning process of the film (similar to slip of liquid at solid interfaces).

The random diffusion of molecules at the film interfaces, here surface diffusion flux $j_s = -D_s\nabla\Gamma$ with D_s the diffusion constant of molecules in the surface, compensates the interfacial outflow of molecules together with the adsorption and desorption processes of surfactant molecules between bulk and interfaces.

If there were no interfacial or bulk diffusion ($j_s = j_b = 0$), a surface tension gradient between the film center and periphery would be created and this would be compensated by a (Marangoni) back – flow. Dependent on the gradient, this could reduce the interfacial velocity to zero and the thinning process should follow the Reynolds model for solid interfaces. Instead, due to adsorption/ desorption and diffusion processes, the concentration of surfactant at the interface during the thinning process is assumed to be constant.

An increase in the effective thinning velocity of a foam film is linked to the interfacial mobility of surfactant molecules and can be directly related to the surface and bulk diffusion coefficients. Hence, the thinning of thin parallel axi – symmetric films with fluid interfaces is noted according to Ref [71] as the ratio of the experimentally obtained thinning velocity V and the theoretical thinning velocity V_{Re} for the system with rigid interfaces. In the case that $V > V_{\mathrm{Re}}$ ($V/V_{\mathrm{Re}} > 1$), the contributions from bulk diffusion and surface diffusion are expressed by the parameters b and h_s according to Equation 4.1.

$$\frac{V}{V_{\mathrm{Re}}} = 1 + b + \frac{h_s}{h} \qquad \textit{Equation 4.1}$$

These parameters are directly connected to the diffusion coefficients of the molecules in the bulk D_b and at the film interfaces D_s,

$$b = \frac{3\eta D_b (a + c\ )^2}{\Gamma_\infty^2 k_B T c}$$

$$h_s = \frac{6\eta D_s a}{\Gamma_\infty k_B T c} \qquad \textit{Equation 4.2}$$

with known values for the dynamic viscosity of water η, the temperature T, the Boltzmann's constant k_B, and the concentration of surfactant under equilibrium conditions *c.* The Langmuir adsorption coefficient a and the maximum adsorption density Γ_∞ can be deduced from the Langmuir adsorption isotherm. That makes b and h_s useful fitting parameters for the analysis of experimental thinning data with Equation 4.1 as a fitting function.

In order to obtain a suitable fitting function, we followed Ref [72] and Equation 4.1 was rewritten with the required input and fitting parameters and with numerical and analytical software tools. Then this expression was analytically solved for t resulting in an analytical formula of the symbolic form $t = T(h, A_H, P_c, R_f, b, h_s)$ [64]

$$
\begin{aligned}
T(h,a_H,P_c,R_f,b,h_s) = -\frac{3}{2}\mu R_f^2(-2\sqrt{3}(a_H^{2/3}(1+b)^2 - P_c^{2/3}h_s^2)\arctan[\frac{1-2P_c^{1/3}h/a_H^{1/3}}{\sqrt{3}}] \\
+ 2(a_H^{2/3}((1+b)^2 - P_c^{2/3}h_s^2)\ln[a_H^{1/3} + P_c^{1/3}h] \\
- 6a_H^{1/3}P_c^{1/3}h_s\ln[h_s + h + bh] - 6a_H^{1/3}P_c^{1/3}h_s b\ln[h_s + h + bh] \\
- a_H^{2/3}\ln[a_H^{2/3} - a_H^{1/3}P_c^{1/3}h + P_c^{2/3}h^2] - 2a_H^{2/3}b\ln[a_H^{2/3} - a_H^{1/3}P_c^{1/3}h + P_c^{2/3}h^2] \\
- a_H^{2/3}b^2\ln[a_H^{2/3} - a_H^{1/3}P_c^{1/3}h + P_c^{2/3}h^2] - P_c^{2/3}h_s^2\ln[a_H^{2/3} - a_H^{1/3}P_c^{1/3}h + P_c^{2/3}h^2] \\
+ 2a_H^{1/3}P_c^{1/3}h_s\ln[a + P_c h^3] + 2a_H^{1/3}P_c^{1/3}h_s b\ln[a + P_c h^3]) \\
/(6a_H^{1/3}P_c^{1/3}(a_H(1+b)^3 - P_c h_s^3))
\end{aligned}
\qquad \textit{Equation 4.3}
$$

with h, A_H, P_c, and R_f as input parameters and b and h_s as fitting parameters.

For the statistical differentiation of our fitted results we applied the reduced χ^2 method. Equation 4.1 was solved numerically for h and we obtain the function $h = T^{-1}(t_0, A_H, P_c, R_f, b, h_s)$. This function can then numerically be fitted to our data for discrete time intervals t_0 (here every 0.5 seconds), whilst minimizing the reduced χ^2 function, according to Equation 4.3. The scattering of the thickness values was implemented into the fit as the weight $1/\sigma_i$.

4.1.5 Fitting Results

According to the above – described method, we fitted the experimental data of foam films stabilized by $\beta - C_{12}G_2$ in the presence of 0.2 M NaCl with respect to the parameter for surface diffusion h_s. An average value of R_f was given as input parame-

ter because of minor deviations between the single experiments. A first estimate for *b* and h_s/h in Equation 4.1 shows, that b is expected to be by a factor of *b* smaller than the value of h_s/h over the complete range of surfactant concentration. Hence, we neglect the contribution of b, and we do not expect reliable information on the bulk diffusion coefficient for our system from this method.

The resulting values for the fitted parameters and its corresponding χ^2 – values, can be seen in Table 4.1.

Table 4.1 Quantitative values for fitting parameter h_s and surface diffusion coefficients D_s obtained via the thinning dynamics of foam films from solutions of different concentrations of $\beta - C_{12}G_2$ in the presence of 0.2 M NaCl. The value of surface coverage for each concentration is provided. The error criteria χ_v^2 for the fits, in the case of mobile interfaces $b \neq h_s \neq 0$, and for comparison, assuming immobile interfaces with $b = h_s = 0$ are listed.

β - $C_{12}G_2$ conc. (mM)	Γ (10^{-6}mol/m^2)	h_s (nm)	D_s (10^{-8} m^2/s)	χ_v^2 $h_2 \neq b \neq 0$	χ_v^2 $h_s = b = 0$
0.01	2.92	20.7	8.62	0.207	7.165
0.02	3.41	9.2	7.66	0.057	1.62
0.04	3.72	2.2	3.67	0.219	0.391
0.06	3.83	1.3	3.25	0.391	0.543
0.12	3.94	0	0	---	0.533
0.15	3.98	0	0	---	0.216
0.4	4.09	0	0	---	0.403
1.0	4.09	0	0	---	0.351

The resulting ratio of the experimentally obtained thinning velocity *V* and the theoretical thinning velocity V_{Re} for the system with rigid interfaces V/V_{Re} (Equation 4.1, p.38) indicates, as shown in *Figure 4.4* , an up to 75% increase of the thinning velocity for foam films from solutions with a surfactant concentration of 0.06 mM or lower due to mobile interfaces. For higher concentrations of surfactant, we can fit the data with

values for h_s of 10^{-4} nm but we reach the resolution of the method at $h_s \approx 5 \cdot 10^{-1}$ nm and therefore we are not able to make quantitative predictions for very low surface diffusion coefficients. However, we were able to fit the data of 0.12 – 1 mM with a fitting parameter $h_s = D_s = 0$, which means that the model assuming rigid interfaces (Equation 2.15) suffices to describe the data.

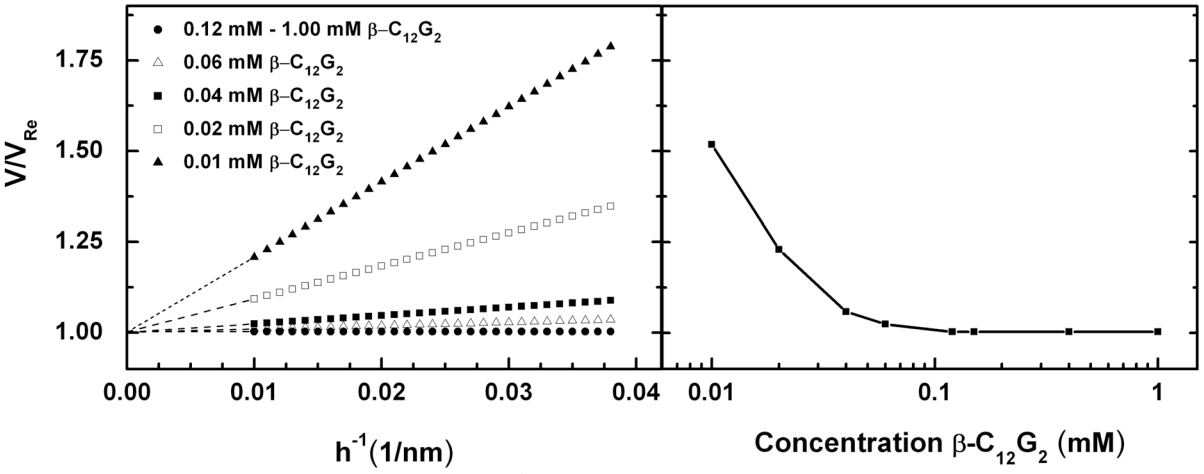

Figure 4.4 Experimentally obtained velocity of thinning (V) compared to Reynolds' / Scheludko's thinning velocity (V_{Re}). (left) plotted versus h^{-1} The slope represents the fitting parameter h_s; the intercepts of the lines with the ordinate are the fitting parameter (1+b). (right) Ratio of V/V_{Re} for films from different concentrations of surfactant, at constant thickness of h = 40 nm.

When applying the modified Stefan Reynolds' model for film thinning (Equation 2.15 p.19) to fit the data sets for 0.01 mM – 0.06 mM $\beta - C_{12}G_2$ ($h_s = D_s = 0$) the fits assuming rigid interfaces deviate substantially from the measured data points, whereas the fits which account for interfacial diffusion processes, pass accurately through the average data points as in Figure 4.5 for 0.02 mM of $\beta - C_{12}G_2$.

The statistical difference between the curves using an error analysis based on the reduced χ^2 criteria is apparent. We obtain for the assumption of mobile surfaces and molecular movement in the bulk ($h_s \neq 0$) the value for χ^2 of 0.057 and for the fit assuming immobile surfaces ($h_s = 0$) the value for χ^2 of 1.62. The value of $\chi^2 = 0.057$ appears too good (overfitting) which we attribute to the rather high standard deviation of the average data points.

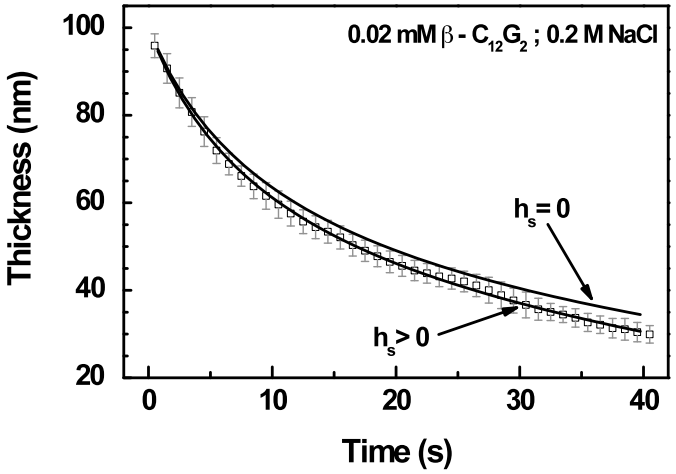

Figure 4.5 Experimental thinning data of a foam film from solution containing 0.02 mM of $\beta - C_{12}G_2$ and 0.2M NaCl (grey squares) fitted with ($h_s > 0$) and without ($h_s = 0$) contribution of the surface diffusion parameter h_s (black lines).

Nevertheless, a fit which gives a χ^2 value of 1.62 can be accepted as statistically different to the experimental data. Using the probability distribution we found that the fit which accounts for immobile surfaces represents the data points with a probability better than 5 %. Hence, we can assume that the interfaces of the films are mobile ($h_s > 0$) below a surfactant concentration of 0.12 mM, which leads to a faster drainage of the film. For a concentration of $\beta - C_{12}G_2$ larger than 0.12 mM the interfaces seem "blocked". Nevertheless, the interfacial mobility at 0.12 mM and 0.15 mM, both below the cmc, could be either below the resolution of the method or those films have blocked interfaces and no accelerated outflow.

The surface diffusion coefficients calculated according to Equation 4.2 from the fitting parameter h_s show a dependence on the concentration of $\beta - C_{12}G_2$ in the film forming solution as presented in *Figure 4.6 top*. There are two major regimes of D_s. For high concentrations of surfactant (≥ 0.12 mM) we can predict that D_s is close to zero. We assume, for that regime, that the film surfaces are rigid – like with tightly packed surfactant molecules. With decreasing concentration of surfactant in the bulk and therefore decreasing amount of surfactant at the interface, D_s increases systematically and we obtain the highest value for D_s of $8.6 \cdot 10^{-8}\,m^2/s$ at our lowest concentration of surfactant, 0.01 mM $\beta - C_{12}G_2$.

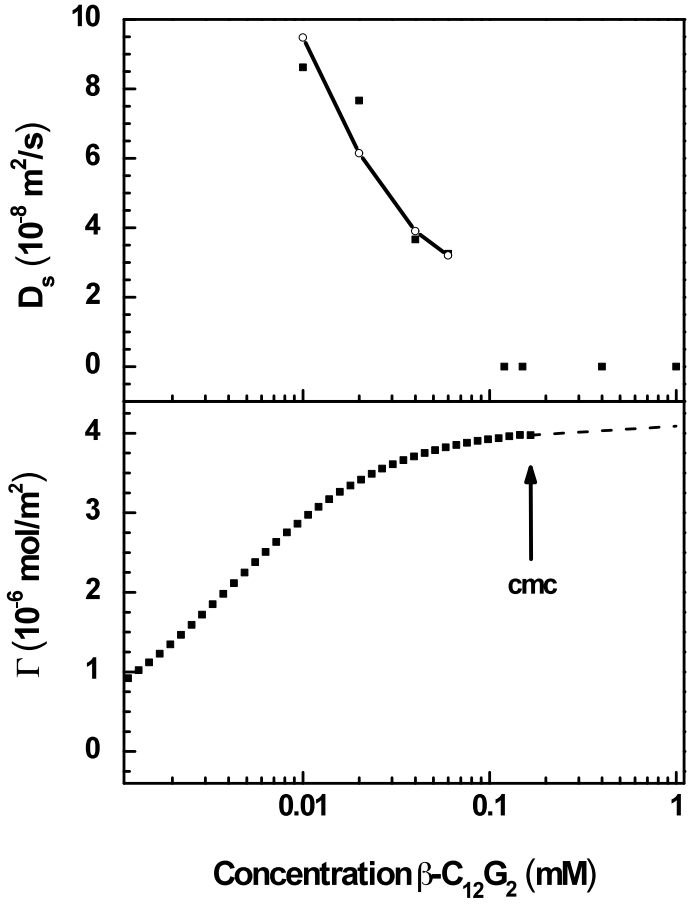

Figure 4.6 Top: Concentration dependent coefficient of surface diffusion D_s of foam films during the thinning process calculated from fitting parameters h_s as black squares, the line indicates the decrease of D_s following the free volume model [73]; Bottom: Surface coverage Γ calculated from surface tension of the bulk solution. Theoretical Γ_∞ indicated as dashed line.

The value for D_s in the range of 10^{-8} m^2/s is analogous to that presented in the literature [72, 74-75]. Even though, it seems rather high, since the self diffusion of water molecules in the bulk is $2.3 \cdot 10^{-9}$ m^2/s [5] . Generally, the diffusion coefficients at the surfaces are a factor of 10 lower. Therefore, we accept this value as an apparent surface diffusion coefficient, which might include effects of drag or convection forces, which accelerate the thinning process and reflect the measured value of the surface diffusion coefficient.

4.1.6 Interpretation of the Diffusion Coefficient according to the Free Volume Model

Studies on phospholipid monolayers spread at interfaces show that the surface diffusion coefficient of a monolayer of amphiphilic molecules depends on the free area per molecule $a_f = \bar{a} - a_0$ with $\bar{a}$ the average molecular area for certain surfactant concentration and a_0 the minimum required area per surfactant molecule. The surface coverage, as shown in Figure 4.6 bottom, is an indication for the mean free area a molecule has at the interfaces for a certain surfactant concentration. We obtained a molecular area at saturation of 0.41 nm^2 which is reasonable as one expects this value to be above a_0. Reported literature values range between 0.30 nm^2 and 0.50 nm^2 but seem higher than the maximum space a $\beta - C_{12}G_2$ molecule would need with a single hydrocarbon chain (~ 0.20 nm^2) and two sugar rings (maximum length of 0.12 nm). Experiments with deposition of $\beta - C_{12}G_2$ on solid substrates [76] showed a minimum free area necessary for the molecules of 0.30nm^2 which could indicate, that in solution the sugar rings tend to bind water, which prevents the formation of tightly packed interfacial layers of $\beta - C_{12}G_2$.

The free volume model [73] assumes a linear dependence between $\ln D_s$ and the inverse of the effective mean free area a_f.

$$\ln D_s = A - \frac{B}{a_f} \qquad \textit{Equation 4.4}$$

The coefficient A yields an upper value of D_s for $1/a_f \rightarrow 0$ and B stands for the minimal critical free area a_c necessary for the displacement of a molecule. With the free volume model, we are able to approximate our data with the value of a_c = 0.29 nm^2 and obtain a decay of D_s for increasing surface coverage according to our experimental results (compare Figure 4.6 top solid line).

The reasonable fit of the experimental points and the reasonable value obtained for a_c suggest that even though the values we obtained for D_s are larger than expected, the additional driving force for molecular diffusion at the film surfaces is independent of the surfactant concentration. This force is equal for all concentrations which allow the data to be properly presented using the free volume model. We should add that the free volume model is applicable although the diffusion coefficients are orders of magnitude higher than expected. This is probably due to the inverse proportionality of diffusion and viscosity. Therefore, also any convective motion should obey the free volume model given by Equation 4.4.

4.1.7 Conclusions

The dynamics of thinning of foam films prepared from solutions of the non – ionic surfactant $\beta - C_{12}G_2$ with different concentration have been investigated. The surfactant concentration varied from 0.01 – 1.0 mM, the electrolyte concentration was kept constant at 0.2 M NaCl. Thin liquid films are formed from a drop of a liquid which contains a sufficient concentration of surfactant to stabilize the film. Under the actions of the capillary pressure and, below a certain thickness, also the attractive van der Waals disjoining pressure, the liquid from the drop is expelled, and a liquid film is formed. Studies on the velocity of film thinning supply important information about the attraction between the film surfaces (negative disjoining pressure), but also about the dynamics of the surfactant molecules on the film surfaces. We used a classical theoretical model to describe the thinning process and were able to distinguish between different regimes of thinning. The thinning can be described according to the outflow of liquid from between two rigid disks (Reynolds' thinning) at concentrations higher than 0.12 mM. The results show that the "blocking" of interfaces seems to happen at lower concentrations than the spontaneous formation of micelles at the cmc of 0.16 mM. For concentrations of surfactant below 0.12 mM, we observed an accelerated thinning due to non – zero velocity at the film interfaces. The surface diffusion coefficients we obtained follow the free volume model which suggests an increase of D_s with increasing mean area per molecule. The mobility of interfaces plays an important role for films thinner than 100 nm and thus for nanofluidic systems. The outflow velocity increased with decreasing amount of surfactant and with decreasing film thickness. These results make us able to design appropriate TLFs for studies on more complex fluid systems.

4.2 Effect of Ionic Geometry on the Force Balance (Stability) in Thin Liquid Films

4.2.1 Introduction

The classical DLVO theory predicts that the double layer electrostatic interactions (repulsion) between two interfaces (e.g. two particles in solution, two interfaces of common foam or emulsion films etc.) depend on the salt concentration and the charge (valence) of the ions which are present in the solution. This repulsive force together with the van der Waals attraction governs the distance between the two interfaces. The DLVO theory is sensitive to the charge density at interfaces, to the concentration of ions at IFs, but not to the specific interactions and ion properties like the shape of the ion. The DLVO theory describes forces which act on average in a direction perpendicular to the IFs, but does not cover forces, which act in the plane of the IFs or local structural changes at the IFs, like surfactant density fluctuations.

The main characteristic of the flow of liquids in nanofluidic applications is the length and width of the channels. If the walls of the channels are separated only by several ten nanometers from each other, one has to consider also the interactions between the channel walls to each other. The interfaces of a TLF consist of adsorbed molecules, are thus liquid like, and the molecules are moveable. The assumption that interfacial interactions may lead to oscillations with amplitudes ranging in the width of the channels and could even block those, can be discussed in analogy to the stability of TLFs.

Colloidal additives or impurities, which can be ignored in microfluidic channel dimensions, have to be studied in nanofluidic geometries. As seen in many biological and geological processes, the understanding of the behavior of water, ions and small particles in confined geometries is crucial [77]. A well – documented example from nature, the condensation of DNA, illustrates the possible influence of bulk liquid additives on adjacent interfaces.

The described events may be modeled using thin liquid free standing (foam) films. The influence of the salt concentration on the common film (CF) thickness is a standard experiment in the studies on thin liquid films. Usually monovalent salts are used [25, 27, 78-80], but also studies with ions having higher charges were performed [25, 27, 81-82] . Most of the studies confirm the predictions of the classical DLVO theory that the thickness of CF will decrease on the addition of salts to the film forming solutions. However, some exceptions were observed e.g. when Ca^{2+} salts were used. In this

case, instead of decrease in the film thickness upon the addition of salt, an increase was observed at moderate concentrations followed by decrease in the film thickness according to the DLVO theory[81]. The effects were explained with specific binding of the Ca^{2+} ions to the surfaces and a resulting increased interfacial charge until the ion concentration reached a value which compresses the diffuse double layer.

There are no studies in the literature which examine the role of the shape of the ions on the strength of the electrostatic repulsive disjoining pressure in the thin films. In the present chapter we present the results of our studies on the stability of the TLFs, with respect to the influence of the geometry of electrolyte in the film forming solution. In detail, we are interested in the role of charged, multivalent, rod – like ions on the thinning dynamics and stability of TLFs compared to those prepared in the presence of monovalent ions of the NaCl. This study may answer the question how the geometry of bulk additives can influence the stability of a nanofluidic channel.

4.2.2 Stability and Equilibrium of TLFs from $\beta - C_{12}G_2$ and Ions

A typical example of the influence of the salt concentration on the film thickness is presented on Figure 4.7 for films stabilized by the non ionic surfactant $\beta - C_{12}G_2$ in presence of NaCl to the film forming solution [16].

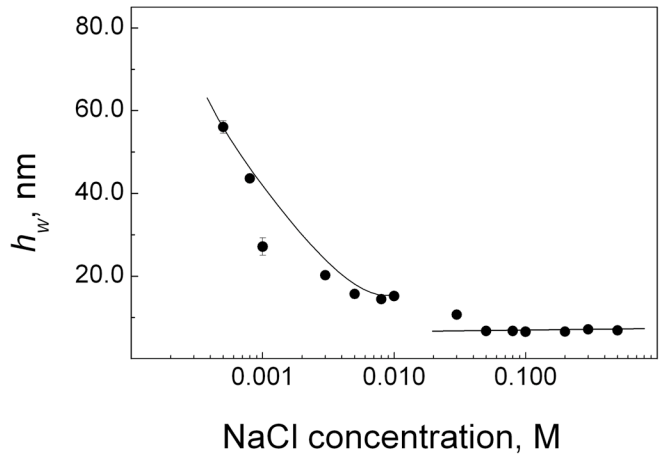

Figure 4.7 Dependence of the equivalent film thickness h_w on the concentration of NaCl. The $\beta - C_{12}G_2$ concentration is constant at $1.0 \cdot 10^{-3}$ M, measured at room temperature. All lines are only guides for the eye [16].

The thickness of the films decreases continuously on addition of NaCl in the range where common films (CFs) are formed. Above a certain salt concentration, the films are so thin that they look black in reflected light and are thus called common

black films (CBFs). Upon further addition of NaCl, only NBFs with constant thickness are formed. Between these two ranges of stable films exists a range of salt concentrations where films with intermediate thickness between those of CFs and NBFs are formed. The dependencies of film thickness and lifetime on the electrolyte concentration in the initial solutions allow one to estimate the critical electrolyte concentration at which the CF / NBF transition occurs [25 (p. 201)].

A precise look into the statistic of the experiments with these films shows that first CFs are formed. In these CFs, thinner black spots with the thickness of NBFs are formed. The probability for their formation varies with the change of the salt concentration being higher with increased salt concentration. This means that in this range of concentrations the probability for formation of either of the both types of black films is strongly dependent on small changes in the salt concentration or more generally the action of the double layer repulsion. It is already shown in the literature that the process of formation of NBFs in the thicker CFs is a stochastic process similar to the film rupture [50, 83]. Once the CFs are formed they either rupture or form more stable (lower energy) NBFs. A jump – like change in thickness is observed in Figure 4.7 at a certain concentration of electrolyte. With a further increase in electrolyte concentration, a film with a thickness of 6.6 nm is formed, which does not change in thickness.

The transition from CF to NBF reflects the transition from higher energy state to a lower energy state of the system. This transition needs certain activation energy which is related to the difference between the repulsive electrostatic double layer repulsion part of the disjoining pressure Π_{el} and the van der Waals attraction part Π_{vdW} (Figure 2.3, p.12). The activation is a result of the oscillations of the film surfaces (2.3.4 p.16) which may bring the two surfaces so close together that the contribution of Π_{vdW} is large enough to overcome the Π_{el}.

Figure 4.8 presents the change in film thickness over time showing the time it takes (respectively the probability) for formation of a NBF in the CF. The transition time τ decreases with increasing NaCl concentration from 160 min for $\tau_{NaCl\ (1.2\ mM)}$ to 25 min for $\tau_{NaCl\ (6.0\ mM)}$.

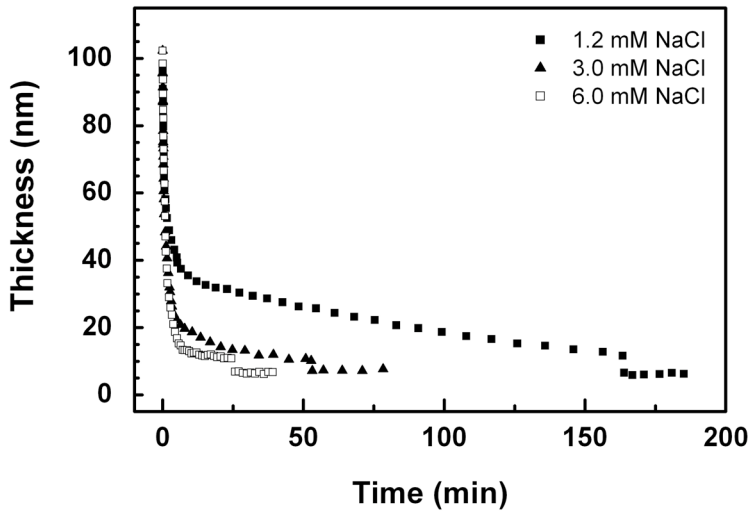

Figure 4.8 Thinning of TLFs from 0.2 mM $\beta - C_{12}G_2$ and 1.2 – 6.0 mM NaCl. The time τ_{NaCl} of transition from CF to NBF decreases with increasing concentration of NaCl; τ_{NaCl} = 160 min (1.2 mM) - 25 min (6.0 mM).

We also study the behavior of TLFs containing spermidine instead of NaCl in the solution. The results are presented as a function of the ionic strength thus avoiding inconsistencies because of the different charges of both salts. The spermidine molecule of roughly 1 nm length has the molecular structure as shown in Figure 4.9. With addition of hydrochloride (HCl), the amine groups are protonated and the product is spermidine trihydrochloride. The single positive charges are located at each ammonia end group of the molecule and one at the central amino group.

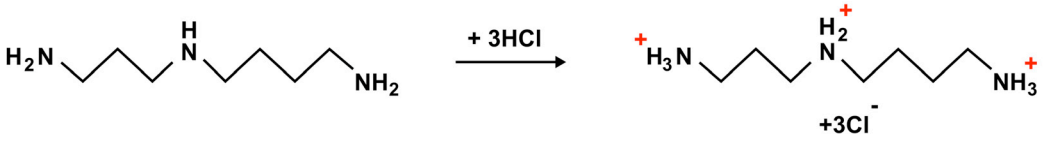

Figure 4.9 A rod – like spermidine molecule of roughly 1 nm length. With addition of hydrochloride (HCl), the amine groups are protonated and the product is spermidine trihydrochloride.

The location of the charges at the molecule account for the rod – like appearance, since bending or folding would induce electrostatic repulsion. With the pH value of the solution, we can determine the state of protonation. It is confirmed that at pH 6.6, 98% of the spermidine molecules in solution are triprotonated [84].

In presence of spermidine with the same ionic strength (I_B) in the solution as NaCl, the transition occurs immediately after the film thins or it occurs up to 10 min after the formation of a CF.

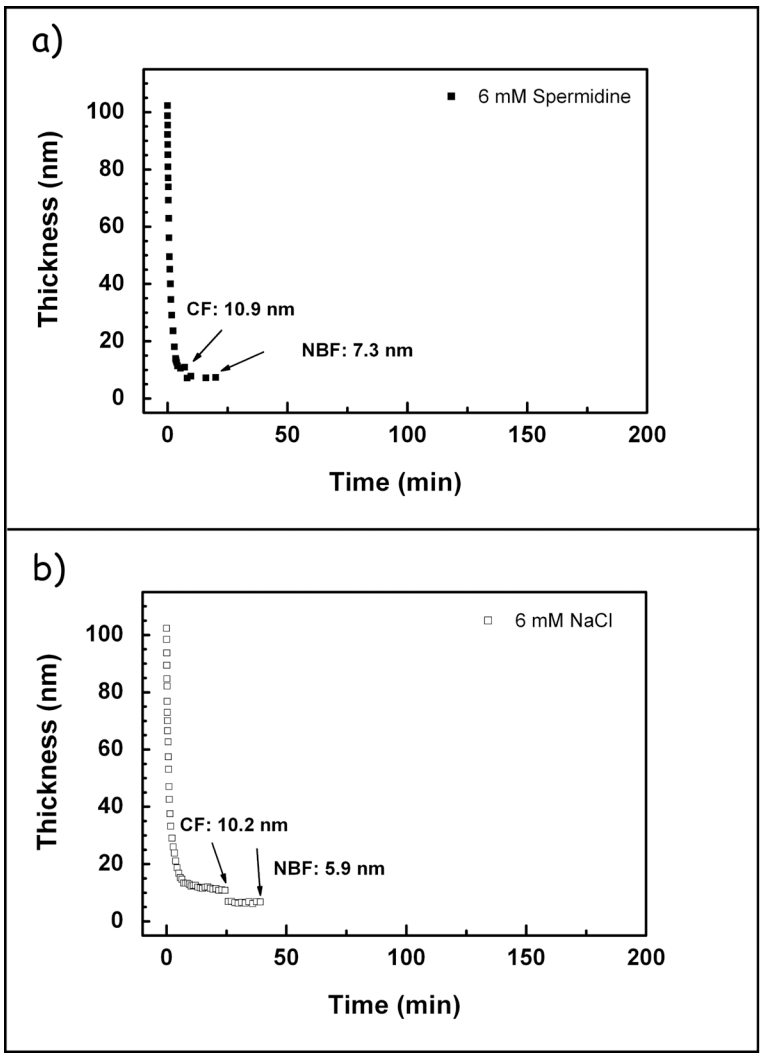

Figure 4.10 Thinning of TLFs from 0.2 mM $\beta - C_{12}G_2$ and I_B = 6.0 mM of (a) spermidine and (b) NaCl. The transition times from CF to NBF are (a) τ_{sp} = 5 min, and (b) τ_{NaCl} = 25 min.

The comparison between NaCl and spermidine is shown in Figure 4.10 (a, b). The system with spermidine has a shorter observable transition time from CF to NBF of τ_{sp} = 5 min, compared to the TLF system with NaCl τ_{NaCl} = 25 min. There might be different reasons why the transition occurs with different probabilities in both systems. One of those could be the different balances between Π_{el} and Π_{vdW} in the systems. This has to be reflected not only in a higher probability for transition from CF to NBF, but also in different velocities of film thinning, being higher for the system with lower Π_{el} (Equation 2.15, p.19).

Figure 4.11 presents two thinning curves for films with either NaCl or spermidine. Any specific adsorption of ions in interfacial layers would cause a change of the surface potential and the thickness of the diffusive double layer (change of Debye length). There is no difference in the velocity of film formation between the two cases which means that the interactions at long distances between the film surfaces are similar.

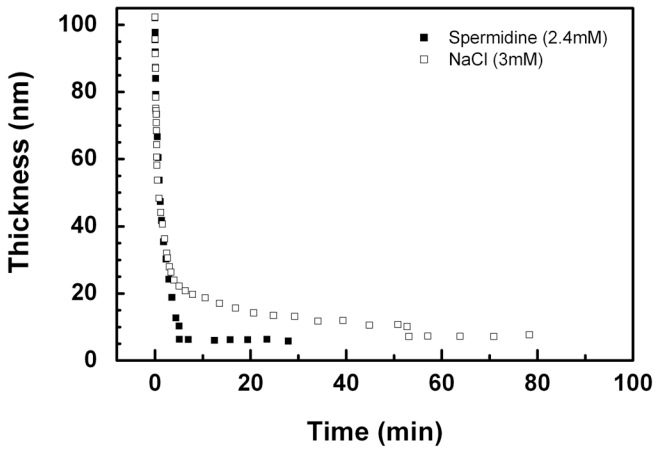

Figure 4.11 Comparison of the thinning behavior of films from NaCl and films from spermidine, each in the presence of 0.2 mM $\beta - C_{12}G_2$. The ionic strength for the solution containing NaCl is 3 mM (pH = 6.7) and for the spermidine solution 2.4 mM (pH = 6.9).

No other changes in the films are observed in the presence of spermidine compared to NaCl. The thickness of the CF and NBF are equal in the limits of the experimental error (see Figure 4.12). The CF and NBF thickness values for TLFs from 0.2 mM $\beta - C_{12}G_2$ with spermidine (filled symbols) and NaCl (empty symbols). The CF thickness is ~ 11 nm, and the NBF thickness is ~ 6 nm, independent of the concentration and valence of ions.

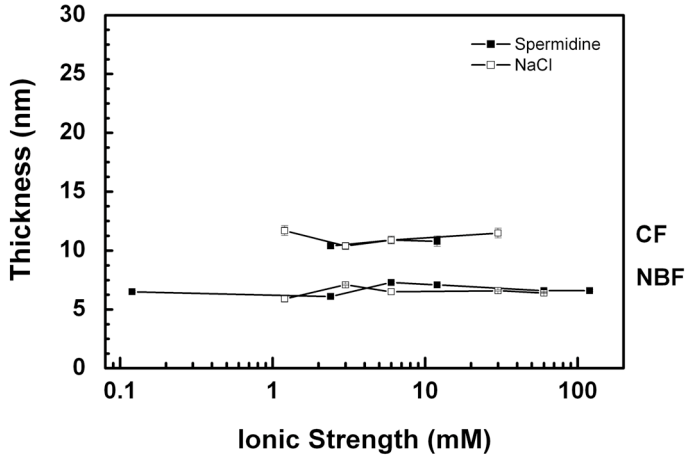

Figure 4.12 The CF and NBF thickness values for TLFs from 0.2 mM $\beta - C_{12}G_2$ with spermidine (filled symbols) and NaCl (empty symbols). The CF thickness is ~ 11 nm, and the NBF thickness is ~ 6 nm, independent of the concentration and valence of ions.

The same thickness values of CFs mean that their Π_{el} are similar. Furthermore, no difference in the steric interactions, in the case of NBFs, and the electrostatic interactions for CFs is observed. The equivalent thickness for the NBFs of h_w = 6.6 nm agrees well with literature values for the same system. We could not observe stable CFs over the whole concentration range, therefore the data for spermidine covers a smaller concentration range than the NaCl data.

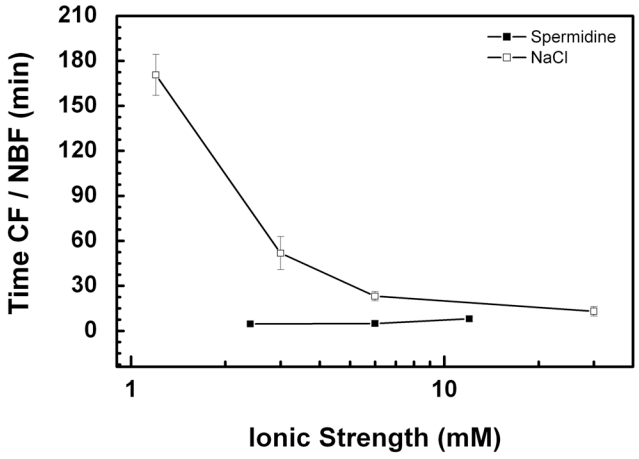

Figure 4.13 Time from I_{max} to transition from CF to NBF is τ, the transition time. For TLFs from 0.2 mM $\beta - C_{12}G_2$ and 1 - 30 mM of spermidine (filled symbols) and NaCl (empty symbols), the transition times vary between τ_{sp} = 5 min, and τ_{NaCl} = 25 min.

At all concentrations of ions, there are no stable CF formed. Surface tension data for the respective ionic strength values show maximum variations of ± 0.1 mN/m for the samples containing NaCl, and ± 0.2 mN/m for the samples containing spermidine. It can be followed, that there is no systematic difference between the interfaces of the two systems which we compare.The only difference is the huge variation in the transition time for the CF / NBF for both systems (see Figure 4.13).

Changing the type of salt is expected to strongly influence the electrostatic double layer repulsion between the film surfaces; respectively, it controls the film thickness. The electrostatic double layer potential for films stabilized with $\beta - C_{12}G_2$ in our range of concentrations is measured to be ca. 20 mV [25]. This value is sensitive to the surfactant concentration and the pH value of the solution. The interfaces of aqueous foam films reach their isoelectric point around pH 4.5 [25 (p. 143)]. This charge is a result of specific adsorption of OH- groups at the water/air interface. The non ionic surfactants compete for the same places at the interface with the OH - groups thus reducing the potential at the water interface until a certain value which remains constant independent of changes of pH < 4.5.

The Bjerrum length is less than 0.7 nm and the molecule can be treated as one with three independent charges.

The parameter most sensitive to the changes in the salt concentration is the electrostatic disjoining pressure. We have calculated it using the full mathematical formalism. The spermidine ions are electrostatically very asymmetric. They consist of one trivalent ion and 3 monovalent ions. Thus, any assumptions in the calculations are not possible and the full formulas for calculation of the electrostatic component of the disjoining pressure have to be applied. Π_{el} is given by

$$\Pi_{el} = k_B T \delta_{el1} \left(\exp\left(\frac{e \cdot \varphi_{m1}}{k_B T} \right) - 1 \right) + k_B T \delta_{el2} \left(\exp\left(\frac{-e \cdot \varphi_{m2}}{k_B T} \right) - 1 \right) \qquad \textit{Equation 4.5}$$

where δ_{el1} and δ_{el2} are the number densities of the charged spermidine ions and respectively the Cl^- counter ions in the solution.

$$\varphi_{m1} = \left(\frac{8 k_B T \gamma_1}{e} \right) \exp\left(-\kappa \frac{h}{2} \right) \text{ and } \quad \varphi_{m2} = \left(\frac{8 k_B T \gamma_2}{e} \right) \exp\left(-\kappa \frac{h}{2} \right) \qquad \textit{Equation 4.6}$$

are the potentials at the midplane of the film (compare Figure 2.2, p.9) in presence of the cations and the anions under the assumption that φ_m is small and it is a sum of the potentials from each surface at $x = \frac{1}{2} d$. The parameters

$$\gamma_1 = \tanh\left(\frac{z_1 e\varphi_0}{4k_B T}\right) \text{ and } \quad \gamma_2 = \tanh\left(\frac{z_2 e\varphi_0}{4k_B T}\right) \qquad \textit{Equation 4.7}$$

for each of the ions cannot exceed unity. The Debye length κ^{-1} is given in its full form by

$$\kappa^{-1} = \sqrt{\frac{\varepsilon\varepsilon_0 k_B T}{2e^2(z_1^2\delta_{el1} + z_2^2\delta_{el2})}} \qquad \textit{Equation 4.8}$$

with z_1 and z_2 the valences of the cations and the anions. This equation reduces to Equation 2.7 (p. 8) for symmetric electrolytes.

The transition time CF / NBF as a function of the electrostatic disjoining pressure is shown in Figure 4.14.

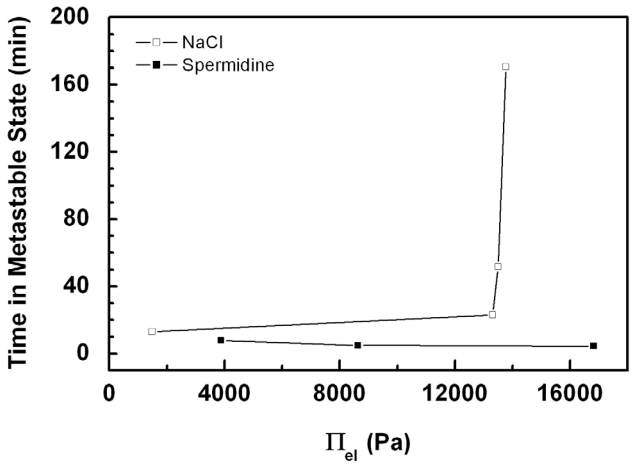

Figure 4.14 Transition time CF/NBF as a function of the electrostatic disjoining pressure.

The figure shows that up to a Π_{el} of ca. 13 kPa the time for transition of CF into NBF for both salts is similar. Above this pressure the transition stays constant low for the systems which contain spermidine, but strongly increases to hundreds of minutes in the case of NaCl. Considering that no differences in the equilibrium film structure are observed between both salts the only explanation of the observed results could be based on the influence of the ion shape on the transition of CF to NBF.

4.2.3 Classical Theory on Film Stability and Critical Rupture Thickness

We need to answer the question if local fluctuations in the CF can induce local thickness reductions in such a way that the rod – like ion, spermidine, can alter the

conditions for film stability due to their geometry. A locally thinner spot of a film will experience a substantial increase in local attractive force, which can reduce the local thickness by a great extent. Dependent on the size of the molecules and the attractive forces of the walls, such local thickness changes could favor a bridging effect of the film interfaces and promote the attractions between the film surfaces.

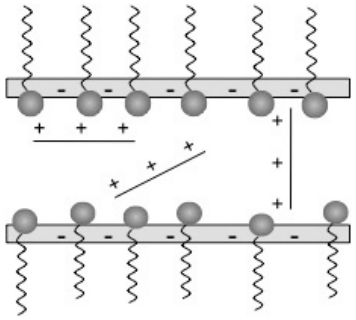

Figure 4.15 Scheme of a local spot of a TLF with negatively charged IFs. The spermidine ions are sketched as trivalently charged molecules between the film IFs. The formation of a bridge between both IFs is a potential way of arrangement.

The transformation of the equivalent thickness data into real thickness according to the three layer model, yield values of 10.2 ± 1 nm for CFs and 5.9 ± 1 nm for NBFs, thus roughly 0.6 nm smaller than the experimentally obtained equivalent thickness values. The electrostatic length of a fully stretched spermidine molecule is ca. 2.4 nm. The film interfaces are 10 nm apart. This thickness includes the thickness of the surfactant molecules which is estimated to be around 1.4 nm. Thus, the distance at which the two interfaces interact with their electrostatic double layers is 8.2 nm. Local film fluctuation as large as 3 nm may occur which can cause approach of the two interfaces at a distance of ca. 2.2 nm. That means we may have a 2.4 nm long rod in a 2.2 nm wide channel. Thus, the rod like positive spermidine ion may create a bridge between the negative surfaces of the film and accelerate the transition of CF either to NBF or to film rupture. The rod – like ions causing a bridging of the interfaces is schematically shown in Figure 4.15.

In order to get an idea about the probability of the above described bridging, one can consider that fluctuations and rod arrangements follow a Gaussian probability distribution and the above described bridging is not located in the maximum of the probabilities but rather at the edges. Therefore the events are possible. This phenomenon ranges in between long range and short range forces. There are extra electrostatic forces, which occur not in long distance as electrostatic forces usually do but in short range. The thinning passes the electrostatic long range forces phase, then the vdW

attraction forces, which get greater at thinner spots of local fluctuations. There, the vdW forces work towards a thinning of the film and in addition there is a short range electrostatic drag force, which pulls the IFs together, and forms a bridge like structure.

4.2.4 Activation Energy E_a and Energy for Hole Nucleation

We can describe the transition of a CF to a NBF as a chemical reaction. The transition will take place only when the two film surfaces come into close enough contact that the attraction between them is so strong that the local thinning defect is stable and can only be increased and a growing black spot is formed. In order to reach the state of irreversible formation of a NBF the interaction between the film surfaces has to overcome an energy barrier as shown in Figure 2.3, p.12. The activation energy is proportional to the probability for formation of NBF, respectively reciprocal to the time of stability of the higher energy state – in our case the NBF. Thus one can write [37] [38]

$$\frac{\tau_{NaCl}}{\tau_{Sp}} = \exp\left(\frac{\Delta E_{aNaCl} - \Delta E_{aSp}}{k_B T}\right) \qquad \textit{Equation 4.9}$$

where τ stands for the transition times for NaCl and spermidine, respectively, ΔE_a describes the activation energy barrier of the systems.

The equation allows us to calculate the difference in the activation energy of the transition CF to NBF in presence of NaCl and spermidine. The values are presented in Table 4.2.

Table 4.2 Results for the transition times from CF to NBF for spermidine and NaCl ions dependent on their ionic strength. The activation energy differences ΔE_a shows the different energetic probabilities of the systems. (extrapolated certain; ** extrapolated uncertain)*

Ionic Strength (mM)	τ NaCl (min)	τ Spermidine (min)	$\Delta E_{a(NaCl-Sp)}$
1.2	170.62	5**	3.5 k_BT*
1.2	170.62	8**	3.1 k_BT*
2.4	80*	4.6	2.9 k_BT*
3	51.82	4.86*	2.4 k_BT*
6	23.1	4.95	1.5 k_BT
12	19.2*	8.02	0.9 k_BT*
30	13.2	5**	1.0 k_BT*
30	13.2*	8**	0.5 k_BT*

All values are in the range of a few k_BT. This is the gain of energy of the system when the spermidine ions bridge the two film surfaces and thus accelerate the formation of NBF. The difference in the activation energies is in the range of the thermal motion at the liquid surfaces and confirms that a bridging effect can be observed in our system.

Spontaneous bridging, hole – formation, or local aggregation can occur due to temperature gradients. It has been noted in literature, that ΔT of only 0.64 K leads to a change in the film thickness of 1 nm, which can create energetically the critical conditions for the above phenomena to appear [85]. Theoretical studies on the energy of ideal systems [86-87] indicated that there is an energy gain for the system when charged rods "bridge" the gap in between oppositely charged interfaces.

4.2.5 Influence of Yttrium Chloride (YCl_3), another Trivalent Ion on the Transition CF / NBF

In order to prove the appearance of bridging effects due to the specific rod – like shape of the spermidine ions (instead of the trivalent charge), we performed experiments with YCl_3 instead of spermidine in the film forming solution. The velocity of thinning, formation of equilibrium CF and NBF and the thickness is presented in Figure 4.16. The thinning dynamics of a TLF from 0.2 mM $\beta - C_{12}G_2$ with the trivalent ion YCl_3 (I_B = 2.4 mM) is shown in Figure 4.16. The CF has a thickness of 12.7 nm and the NBF a thickness of 6.7 nm.

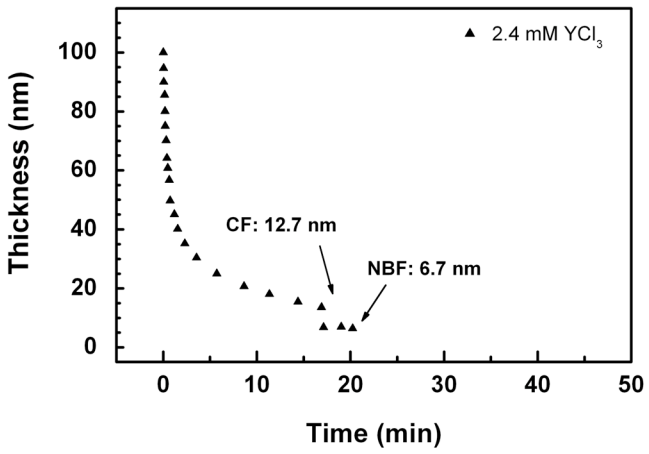

Figure 4.16 Thinning dynamics of a TLF from 0.2 mM $\beta - C_{12}G_2$ with the trivalent ion YCl_3 (I_B = 2.4 mM). The CF thickness is 12.7 nm and the NBF thickness is 6.7 nm.

The direct comparison to the NaCl (I_B = 3.0 mM) and the spermidine (I_B = 2.4 mM) system, shows a longer transition time from CF to NBF than spermidine but a shorter than in presence of NaCl. The results are summarized in Table 4.3.

Table 4.3 Transition times τ from CF to NBF for TLFs from trivalent ions YCl_3 in comparison to values from experiments with NaCl and spermidine with similar ionic strength IB. The pH – values of the film forming solutions, the NBF and CF thicknesses, as well as the diameter Ø of the glass cell, which is responsible for P_c are given.

Ion	I_B (mM)	τ (min)	pH	h (NBF, nm)	h (CF, nm)	Ø (mm)
Spermidine	2.4	4.6	6.9	6.1	10.4	4.5
YCl_3	2.4	16.0	6.5	6.7	12.7	4.3
NaCl	3.0	51.8	6.7	7.1	10.4	3.6
NaCl	1.2	170.6	7.4	5.9	11.7	4.5

Following the classical DLVO theory the probability for formation of NBF should be similar to that of the spermidine ions. The results in Table 4.3 conclude that the multivalency of the ions has an effect on the system, but the effect of spermidine is more pronounced than for other trivalent ions. In order to get the pH – values of the YCl_3 solution to be in the range of the others, some NaOH had to be added, this contribution alters the ionic strength and respectively the results for film stability. This means that indeed τ (YCl_3) must be larger than presented here and therefore, we cannot explain the enormous reduction of τ by spermidine solely by the ion valency.

4.2.6 Influence of the Sign of the Charge of the Film Surfaces on the Electrostatic Action of Spermidine Ions

We performed experiments to prove how the sign of the charges of the film surfaces may influence the occurrence of the bridging effect. We used the cationic surfactant C_{16}TAB instead of the non ionic $\beta - C_{12}G_2$. The concentration of 1mM C_{16}TAB assures the formation of positively charged surfaces instead of the negatively charged ones because of the specific adsorption of OH - ions in the case of $\beta - C_{12}G_2$.[85, 88-89].

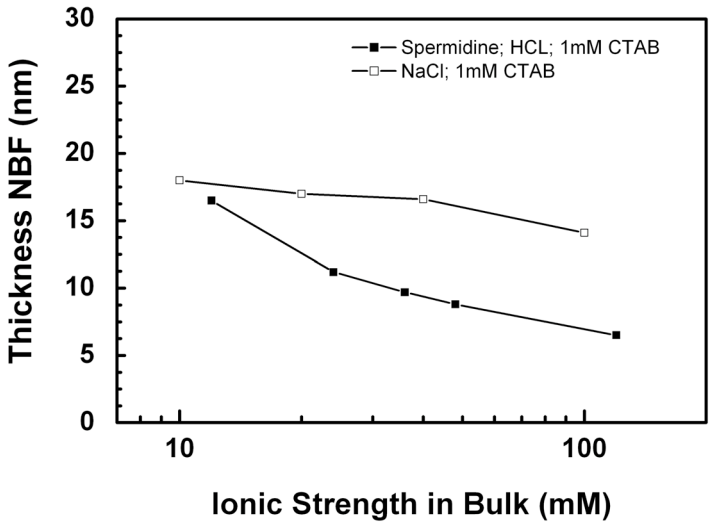

Figure 4.17 Thickness of NBF from 1mM CTAB and NaCl (empty symbols), or spermidine (solid symbols).

The results of films stabilized with C_{16}TAB show that the thickness of the CF and the NBF depends on the concentration and type of electrolyte. The results show i) no formation of a stable CFs and ii) a decrease of the NBF thickness with increasing concentration of the electrolytes. In the case of NaCl as an electrolyte, the equivalent thickness reduces from 18 nm for 10 mM to 15 nm at 100 mM electrolyte. In the case of spermidine, the trend for the thickness decrease can be observed similarly, but the impact seems much higher. The NBF thickness reduces from 16 nm to 6 nm over the described range of trivalent ion concentration. This decrease can be explained by specific interactions between the ion and the IFs, a discharging / screening of the IF according to the DLVO theory. Thus the results of this experiment are not reliable and another cationic surfactant should be investigated which can help provide the idea of bridging between the film surfaces.

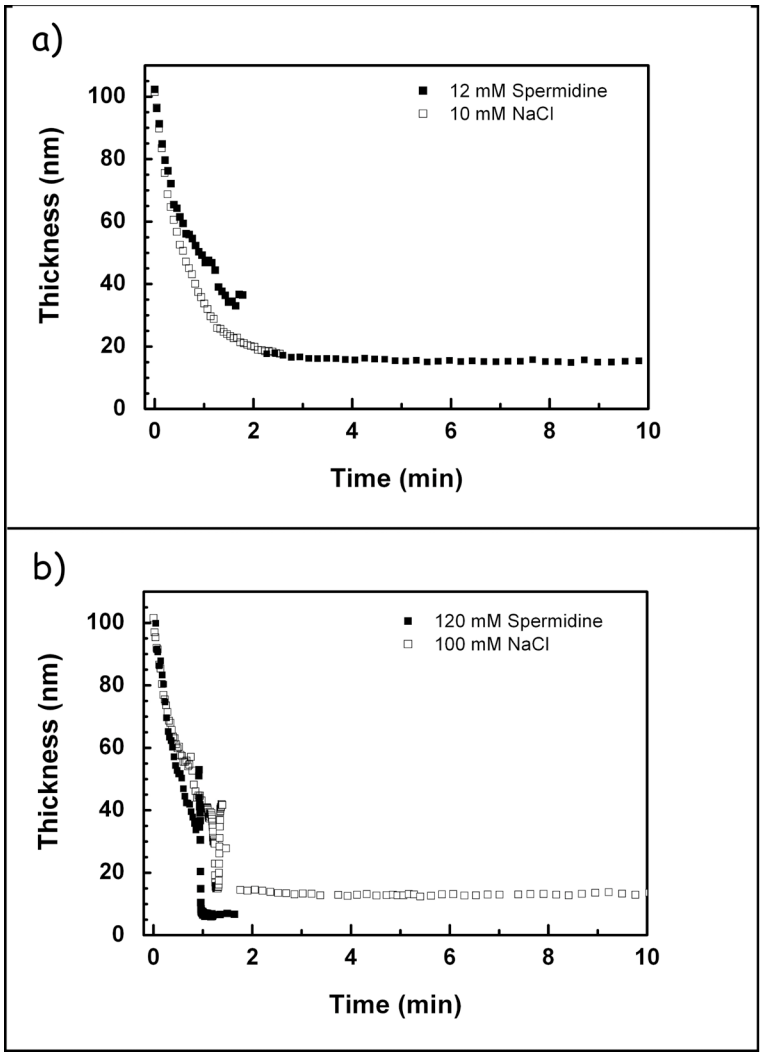

Figure 4.18 Thinnig behavior of TLFs from 1 mM CTAB and different concentrations of NaCl (empty symbols) and spermidine (solid symbols); (a) NaCl I_B = 10mM, Spermidine I_B = 12mM; (b) additionally NaCl I_B = 100mM, Spermidine I_B = 120mM

4.2.7 Conclusions

The classical DLVO theory describes the electrostatic double layer interactions between interfaces, only considering the potential of the surfaces and the influence of the concentration and charge of the dissolved ions in the liquid medium. Some later works have shown that the specific interactions between the ions and the surfaces have to be taken into account when describing the repulsion between charged surfaces. The role of the ion shape on these interactions has not been considered in details yet. The effect of some anions on the interactions in films was shown and explained on the basis of their structure – making and structure – breaking properties, while the effect of cations is exactly the reverse. The observed order of the salt effect approximately follows the lyotropic series.

We first present results in this chapter which recognize the existence of an additional attractive force in foam films based on the electrostatic interaction between rod – like ions and oppositely charged surfaces. The results show that films prepared in presence of Spermidine experience a transformation of the thicker CF to the thinnest NBF faster (with higher probability) as the films prepared with NaCl at similar conditions of electrostatic interaction. This effect is not a result of specific adsorption of any of the ions at the fluid surfaces and it does not lead to any changes in the equilibrium properties of the CF and NBF. A strong difference in the behavior of the trivalent Y^{3+} ion and the Spermidine is registered which proves the strong influence of the ion shape on the interactions.

The effect is observed when the film interfaces are separated on a distance comparable to the length of the ion. One has to expect that similar effects will be observed when nanoparticles are blocked between the film surfaces. However, one has to be aware of the osmotic effects which might occur in such systems and may overcome the “bridging effect” where energy is only of a few k_BT units. Performance of such experiments in the future would be an interesting extension of the present work.

Similar to the interactions we have reported, were recently theoretical predictions [86]. In this paper, the authors have developed a density functional theory for rod – like ions of arbitrary length, subject to an additional non – electrostatic external potential. The specific application to the case of two interacting, like – charged, planar macro ions reveals the possibility of attractive interactions, introduced entirely by correlations within the rod – like ions, rather than between them (the latter being neglected in the mean – field Poisson – Boltzmann approach). The theoretical predictions qualitatively corroborate previous findings on the interactions induced by rod – like ions that were based on a Taylor expansion with respect to the rod length [90]. We expect that our present results contribute to better understanding of the frequent rod – like structure of common condensing agents such as polyamines and certain linear peptides that are able to condense DNA [91-92] and other macro ions [93]. Theoretically, there is an attraction possible, but Poisson – Boltzmann theory does not predict attraction for point – like multivalent ions. Measurements of the contact angle of foam films could access directly the energies of interactions in the film. These measurements should be done to complement the already performed experiments.

4.3 Nanosized Particles in Aqueous Free Standing Thin Liquid Films: Fluid Dynamics and Structure

4.3.1 Introduction

Nano sized inhomogenities in channels with a thickness of few nanometers may strongly influence the flow of liquid in such systems. These for example can be the extracellular channels in living bodies or capillaries. Inhomogeneities could also be different proteins or protein aggregates, medicines or particulate systems which include Fe_3O_4 as a core. Additionally, these inhomogeneities are applicable in analytical methods due to their magnetic effect in analytical medicine as contrast enhancer e.g. for magneto resonance tomography (MRT). Because of their nanometer thickness, foam films can be used as a model to study these effects. The present chapter summarizes the results of our studies on the equilibrium and dynamic properties of foam films prepared in presence of different nanoparticles. Different types of particles were added to the film forming solution. In detail, the state of the particles in nano – confinement is of interest and is dependent on the size and concentration of particles or particle aggregates. We are interested in the question how the presence of particles influences the film properties due to confinement or flow effects. All experiments were performed with films stabilized with 0.02 mM $\beta - C_{12}G_2$ and in the presence of a high concentration of electrolyte, 0.2 M NaCl. A sufficient amount of NaCl suppresses the electrostatic double layer repulsion between the film interfaces. This assures always the formation of NBF as an equilibrium state at the end of the thinning process. The thinning behavior was analyzed with the theoretical model previously introduced (chapter 4.1, p.34 ff.).

Two different particle systems were chosen for the present analysis. The particles have to be stable at high ion concentration. The average particle diameter should lie in the range of the NBF thickness (ca. 6 nm), in order to achieve single layered particles. Commercially available magnetite (Fe_3O_4) particles with a diameter of 5 - 15 nm, stabilized by oleic acid molecules, were chosen. DLS and TEM studies showed that the diameter of the Fe_3O_4 particles is in average $\varnothing = 9 \pm 2$ nm ($5 \leq \varnothing \leq 16$ nm). As an alternative system gold nanoparticles with a diameter of 4 - 10 nm with covalently attached polymers as stabilizers were used [94]. The decisive characteristics of Au nanoparticles are due to the visibility through a light microscope because of the strong scattering.

4.3.2 Influence of Particles on Film Interfaces

The presence of particles in film forming solution (dispersion) may influence the surface tension of the bulk and respectively the characteristics of the film surfaces. This information can be interpreted as the property of the channel walls of the nanofluidic TLF system. The film forming solutions consist of the film stabilizing surfactant molecules $\beta - C_{12}G_2$, the nanoparticles (Fe_3O_4 or Au), and the particle stabilizers, fatty (oleic) acid in case of Fe_3O_4, and amphiphilic polymer chains covalently attached to the Au particles. The interfaces were designed to be moveable, according to chapter 4.1, with the constant surfactant $\beta - C_{12}G_2$ concentration of 0.02 mM. The aim of this section was to see if the particles change the interfacial dynamics.

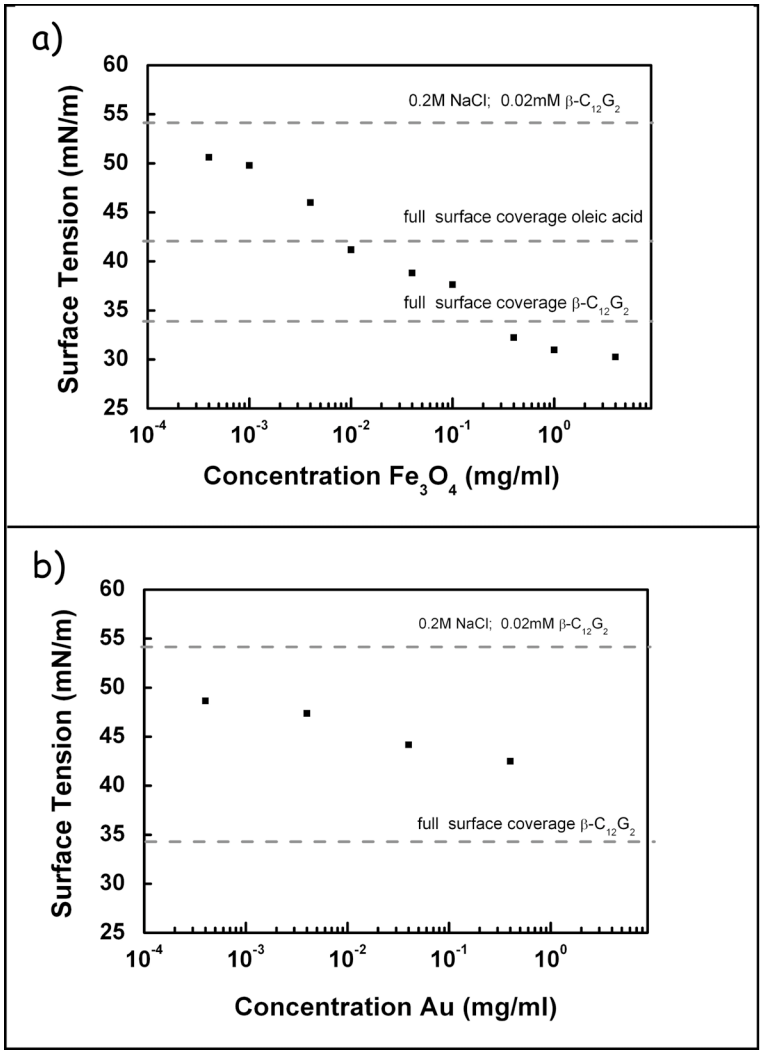

Figure 4.19: Surface tension dependent on concentration of particles in aqueous solution; the error bars are in the size range of the symbols. The concentration of non – ionic surfactant and electrolyte are 0.02 mM $\beta - C_{12}G_2$ and 0.2 M NaCl. The dotted lines indicate surface tension values for different states: σ = 54 mN/m for the surfactant/ electrolyte system without

particles, σ = 42 mN/m for the theoretical full surface coverage of oleic acid molecules (a only), and σ = 34 mN/m is the value for the full surface coverage with $\beta - C_{12}G_2$.

Different concentrations of the particle systems, Fe_3O_4 - OA or Au – polymer, were dispersed in aqueous solution. The surface tension of the used aqueous dispersions was measured at different concentrations of particles. The results are summarized in Figure 4.19. The surface tension of the $\beta - C_{12}G_2$ solution in presence of 0.2 M NaCl and 0.02 mM $\beta - C_{12}G_2$ is σ = 54 mN/m.

In Figure 4.19, the surface tension decreases for both particle systems with increasing particle concentration in the solution. The concentration of Fe_3O_4 particles ranges from $4 \cdot 10^{-4} - 4.0$ mg/ml and σ decreases down to 30 mN/m for 4.0 mg/ml particles in the solution (Figure 4.19 a). An aqueous interface fully covered with OA molecules would have the surface tension of 42 mN/m, as indicated with the dotted line in Figure 4.19 (a). The value of 42 mN/m can be derived from the pressure – area Langmuir isotherm for water insoluble monolayers which can be found in literature [95]. This lowest surface tension value of 30 mN/m is even lower than σ for a fully covered $\beta - C_{12}G_2$ interface, where σ = 34 mN/m, as seen in the previous chapter. Therefore, the decrease of the surface tension can be seen as evidence that the attachment of particles to the interface creates a further reduction of surface energy and it would be possible with the surface active stabilizing molecules. Thus the film surfaces (the “channel walls“) seem to be influenced by the addition of particles.

The Au particles were concentrated in the range of $4 \cdot 10^{-4} - 4 \cdot 10^{-1}$ mg/ml, and σ decreases to 42.5 mN/m. From the data in Figure 4.19 (b), we can see that either the Au particles or traces of the stabilizing polymer must adsorb to the interface to induce the σ decrease. Therefore, it is suggested that the particles are attached to the interface. If the decrease was due to the stabilizing polymer, the reasons must be found in the detachment of the polymer due to the condition of high ion density in the dispersion. We can argue that for all concentrations of Au particles the films are in the state of possibly moveable molecules at the interfaces.

Both particle systems show a decrease of surface tension, that means a decrease of interfacial energy. For neither of the systems, we cannot conclude, based on the surface tension data, which contribution to the surface tension decrease is due to the adsorption of particles to the interface or how much the impurities in the form of stabilizing molecules contribute. It is evident, though, that in both cases, particles “adsorb” to the interface and change the characterization of the channel wall in a certain

way, which will be essential in understanding the outflow dynamics of the dispersion from the film in the following chapter.

Compared to the Au particle system, the decrease of surface tension is much more pronounced for the OA stabilized Fe_3O_4 particles. Instead of a decrease by 7 mN/m, σ decreases for the Fe_3O_4 particles by 20 mN/m. It has been shown before that the oleic acid – stabilized Fe_3O_4 particles at the air/water interface follow Langmuir adsorption with an indication for domain formation, growth and aggregation [96-97].

This leads to the conclusion that the particles seem to have a substantial influence on the properties of our TLF IFs, and thus on the nanofluidic channel wall. For the Fe_3O_4 system, it can be suggested that the IFs are rigid – like, whereas for the Au particles, we work in the fluid – like domain.

4.3.3 Dynamic Conditions of Dispersions in Nano Confined TLFs

After the characterization of the nanofluidic channel walls by interpretation of the surface activity of the bulk dispersions, we observe here the complex fluids confined in nano sized geometry. In analogy to the experiments in the previous chapters, we prepare TLFs to generate the confinement situation, and detect with the microinterferometric method the outflow of the liquid from the film. The distance of the film interfaces, meaning the diameter of the “channel”, is similar to the experiments shown above in the range from 100 – 30 nm during outflow.

We observe outflow velocities dependent on the concentration of the added Fe_3O_4 particle system (Figure 4.20). The error bars indicate the standard deviation of the average and the theoretical fits are shown as solid lines.

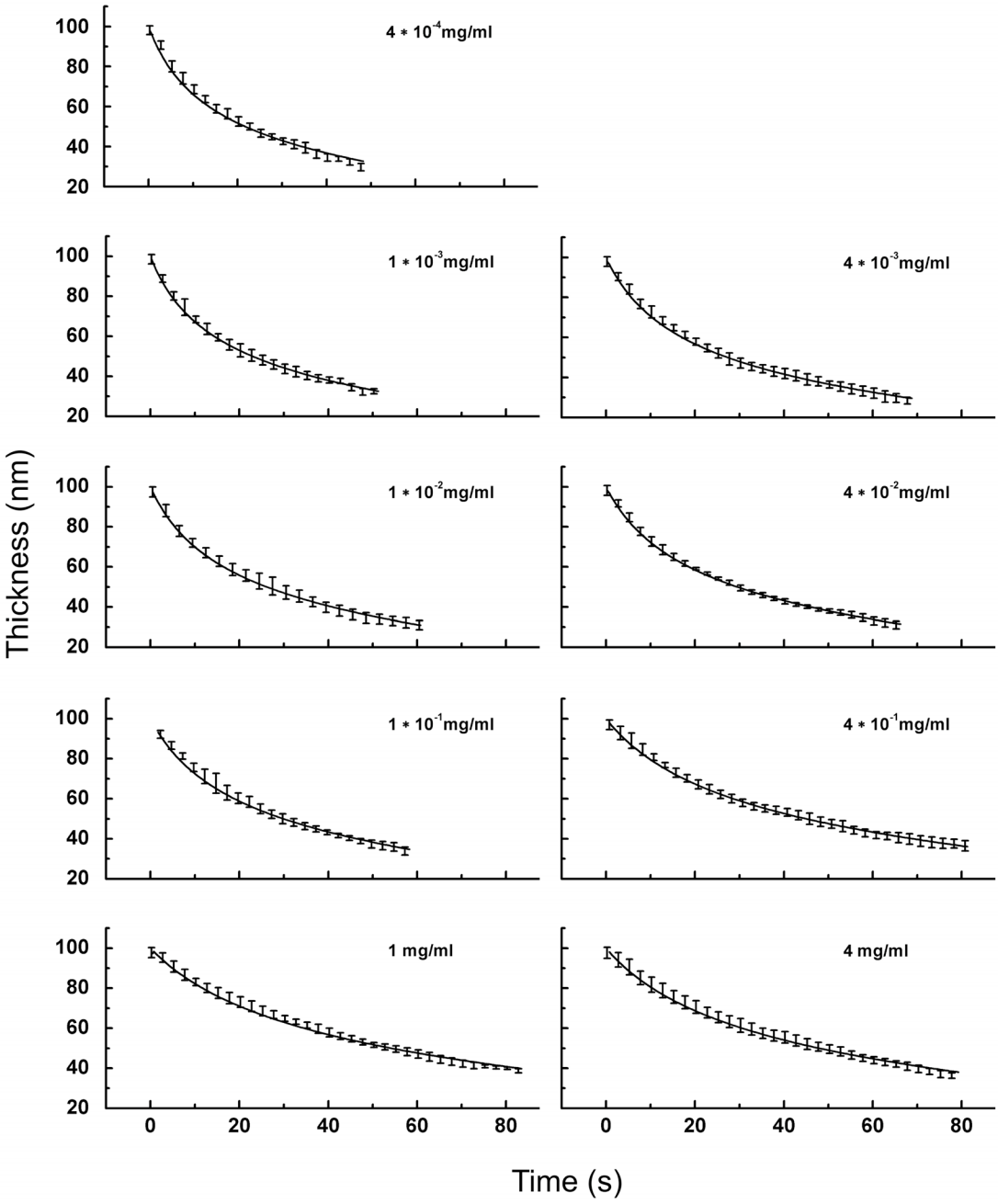

Figure 4.20 Thinning dynamics of foam films from solutions of 0.02 mM $\beta - C_{12}G_2$, 0.2 M NaCl, and concentrations of steric stabilized Fe_3O_4 particles of $4 \cdot 10^{-4} mg/ml - 4.0 mg/ml$. The result from experiments is shown as bars, the length of the line indicates the error. The solid line is the fit.

From $4 \cdot 10^{-4}$ – 4.0 mg/ml we can detect a systematic retardation of the thinning velocity. The thinning is followed until the films spontaneously become NBFs at the critical rupture thickness h_{cr}. We observe that for low concentrations, the thinning process is terminated 40 s after the final intensity maximum, whereas for the highest concentrations, the thinning takes up to 80 s until the point of the critical rupture thickness

h_{cr} is reached. A trend for h_{cr} is not in the focus of the study but it seems to become higher with increasing amount of particles in solution.

For TLFs from dispersions containing Au particles of concentrations of $4 \cdot 10^{-4}$ – $4 \cdot 10^{-1}$ mg/ml, we can obtain a dependence of the liquid outflow velocity on particle concentration (Figure 4.21).

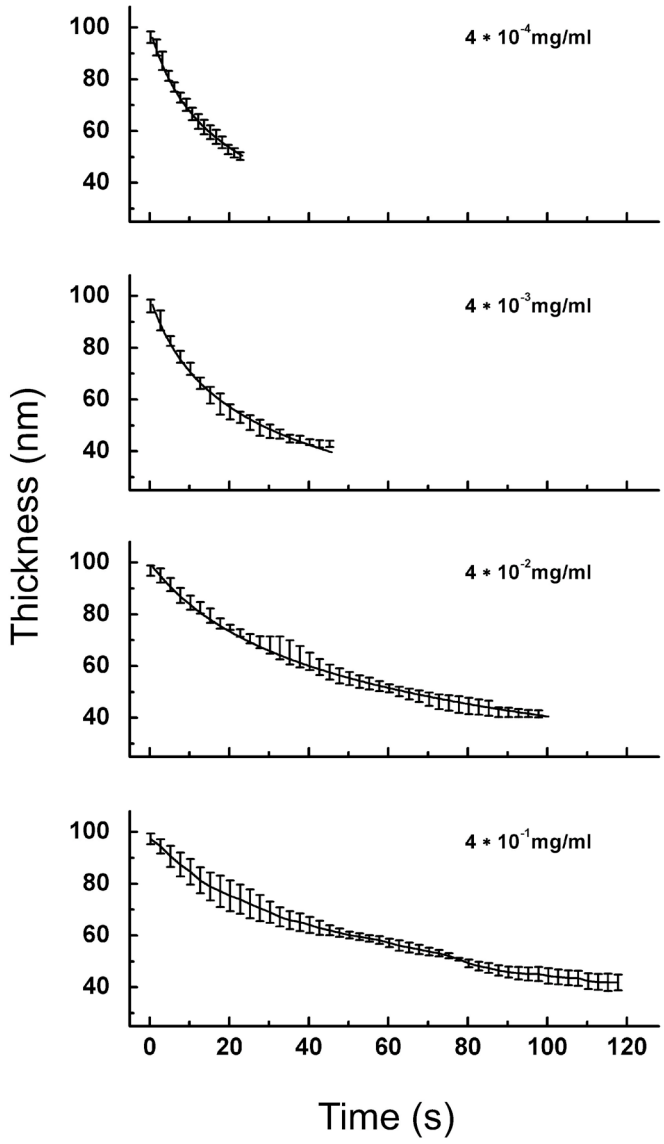

Figure 4.21 Thinning dynamics of foam films from solutions of 0.02 mM $\beta - C_{12}G_2$, 0.2 M NaCl, and concentrations of sterically stabilized Au particles of $4 \cdot 10^{-4} - 4 \cdot 10^{-1} mg/ml$. The result from experiments is shown as bars with error, the fit is indicated by the solid line.

For $4 \cdot 10^{-4} mg/ml$ we can observe the fastest film drainage, which is indicated by the fact that h_{cr} is reached after ~ 20 *s.* For $4 \cdot 10^{-1} mg/ml$ h_{cr} is reached after

~ 120 *s.* The critical rupture thickness seems to decrease systematically from the lower to the higher concentration of particles.

The qualitative conclusion from the thinning dynamics of both systems shows that for both systems the tendency is to decrease the outflow velocity with an increase in particle concentration. Comparing the behavior of films from Fe_3O_4 with those from Au, the trend of a faster thinning of the films for smaller concentration of particles is shown. These films reach the thickness of the critical point of rupture h_{cr} after a shorter time compared to films with more particles. Changes in outflow velocities have been attributed to changes in interfacial mobility (results chapter 4.1), and the question arises if this is the reason for the observations. According to the surface tension measurement results, the IFs of the films should be rigid – like for the Fe_3O_4 particle system, whereas the Au particle system should be in the fluid – like interfacial state, where a measureable amount of surface diffusivity accelerates liquid flow in the model channels.

A quantitative comparison of the values for h_{cr} , the time τ at which h_{cr} is reached between the data for the particle systems, or to the pure $\beta - C_{12}G_2$ system cannot be attempted at this stage, solely by comparing the graphs. The reason lies in the variation of σ and of the varying dimensions of the glass ring cells R_c, which determine the capillary pressure, and thus influences directly the thinning velocity.

4.3.4 Quantitative Analysis of Outflow

The theoretical approach described in chapter 4.1.4. was applied to the data, which includes parameters h and b for surface and bulk diffusion, respectively. The data could not be fitted in an agreeable way by the procedure because the film thinning velocity was slower than the proposed fitting models for all the experimental datasets. The thinning velocity of the films containing particles is slower than the lower velocity of thinning already calculated for the pure system which contains only $\beta - C_{12}G_2$. This velocity of film thinning was attributed to the formation of fully covered film surfaces which behave like rigid surfaces. The conclusion can be drawn, that the retardation must be a result of bulk rather than interfacial processes. Any further decrease of the velocity of film thinning can be attributed to changes in the viscosity of the liquid confined between the film surfaces (see modified Reynolds' Equation 2.15,p. 19). We modified the fitting function, so that b = h = 0 and an additional value for fitting was introduced, which could describe the slower liquid flow through the artificial nanochannels. Applying Reynolds' equation we could calculate the viscosity η.

The resulting fitted model curves of the liquid outflow can be obtained in Figure 4.20 and Figure 4.21, where the black lines indicate the fit of the respective experimental data which is presented as black bars.

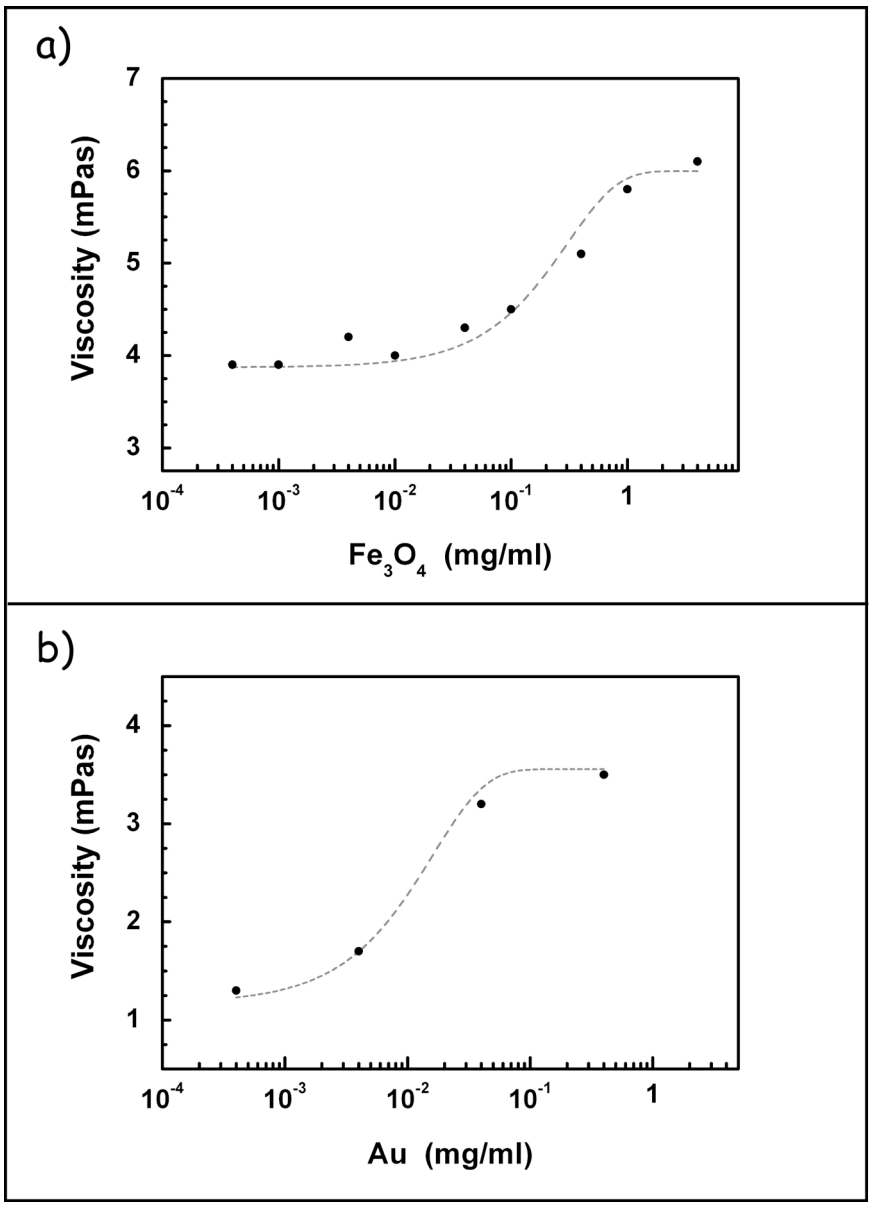

Figure 4.22 Viscosity vs. particle concentration, results from theoretical fits (black points). The film forming solutions contained apart from (a) Fe_3O_4 particles and (b) Au particles 0.02 mM $\beta - C_{12}G_2$ and 0.2 M NaCl; the grey line is just a guide for the eye.

The resulting values for η, which we obtained when fitting the experimental data, are presented in Figure 4.22, (a) for the Fe_3O_4 particle system and (b) for the Au particle system.

For the Fe_3O_4 particle system, the viscosity showed a value of 3.9 mPa s and reaches a maximum of 6.1 mPa s. The value η for the TLFs containing Au particles which we can calculate for the different amounts of particles, ranges from 1.3 mPa s for $4 \cdot 10^{-4} mg/ml$ particles up to 3.5 mPa s for $4 \cdot 10^{-1} mg/ml$ particles.

The fitting results for the Fe_3O_4 and Au particle system are presented in Table 4.4. The value for the parameter viscosity in the Reynolds formula differs for the different concentrations of particles and they are all well above the viscosity we assumed for the solution without particles, roughly the viscosity of water at room temperature.

The amount of particles, which is in the range of ‰ volume fraction, should not change the viscosity of the dispersion in a measureable range. Therefore, we assume that the increased value for viscosity does not reflect the "real" dynamic viscosity of the solution but rather structural changes inside the film. These changes could be due to particle aggregates which could be possible in the confined geometry of the film under the dynamic outflow conditions described above. The aggregates could then assemble to plugs at the meniscus film border so that the outflow gets hindered and a retardation of the thinning velocity is observed. Furthermore, the particle aggregates could flocculate and form columns in the film, effectively hindering the liquid outflow mechanically as obstacles in the liquid.

Non – Newtonian fluids, show visco – elastic properties with viscosity values dependent on the shear rate of the fluid, and therefore called apparent viscosity. The apparent viscosity of blood, which consists of roughly 50 vol % particles (cells), is provided in literature as 3 - 5 mPa s (at 37°C) [98]. Generally, a low shear rate means a high apparent viscosity, and a high shear rate means Newtonian behavior. The shape of the viscosity curve gives an indication that the increase of the apparent viscosity is stepwise, meaning that we see a significant difference between two different regimes. The concentrations where the steps occur are for Fe_3O_4 at $4 \cdot 10^{-1}$ mg/ml and for Au at 10^{-2} mg/ml. For the obtained results, this would mean that the Fe_3O_4 particle system in the channel from 100 nm thickness to 30 nm thickness never behaves like a Newtonian fluid, the Au particle system shows for low concentrations of particles values for η close to 1 mPa s, very close to the viscosity of a Newtonian fluid. Furthermore, the higher the concentration of particles in all presented solutions, the lower the surface tension and the lower the outflow velocity. This change in the outflow velocity can partially explain the presented results. This would mean that our dispersion transformed in confinement to non – Newtonian fluids, to follow the respective laws for shear flow dependent viscosity.

Table 4.4 Experimental properties and results for the experimental systems containing Fe_3O_4 and Au particles. Concentration of particles in mg/ml is given, as well as the surface tension σ, the capillary pressure P_c which acted on the TLFs, the film radius R_f, the equivalent equilibrium thickness h_w and the viscosity value obtained through the theoretical modeling process.

	Conc. Particles (mg/ml)	σ (mN/m)	P_c (N/m^2)	h_w (nm)	Viscosity (mPa s)
Fe_3O_4	**0.0004**	50.6	46.0	N.S.	3.9
	0.0010	49.8	45.3	10.3 ± 0.1	3.9
	0.0040	46.0	41.8	10.4 ± 0.4	4.2
	0.0100	41.2	37.4	10.8 ± 0.1	4.0
	0.0400	38.8	35.3	10.3 ± 0.1	4.3
	0.1000	37.6	34.2	10.2 ± 0.2	4.5
	0.4000	32.2	29.3	11.2 ± 0.1	5.1
	1.0000	31.0	28.2	10.3 ± 0.1	5.8
	4.0000	30.3	27.5	10.5 ± 0.1	6.1
Au	**0.0004**	48.7	51.2	N.S.	1.3
	0.0040	47.4	49.9	10.3 ± 0.1	1.7
	0.0400	44.2	40.2	(26.8 ± 0.3*)	3.2
	0.4000	42.5	38.6	10.8 ± 0.1	3.5

* The measurements were aborted before the equilibrium thickness could be observed.

N.S.: The films did not reach an equilibrium thin film but were not stable and ruptured.

Studies with comparable nanoparticle systems suggest that drastic thinning retardations cannot be described by a simple modification of the value of the dynamic viscosity [99]. They present further the picture of a traffic jam which finally leads to the formation of nanocomposite corks that occupy the entire section of the Plateau border for the dispersions displaying “oligomeric” aggregates. Their work considers dispersions with particle concentrations around 1 wt %, which is substantially above our parti-

cle concentration range. In the paper, they give a qualitative explanation for the seemingly two – step mechanism of traffic jam formation: First, small native “oligomeric” aggregates, which are mainly present in the bulk of the plateau borders, grow for a low gradient of flow velocity in the plateau border section by successive adhesive collisions in the node crossing region. Second, when the as – formed aggregates reach a size close to the channel diameter, the liquid flow is rapidly entirely locked by a nanocomposite cork. The films are stabilized by the hydrophilic aggregates according to an entrapment / flocculation process driven by film drainage and closure. This picture could explain the difference in the particle systems between Fe_3O_4 and Au particles, which show that the differences in the apparent viscosity for the lowest concentrations of particles differ by a factor 4. We can assume that Fe_3O_4 has a larger tendency than Au to form aggregates, so that the flocculation and aggregation of the system could explain the differences.

4.3.5 Static Conditions

We used the high scattering ability of Au particles and observed the equilibrium state optically. As shown in Figure 4.23, we obtained bright spots randomly distributed in the films. The bright spots are possible particle aggregates, which shine bright in the microscope's light. The absolute size of the aggregates cannot be shown from the radius of the shining spots. They should be much smaller. A feature which we could obtain is that the spots move due to thermal Brownian motion. The Fe_3O_4 particles in the TLFs provided no optical indication for formation of inhomogenities.

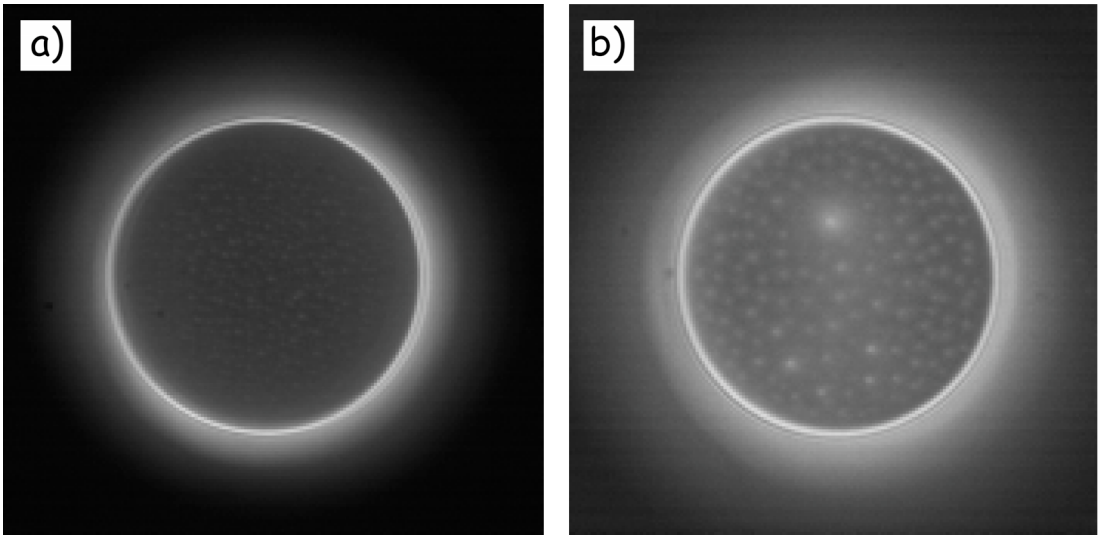

Figure 4.23 TLFs (radius 70 ± 3 µm) from 0.02 mM $\beta - C_{12}G_2$, 0.2 M NaCl, and (a) 0.04 mg/ml , and (b) 0.4 mg/ml Au particles.

It remains unclear if bigger aggregates are formed due to higher local temperature in the film from brighter light or if they result from a higher local particle concentration. It is important to recognize the temperature sensitivity of the particle stabilizing polymers. Directly under the pinhole, where the temperature is higher than elsewhere in the film, the particles tend to agglomerate (=bright spot). It has been noted earlier [85] that local aggregation can occur due to temperature gradients and that ΔT of only 0.64 K can lead to a change in the film thickness of 1 nm, creating energetically the critical conditions for particle aggregation.

It has recently been noted for a different particle – film system, that a striking liquid fraction measured in the presence of particles at the end of the free – drainage experiments may correspond in a significant manner to the residual water entrapped in the swollen films [99]. This could explain the higher equilibrium film thickness of films containing particles, in contrast to films without particles under the same energetic conditions. Nevertheless, the question if particles stay in the film remains, and if yes, which structure they form cannot be completely answered. The equilibrium film thickness for both systems and the fact that we can optically observe aggregates in the Au films supports the idea of an existence of particles in the film, nevertheless in Ref [61] it is shown that if at least one layer of particles stays in the film then black spot expansion does not occur. That would mean we loose all particles in the Fe_3O_4 film, whereas, the author speaks of films where stratification appears, where a much higher concentration of particles is necessary.

The values for equilibrium thickness are presented in Table 4.4. Between the particle systems the final equilibrium thickness is similar despite the optical differences which can be observed above. In comparison to the films without particles, the final thickness differs and shows a ~ 4 nm increase (between 6.6 nm for films without particles and ~ 10.6 nm for films with particles). This leads to the assumption that the smallest of the particles could remain in the film, which we will study in the following chapter.

4.3.6 Conclusions

The results presented in this chapter demonstrate that inclusion of nano – sized objects in the thin nanofluidic channel will strongly influence the flow in the channels. This result is very well pronounced and cannot be attributed to some specific to the foam film details (e.g. the mobility of the film surfaces which might be influenced by the presence of minor contaminations of surfactants). The results show that even the addition of small amount of nanoparticles to the film forming solution decreases

drastically the velocity of film thinning. This effect may have strong impact not only in the field of fluidics but also is very important for applications when preparation of stable particulate foams is looked for.

An interesting result is the observation that the viscosity of the liquid fixed between both film surfaces increases with the concentration of the particles. This result was expected and already predicted by the Einstein's formula for the viscosity of suspensions

$$\eta = \eta_o(1 - 2.5\vartheta) \qquad \textit{Equation 4.10}$$

where η is the viscosity, η_o is the viscosity of the dispersion medium and ϑ is the volume fraction of the dispersed phase. The formula predicts continuing increase of the viscosity when the fraction of particles increases. This relation cannot explain the step wise shape of the curves presented in Figure 4.22. Such a shape should prove the changes in the film structure on addition of the particles.

We find that the picture suggesting that nanocomposite corks are formed in the thin channels [99] might be used to explain the behavior of our thin foam films. This can be supported by the observations with equilibrium films which are thicker than the films without particles. There are two possibilities for the increased thickness – either the particles are adsorbed at the film surfaces or they stay between them just blocked there by the strong capillary forces acting there. This fine structure of the films can be elucidated only using contemporary physical techniques like GISAXS. As the changes in the surface tension are comparatively small we may conclude that most probably the particles are blocked between the two surfaces of the film. This may create an additional osmotic pressure which tends to disjoin the film surfaces, respectively to increase the thickness of the equilibrium films. The presence of such osmotic components can also contribute to the effect of slowed down flow of the liquid out of the films.

4.4 Preliminary Results to the Structure of Free Standing Liquid Films from $\beta - C_{12}G_2$ Containing Fe_3O_4 Nanoparticles using Neutron Reflectometry (NR) and Grazing Incidence Small Angle X – Ray Scattering (GISAXS)

4.4.1 Introduction

Stabilization of liquid films with nanoparticles is an important new area of studies with foam films. The use of chemically inert particles allows formation of dispersions (foams, emulsions) which can be used in different pharmaceutical applications or development of new materials. Previous studies showed that neutron reflectometry is a suitable tool to study the internal structure of foam films[100]. The selective sensitivity to the surfactant molecules and D_2O used as aqueous phase, assure good contrast between the foam film layers. We aim to clarify the structure of foam films stabilized with nanoparticles. NR will be used to investigate the position of the particles in the film, whether they are included in the aqueous core or attached (adsorbed) to the film surfaces. In the next step, the scattering signal from the films will be collected and information about the in – plane organization of the particles will be investigated.

4.4.2 Profile analysis of complex foam films via Neutron Reflectometry

With the NR technique, we examine aqueous TLFs with amounts of Fe_3O_4 - OA from 0 – 1 mg/ml. The solutions were based on D_2O to give contrast in the measurements to the particles. The reflectivity curves for films prepared with different concentrations of Fe particles are presented on Figure 4.24. A slight difference can be observed between the samples without particles, indicated as triangle shaped symbols, compared to the sample with the highest amount of particles (filled squared symbols).

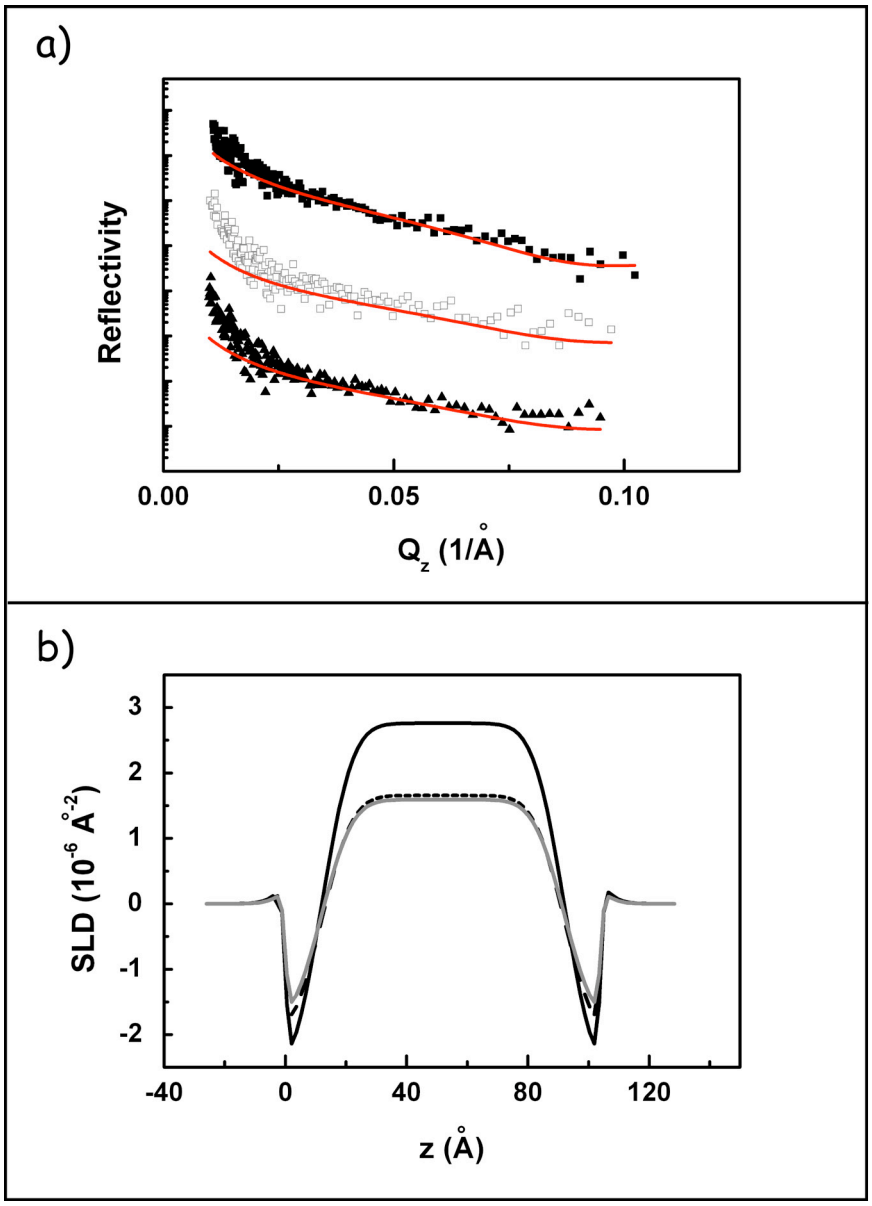

Figure 4.24 Neutron Reflectometry experimental and model data from large foam films containing 0.4mM $\beta - C_{12}G_2$, 0.2 M NaCl, 25% glycerol and Fe_3O_4 particles of different concentrations. (a) Experimentally obtained reflectivity vs. q_z for 0 mg/ml Fe_3O_4 (triangles), 0.1 mg/ml Fe_3O_4 (empty squares), and 1 mg/ml Fe_3O_4 (filled squares). The fits are presented as solid lines. (b) The scattering length density (SLD) profile for the respective samples: 0 mg/ml Fe_3O_4 (grey solid line), 0.1 mg/ml Fe_3O_4 (black dotted line), and 1 mg/ml Fe_3O_4 (black solid line).

The presented results show the q_z range of 0 – 0.1 Å^{-1}. Assuming a thickness of roughly 10 nm for the film thickness, meaning the reflective planes of the neutron beam, we would expect to see the first fringe according to the Bragg law at ca. $q_z = 2\pi / 100$ Å = 0.06 Å^{-1}. This value is in the range of background scattering for the experiment and no further detailed information could be drawn from the experimental

data due to the inability to detect any fringes in the reflectivity curves.

When we consider reflections Z_1 and Z_2 from the two film interfaces which are very noisy or rough, and consider $Z_1 + Z_2$, the interference result of the detected reflection will affect mostly the location and the distinct visibility of the minima of the fringes, more so than the height of the fringes e.g. the integral under the fringes. The position of the maxima will also be moved, so that a determination of the distance of such rough layers will not be possible without substantial error.

The fitting of the data was possible even though the data have to be accepted very cautiously because of the limitations of the technique we already discussed. The best fits are presented as lines in Figure 4.24 (a). The fitting parameters are summarized in Table 4.5. The obtained scattering length density (SLD) profiles are given in Figure 4.24 (b).

We assume that the thickness values obtained for this sample with the TLF / Micro – interferometric method holds true and use the film thickness of 10.4 nm, including an adsorption surface layer of 1.2 nm and a core of 8 nm with 10% roughness. With these assumptions, we obtain a reasonable trend for the value of the SLD of the layers but unreasonable quantitative values considering the error regimes we obtained.

Table 4.5 NR fitting results with two and one box symmetrical model; SLD and layer thickness d are given dependent on the concentration of Fe_3O_4 particles; the roughness of each layer was assumed to be 10% of h.

Two Box Model

		0 mg/ml Fe_3O_4	*0.1 mg/ml Fe_3O_4*	*1 mg/ml Fe_3O_4*
Interfacial Layer	*d (nm)*	1.2	1.2	1.2
(L 1)	*SLD (10^{-6} Å^{-2})*	- 1.9	- 2.1	- 2.8
Bulk Layer	*d (nm)*	8.0	8.0	8.0
(L 2)	*SLD (10^{-6} Å^{-2})*	1.6	1.7	2.8

One Box Model

		0 mg/ml Fe_3O_4	*0.1 mg/ml Fe_3O_4*	*1 mg/ml Fe_3O_4*
TLF	*d (nm)*	10.4	10.4	10.4
Box 1	*SLD (10^{-6} Å^{-2})*	1.0	1.1	1.8

When calculating theoretically the SLD values according to the volume fractions of the substances, which we have in the solutions, and the respective SLD values for the pure substances (compare Table 4.6), we would expect substantially different quantitative values for the SLD of the system.

Table 4.6 SLD values for the pure substances used in NR experiments. The SLD values for the hydrophobic chains of $\beta - C_{12}G_2$ can be found in Ref [101]

Substance	*SLD (10^{-6} Å^{-2})*	*Density (g/cm^3)*
D_2O	6.36	1.106
H_2O	- 0.56	0.9982
Fe_3O_4	6.84 – 6.97	5.1 - 5.2
Glycerol ($C_3H_8O_3$):	0.61	1.26
Oleic Acid ($C_{18}H_{34}O_2$)	0.08	0.89
$C_{10}H_{21}$	- 0.41	- - -
$C_{10}D_{21}$	7.04	- - -

Calculations of the SLD for the different layers according to simple lever principle resulted in $4.93 \cdot 10^{-6}$ Å^{-2} as assumed SLD value for the bulk layer from D_2O, glycerol, and a concentration of surfactant which does not influence this value. The addition of maximum 1 vol % OA and $\beta - C_{12}G_2$ would reduce the SLD to $4.87 \cdot 10^{-6}$ Å^{-2}. The impact of additional Fe_3O_4 in the bulk would rise SLD values, not lower them, as the results predicted. This leads us to the conclusion that we cannot trust the quantitative results of the measurements. The fact, what we can believe is that we can clearly see a trend which supports the idea that there are particles in the film. However, where and to what concentration we cannot tell from the data. A fitting with the option of a small aqueous bulk and a layer of particles at the interfaces gave no better results; some of the data we were not able to fit.

The relevance of the different SLD results, can be assessed by considering the error made in the fitting process. According to Table 4.6, the SLD values differ between 0 and 0.1 mg/ml Fe_3O_4 by $\Delta SLD_1 = - 0.2 \cdot 10^{-6}$ Å^{-2} for L1 and $\Delta SLD_2 = 0.1 \cdot 10^{-6}$ Å^{-2} for L2. (The difference between 0.1 mg/ml Fe_3O_4 and 1 mg/ml Fe_3O_4 is $\Delta SLD_1 = - 0.7 \cdot 10^{-6}$ Å^{-2} for L1 and $\Delta SLD_2 = 0.6 \cdot 10^{-6}$ Å^{-2} for L2.) For the error calculations we

allow L1 to vary by 0.2 nm and L2 by 0.8 nm. The film thickness L1 + L2 can vary ± 0.4 nm. Internal SLD differences, assuming a stable film thickness of 10.4 nm gave the error ranges for L1 of $\Delta SLD_1 = -1.2 \cdot 10^{-6}$ Å^{-2} and for L2 $\Delta SLD_2 = 0.06 \cdot 10^{-6}$ Å^{-2}. This means that we can obtain a systematic change for SLD_2 in our measurements. The maximum error if also the total film thickness can vary, we receive an error for L1 of $\Delta SLD_1 = -1.4 \cdot 10^{-6}$ Å^{-2} and for L2 $\Delta SLD_2 = 0.2 \cdot 10^{-6}$ Å^{-2}. Both error regimes are larger than the absolute change of SLD between L1 and L2, thus we cannot believe the absolute content of Fe_3O_4 in the film and we have to consider these results as preliminary.

4.4.3 Study of In – plane Structure and Arrangement of Particles via Grazing Incidence Small Angle X – Ray Scattering (GISAXS)

The GISAXS technique is a powerful technique to analyze the in – plane structures of different samples. It was applied for the first time to study free standing thin liquid films. The TLF without any additional particles was examined as the reference to a TLF from 0.4 mM $\beta - C_{12}G_2$, 0.2 M NaCl, 25% glycerol and 0.6 mg/ml Fe_3O_4 particles. The scattering signals of films without particles, as well as reference measurements of the measurement cell and frame without film can be seen in Figure 4.25. The background measurements (a1) and (a2) of the measurement device (cell and empty frame without TLF) are presented. The 2D image intensity distribution is transformed into reciprocal space. q_z is the wave vector component perpendicular to the sample surface and q_y the component parallel to the surface and perpendicular to the x – y scattering plane. The intensity is shown on a logarithmic scale. The colors blue / dark correspond to low intensity and pink / white correspond to high intensity. The measurement times were a_1 ~ 30s and a_2 ~ 600s (=10min). No intensity peak besides the direct beam, shielded by the beam stop, is visible in the detector field. Figure 4.25 (b) shows the 2D scattering pattern of a TLF without particles and measurement time of 45 seconds. No out – of plane scattering, but an intensity distribution in the scattering plane is visible. Out – of – plane cuts of the detected signal from the TLF without particles ((c), empty symbols) measured for 45 s is shown, in the same graph a measurement for 10 s of the film with particles (filled symbols). Despite a short measurement time of 10 s, distinct peaks in the out – of – plane cut of the spectrum from the particle loaded film (filled symbols) can be observed. In contrast, the film without particles (empty symbols) in the same figure, was measured for longer time, 45 s, and no peaks are visible in the off – specular cut. This means, that even for very short measurement times, the spectra of TLFs with and without particles are distinctly different.

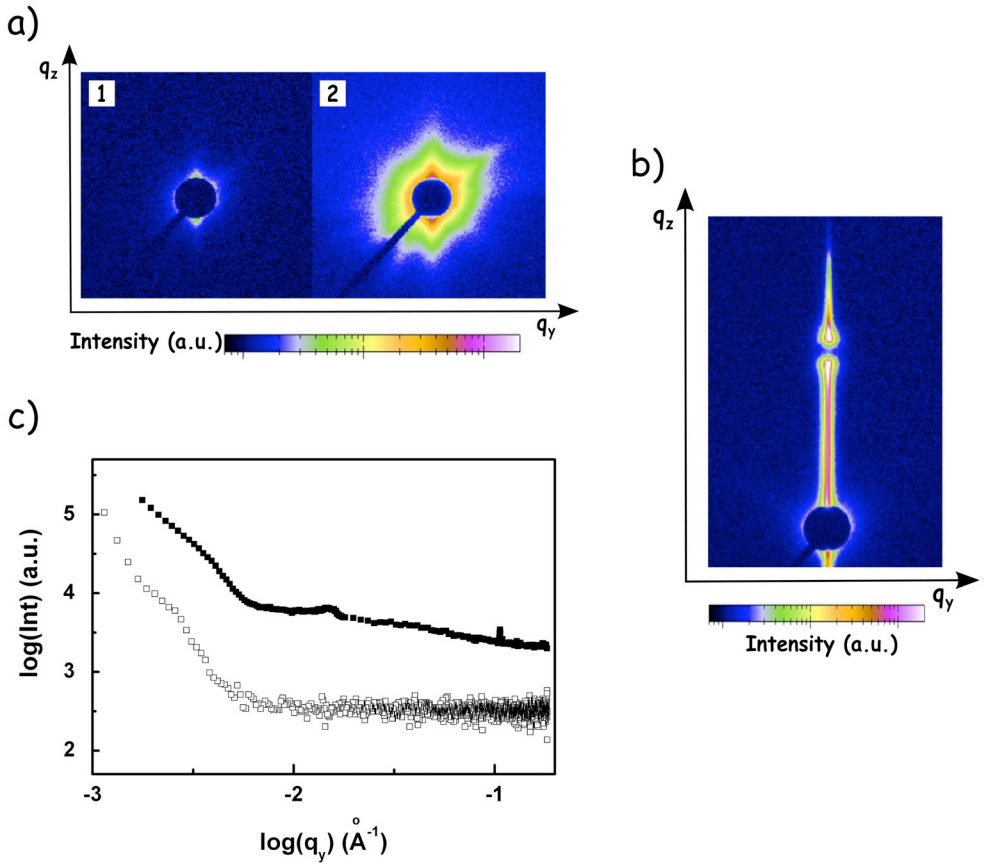

Figure 4.25 (a) Background measurements a1 and a2 of the measurement device (cell and empty frame without TLF). The 2D image intensity distribution is transformed into reciprocal space. q_z is the wave vector component perpendicular to the sample surface and q_y the component parallel to the surface and perpendicular to the x – y scattering plane. The intensity is shown on a logarithmic scale. For color coding, see the scale bar (blue / dark corresponds to low intensity and pink / white corresponds to high intensity). Measurement time: a_1 ~ 30s and a_2 ~ 600s (=10min). No intensity peak besides the direct beam, shielded by the beam stop, is visible in the detector field. (b)) 2D scattering pattern of a TLF without particles, measurement time: 45 seconds. No out – of plane scattering, but an intensity distribution in the scattering plane visible. (c) Out – of – plane cuts of the detected signal from the TLF without particles (empty symbols) measured for 45 s; in the same graph a measurement for 10 s of the film with particles (filled symbols).

We measured the TLF with particles for a measurement time of 63 minutes and the result is shown in Figure 4.26. The scattering signal in the out – of – plane region can be seen as vertical straight lines parallel to the q_z direction. We can observe a distinct signal close to the scattering plane (Figure 4.26 (c)) and on the left hand side a brighter area (Figure 4.26 (b)). The slight asymmetry of the scattering pattern can be attributed to the sagging of the film inside the frame, thus representing a slightly curved

surface on which the X – ray beam impinges.

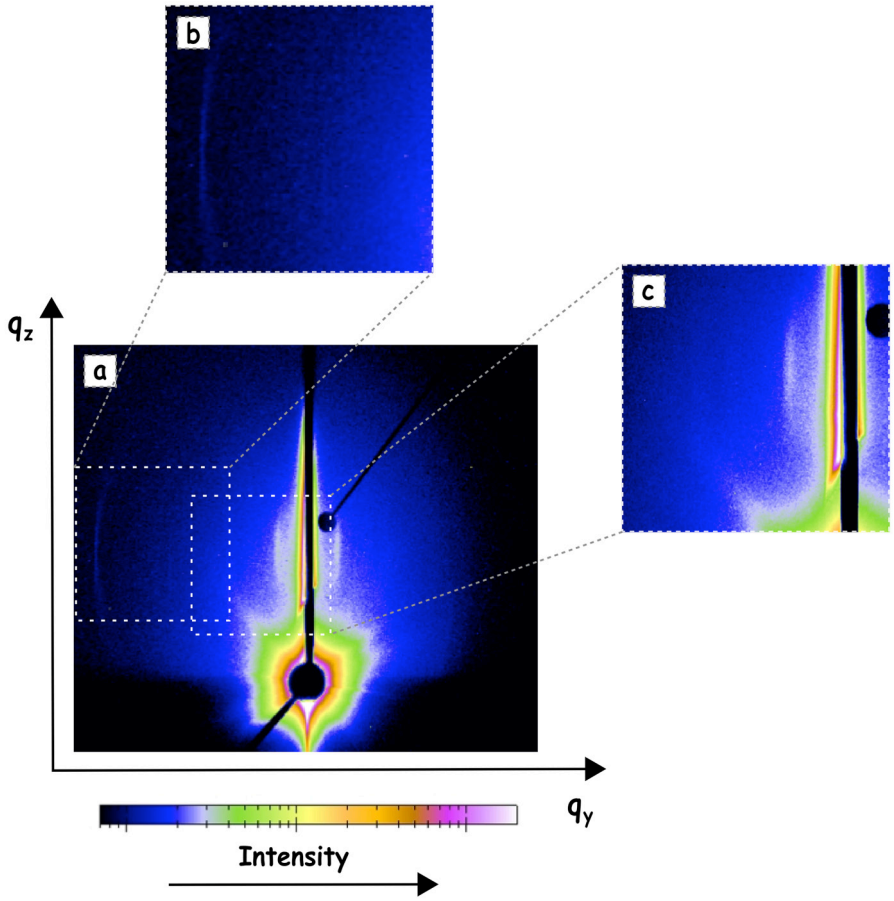

Figure 4.26 (a) 2D scattering pattern of the TLF sample containing particles. The 2D image intensity distribution is transformed into reciprocal space. The q_z is the wave vector component perpendicular to the sample surface and q_y the component parallel to the surface and perpendicular to the x – y scattering plane. The intensity is shown on a logarithmic scale. For color coding, see the scale bar (blue / dark corresponds to low intensity and pink / white corresponds to high intensity). (b) and (c)are enlarged details of off – specular scattering intensity peaks.

A horizontal cut through the 2D intensity distribution (Figure 4.26 (a)) is shown in Figure 4.27. The data is presented mirrored at the scattering plane, for the sake of data analysis. The cut only depends on the wave vector component q_y and the two distinct intensity peaks are located at q_y = 0.015 $Å^{-1}$ and q_y = 0.107 $Å^{-1}$. The experimental data is shown as black squares and the fit of the data is indicated as a red line.

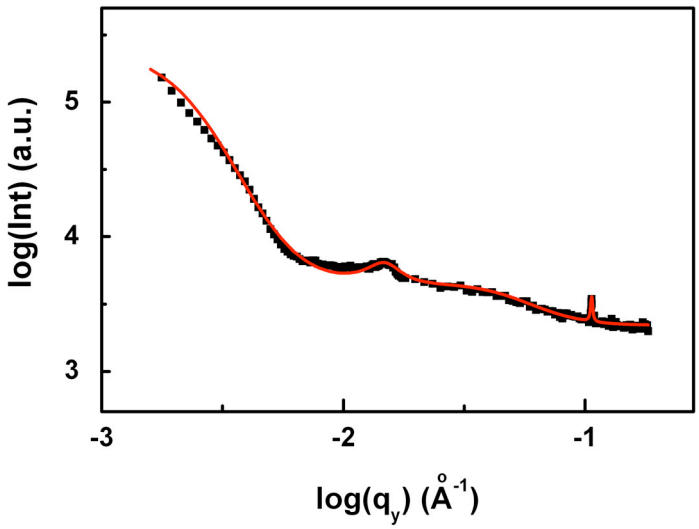

Figure 4.27 Out – of – plane scan cut from the 2D intensity distribution in the reciprocal space. Two distinct intensity peaks are located at q_y = 0.015 Å^{-1} and q_y = 0.107 Å^{-1}. The experimental data is shown as black squares and the fit of the data via Effective Surface Approximation (ESA) is indicated as a red line.

The data analysis, via *Effective Surface Approximation* (ESA) (details in chapter 3.1.3, p.26 and Ref [66]) provides the evidence of the presence of repeating units with characteristic length scales of 45nm and 6 nm. The pronounced peak at q_y= 0.107 Å^{-1} results from the characteristic size of the smallest particles present in the film. The obtained characteristic length of 45 nm, is interpreted as the mean distance of the particles in the film. The appearance of this latter peak thus indicates ordering of the particles even at low concentrations, probably due to a long – range repulsion.

5 SUMMARY AND OUTLOOK

With the rise of nanotechnology in the last decade, nanofluidics has been established as a research field and gained increased interest in science and industry. In medicine and biology, where e.g. intracellular processes are of nanofluidic nature, more and more open questions arise concerning the detailed understanding of the nanofluidic background. However, nanofluidic applications require a full understanding of the nanofluidic system. Natural aqueous nanofluidic systems are very complex, there is often a predominance of liquid interfaces or the fluid contains charged or differently shaped colloids. The effects, promoted by these additives, are far from being completely understood and interesting questions arise with regards to the confinement of such complex fluidic systems.

A systematic study of nanofluidic processes requires designing suitable experimental model nano – channels with required characteristics. The present work employed thin liquid films (TLFs) as experimental models. They have proven to be useful experimental tools because of their simple geometry, reproducible preparation, and controllable liquid interfaces. The economic advantages of TLFs as model systems are the cost efficiency and simple way of producing nanometer channel geometries. The thickness of the channels can be adjusted easily by the concentration of electrolyte in the film forming solution. This way, channel dimensions from 5 – 100 nm are possible, a high flexibility for an experimental system. TLFs have liquid IFs of different charge and properties and they offer the possibility to confine differently shaped ions and molecules to very small spaces, or to subject them to controlled forces. This makes the foam films a unique “device” available to obtain information about fluidic systems in nanometer dimensions.

The main goal of this thesis was to study nanofluidic processes using TLFs as models, or tools, and to subtract information about natural systems plus deepen the understanding on physical chemical conditions. The presented work showed that foam films can be used as experimental models to understand the behavior of liquids in nano – sized confinement.

In the first part of the thesis, we studied the process of thinning of thin liquid films stabilized with the non – ionic surfactant n – dodecyl – β – maltoside ($\beta - C_{12}G_2$) with primary interest in interfacial diffusion processes during the thinning process dependent on surfactant concentration [64]. The surfactant concentration in the film forming solutions was varied at constant electrolyte (NaCl) concentration. The velocity of thin-

ning was analyzed combining previously developed theoretical approaches. Qualitative information about the mobility of the surfactant molecules at the film surfaces was obtained. We found that above a certain limiting surfactant concentration the film surfaces were completely immobile and they behaved as non – deformable, which decelerated the thinning process. This follows the predictions for Reynolds flow of liquid between two non – deformable disks.

A future project will be to change the interfacial properties of TLFs to asymmetrical systems where liquid flow between one solid and one liquid IF can be studied. Basic properties like the flow velocity and the interfacial mobility of such films known as wetting films will be studied. They seem to be promising models for investigating the processes of attachment between e.g. living cells and solid interfaces.

In the second part of the thesis, we designed a TLF nanofluidic system containing rod – like multivalent ions and compared this system to films containing monovalent ions. We presented first results which recognized for the first time the existence of an additional attractive force in the foam films based on the electrostatic interaction between rod – like ions and oppositely charged surfaces. We may speculate that this is an ion bridging component of the disjoining pressure. The results show that for films prepared in presence of spermidine the transformation of the thicker CF to the thinnest NBF is more probable as films prepared with NaCl at similar conditions of electrostatic interaction. This effect is not a result of specific adsorption of any of the ions at the fluid surfaces and it does not lead to any changes in the equilibrium properties of the CF and NBF. Our hypothesis was proven using the trivalent ion Y^{3+} which does not show ion bridging. The experimental results are compared to theoretical predictions and a quantitative agreement on the system's energy gain for the change from CF to NBF could be obtained.

A future project must include further detailed studies of the interactions in the films in presence of spermidine (e.g. measurement of the contact angles which are directly related to the strength of interactions). An important and interesting extension of the work would be experiments with the surface force apparatus because of the better defined geometry of the surfaces compared to those of the foam films.

In the third part of the work, the behavior of nanoparticles in confinement was investigated with respect to their impact on the fluid flow velocity. The particles altered the flow velocity by an unexpected high amount, so that the resulting changes in the dynamic viscosity could not be explained by a realistic change of the fluid viscosity. Only aggregation, flocculation and plug formation can explain the experimental results. The particle systems in the presented thesis had a great impact on the film interfaces

due to the stabilizer molecules present in the bulk solution. The Au system performed much better than the Fe_3O_4 system in terms of purity, so it would be useful to repeat measurements with Fe_3O_4 stabilized by the polymer. Such particles are available since very recently [102].

Finally, the location of the particles with respect to their lateral and vertical arrangement in the film was studied with advanced reflectivity and scattering methods. Neutron Reflectometry studies were performed to investigate the location of nanoparticles in the TLF perpendicular to the IF. For the first time, we study TLFs using grazing incidence small angle X – ray scattering (GISAXS), which is a technique sensitive to the lateral arrangement of particles in confined volumes. This work provides preliminary data on a lateral ordering of particles in the film.

The magnetic nanoparticles in films will have to be more extensively studied using Neutron Reflectometry. This method is exceptionally suitable for such studies since neutrons are sensitive to magnetic moments. The periodic arrangement of particles could induce a collective magnetic response to an external magnetic field. This could not only be detected and quantified via NR but also the polarization could create a rigid – like magnetic particle layer in the film. GISAXS is a promising tool to study more extensively the distribution of particles in TLFs. Open questions on the quantification of particles can be answered. The analysis tools can be amended and improved. New application of the foam films as a “matrix” for particles ordering and design of new materials with specific properties will be possible.

6 EXPERIMENTAL DETAILS

6.1 Solvents, Surfactants, Ions, Materials

6.1.1 Overview

H_2O	Elga Labwater, Germany
D_2O	> 99.96 %, Merck
Glycerol	99 %, Riedel de Haen/Sigma Aldrich
H_2SO_4	95 - 97 %, Sigma Aldrich
HCl	1 M, Merck
NaOH	1 M, Merck
Ethanol	99.8 %, for analysis, Merck
Mucasol®	Brand, Germany
PEI	50 wt % in aqu. sol., Sigma Aldrich
Fe_3O_4 particles: Iron (II, III) Oxide Nanosuspension - Magnetic Fluid	PlasmaChem, Berlin, Germany
Au particles	MPI - KGF [94]
NaCl	> 99.9 %, treated at 600°C for >5 h
Spermidine	> 98 %, Sigma Aldrich
$YCl_3 \cdot 6H_2O$	99.9 %, Sigma Aldrich
$\beta - C_{12}G_2$	≥ 99 %, Glycon, Germany
CTAB	> 99 %, Sigma Aldrich

6.1.2 Solvents

A water purification system (Elga Labwater, Germany) was used to purify the water (H_2O), the specific resistance of the water used was 18.2 MΩ cm. D_2O was used without further purification. To the solutions for NR and GISAXS experiments, 25 vol % of glycerol was added for an increase in viscosity.

6.1.3 Surfactants

N – Dodecyl β – Maltoside ($\beta - C_{12}G_2$) and cetyl trimethyl ammoniumbromide (CTAB) were used without further purification. The hydrophilic group of the surfactant $\beta - C_{12}G_2$ consists of two sugar rings connected via an ether bond as illustrated in Figure 6.1.

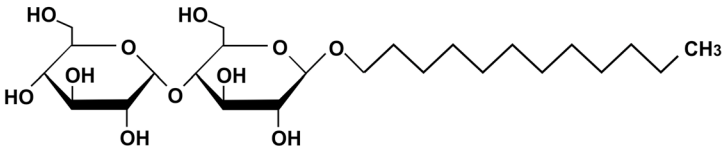

Figure 6.1 Molecular structure of n – dodecyl β – maltoside ($\beta - C_{12}G_2$)

6.1.4 Ions

Sodium chloride (NaCl) was purified by heat treatment at 600°C for at least 5 hours to remove surface – active contaminations.

Spermidine was used without further purification. It degenerates with time, therefore solutions containing spermidine were stored frozen and new solutions were frequently prepared. The pH – value of the spermidine solutions was adjusted by adding three times the amount of HCl than the respective concentration of spermidine.

Yttrium (III) chloride hexahydrate was used without further purification. The aqueous solutions containing YCl_3 showed a decrease of the pH value by several orders. The adjustment to the experimental value of pH 6.6 – 6.8 was performed by adding sodium hydroxide (NaOH).

6.1.5 Preparation of Solutions and Dispersions

All solutions were prepared by dilution and subsequent mixture of concentrated stock solutions containing surfactants or ions. The particles were added directly from the original sample in order to avoid aggregation caused by dilution to less concentrated stock solutions. The solutions and dispersions were prepared and stored in ultra clean glassware, in darkness (especially all particle dispersions), at room temperature, and for at least 12 hours but not longer than one week before usage.

The refractive index (n) of the bulk solutions was measured with an 'Abbe' refractometer (Carl Zeiss Jena, Germany, DDR) at 25°C. All the solutions with 0.2 M NaCl and β - $C_{12}G_2$ surfactant in different concentrations (between 10^{-6} M and 10^{-3} M)

resulted in a refractive index of n = 1.333. The value of n scattered only at the fourth decimal place, and thus does not influence the value for the calculated thickness (h).

The pH value of the solutions was measured with a Mettler Toledo, Five Easy desktop pH meter. The glass electrode was of the type LE409 (pH 0 - 14, 0 - 80 °C). Up to several hours was necessary for the pH of the solutions to attain equilibrium.

6.2 Methods

6.2.1 Microinterferometric Thin Liquid Film Analysis

The thinning process of foam films was monitored with an image enhanced optoelectronic device based on an Olympus IX50 microscope. In all the experiments, the temperature was kept constant at 23°C and controlled with an accuracy of ± 0.1°C. Additionally, the measurement temperature was adjusted to be equal to the room temperature and was kept constant with an accuracy of ± 0.5 °C. The atmosphere in the vessel is saturated with vapor of the respective solution. Two hours are allowed for reaching of equilibrium before starting measurements. An experimentally chosen equilibration time of ~10 min was allowed between each measurement.

For surfactant concentrations above 0.02 mM, the I(t) curves show considerable deviations when allowing less time for reaching equilibrium. Such curves tend to become very wavy, which indicates irregularities in thickness of the film interfaces. Concerning films from solutions with very low surfactant concentrations (≤ 0.02 mM), we found no substantial difference in the smoothness of the I(t) curves as a function of equilibration time.

The cells and the glassware were cleaned in a regular laboratory dishwasher and afterwards kept in a 50% mixture of sulfuric acid (H_2SO_4) and purified water over night. The glassware was rinsed afterwards ten times with purified water and dried in a separate ultra clean oven at 100°C.

In order to keep the contact angle in the cell capillary at $\theta = 0°$ for experiments with positively charge surfactants, the cell has been covered with a layer of the positive polyelectrolyte polyethyleneimine (PEI) for 1h in 0.5 M solution. Approximately two liters of 80°C purified water was aspirated through the capillary in order to remove residual polymer after experiments.

6.2.2 Neutron Reflectometry

The NR experiments were performed at Institute Laue – Langevin (ILL) in Grenoble, France at the dual mode reflectometer D17 [103] used in time – of – flight (TOF) mode. The double chopper system defines the time resolution and thus the wavelength range from 2 to 18 Å, giving a q – range for specular reflectivity of 0.004 – 4 $Å^{-1}$. The TOF experimental data $I(\lambda)$ was transformed with the software LAMP to $Z(q_z)$. LAMP (Large Array Manipulation Package) is an IDL based data reduction package written at the ILL and used on most of the ILL instruments as a tool for primary data inspection. The real space models for the SLD profiles of the film were observed using the software tool Parratt 1.6, which works with the χ^2 criteria in order to find the best possible fit [104].

6.2.3 GISAXS

The GISAXS measurements were taken at the „Deutsches Elektronen – Synchroton" (DESY), Hamburg. In the HASYLAB, the wiggler beamline BW4 was used with the 4.5 GeV positron source at the storage ring „DORIS III" [105].

The dimensions of the micro – focused X – ray beam were 20 µm x 40 µm (vertical x horizontal). Under the applied angle of incidence of $\alpha_i \approx 0.47°$ the beam creates a real footprint on the sample of about 3 – 4 mm length and 40 µm width. The distance between sample and detector was L_{SD} = 2.014 m. The dimensions of the aluminum frame (and film) were 25 mm x 11.25 mm used in horizontal orientation. Before the measurement, the frame was installed vertically enabling the thinning of the film. After reaching equilibrium film thickness, the cell with the film was tilted to horizontal orientation. After the precise alignment of the film to the required experimental geometry, the GISAXS measurement was started.

6.2.4 Tensiometry

The roughened platinum plate for the surface tension measurements was 20 mm long and 0.3 mm thick. Before each measurement the plate was spray rinsed first with purified water, then with ethanol and dried over the flame of a Bunsen burner. Then it was blown with nitrogen to cool off and after 10 min in the measurement chamber it was assumed that the measurement temperature was reached.

The tensiometer used in this work was a Krüss tensiometer K11 with an accuracy of ± 0.1 mN/m in Wilhelmy plate mode. During measurements, the solutions were kept in Polytetrafluorethen (PTFE) beakers. The PTFE beakers were cleaned before

usage in 3 % aqueous Mucasol® cleaning solution (Brand, Germany) for 15 min with ultrasound. They were rinsed ten times with purified water and dried in an ultra – clean oven at 100°C. The solutions were put in PTFE vessels with covers to prevent evaporation at least 30 min before the measurement for equilibration of the surface and the temperature; all experiments were performed at 25°C.

Between 5 and 10 single measurements were performed for each surfactant concentration dependent on the drift of the measured values. For calibration of the tensiometer, measurements of the purified lab water were repeatedly performed and the value for the outline of the plate adjusted in the range of several 100 micrometers (µm) so that the surface tension of pure water was 71.98 mN/m ± 0.1 mN/m.

6.2.5 TEM

The measurements in this work on the characterization of nanoparticles were performed on a TEM of type EM 912 Omega fabricated by Carl – Zeiss (Oberkochen, Germany). The resolution is given to be 0.37 nm (spot) and 0.20 nm (line). The acceleration voltage is 60 – 120 kV. Enlargement capacity is 80x – 500,000x (in 38 steps). The electron source is a lanthanum hexaboride (LaB6) cathode. The optical images are taken via a standard digital (CCD) camera. The vacuum system is a two step rotary vane pump, a turbomolecular pump, followed by an ion getter pump.

6.2.6 DLS

The instrument Zetasizer Nano ZS (Malvern Instruments Ltd., UK) was used to perform the measurements. The measurement time was set to 500s. For shorter measurement times, the determination of the size distribution of the particles and aggregates in the samples was not reproducible. The data analysis was performed using the Zetasizer software with standard operation procedures. The measurement cell was the folded capillary cell, developed by Malvern Instruments especially for the Zetasizer.

7 DEUTSCHE ZUSAMMENFASSUNG

Mit dem Heranwachsen der Nanotechnologie in den vergangenen zehn Jahren hat sich die Nanofluidik als Forschungsbereich etabliert und erfährt wachsende Aufmerksamkeit im wissenschaftlichen, sowie auch im industriellen Bereich. Nanofluidik befasst sich mit dem Fließverhalten von Flüssigkeiten in Nanometer kleinen Schlitzgeometrien und in direkter Nähe von Oberflächen. Im biomedizinischen Bereich, wo intrazelluläre Prozesse häufig komplexer, nanofluidischer Natur sind, wird vermehrt ein detailliertes Verständnis der Nanofluidik benötigt. Den Einfluss, den kleinste Teilchen (Kolloide) verschiedenster Form oder elektrischer Ladung auf die Kanäle und auf das Fließverhalten ausüben ist bei weitem nicht verstanden. Ebensowenig wie der Einfluss flexibler Oberflächen, oder der Einengung von Flüssigkeiten und Kolloiden in Schlitzgeometrien.

Eine systematische Untersuchung von nanofluidischen Prozessen erfordert passende experimentelle Modelle. In der vorliegenden Arbeit werden dünne flüssige Filme, hinsichtlich ihrer Funktionalität als nanofluidische Modelle untersucht. Die Filme sind aufgebaut wie die Hülle einer Seifenblase und die Grenzflächen zwischen Fluid und Gasphase stellen im nanofluidischen System die Wände des Kanals dar. Ihre Eigenschaften werden durch die Menge und Art der Moleküle, die vom Fluid adsorbieren bestimmt.

Wir untersuchten die Fließgeschwindigkeit des Fluids aus dem dünnen Film, abhängig von der Konzentration der filmstabilisierenden Tensidmoleküle n – Dodecyl β – D – Maltoside ($\beta - C_{12}G_2$) bei einer konstanten Elektrolytkonzentration von 0.2 mM NaCl. Mit einem theoretischen Modell konnten wir das Dünnungsverhalten nachzeichnen. Es wurde eine kritische Tensidkonzentration gefunden, unter der die Oberflächen lateral mobil sind und über der sie sich wie fest verhalten. Dadurch konnten wir Aufschluss darüber erlangen, wie die Oberfläche des Films unter verschiedenen Bedingungen geschaffen ist, und das in Bezug zur Verteilungsdichte der Moleküle an den Oberflächen setzen.

Im weiteren untersuchten wir komplexere, nanofluidische Systeme, wobei wir zum einen den Elektrolyten durch ~ 1 nm lange, stäbchenförmige, multivalent geladene Spermidin - Moleküle ersetzten. Im Rahmen der Untersuchungen konnte eine deutliche Veränderung der Stabilität zwischen Filmen mit und ohne Stäbchen festgestellt werden. Die Filme, mit dem monovalenten NaCl, blieben viel länger in dem metastabilen „Common Film“ (CF) Zustand als die Filme, die eine vergleichbare Konzentration von

Spermidine beinhalteten. Die Ergebnisse deuteten auf eine zusätzliche Anziehungskraft durch Brückenbildung zwischen zwei geladenen Oberflächen durch gegensätzlich geladene Stäbchenförmige Moleküle hin. Es konnte gezeigt werden, dass dieser Effekt weder ein Ergebnis von spezifischer Ionenadsorption an die Filmoberfläche war, noch ein Unterschied in den Gleichgewichtszuständen von den Dicken der CFs und der Newton Black Films (NBFs) hervorrief, was auf die korrekte Annahme der Ionenstärke in der Lösung schließen ließ. Auch in Versuchen mit ebenfalls trivalenten Ionen YCl_3 wurde festgestellt, dass keinerlei vergleichbare Überbrückungseffekte auftreten. Die Ergebnisse wurden mit theoretischen Simulationen verglichen und es wurde eine quantitative Übereinstimmung gefunden bezüglich der Größe des Systeminternen Energiegewinns durch den Überbrückungseffekt.

Eine weitere dynamische Untersuchung des Fließverhaltens von Fluiden mit in Schlitzgeometrien eingeengten Kolloiden wurde durchgeführt. Für zwei verschiedene Arten von Nanopartikeln (Fe_3O_4 stabilisiert mit Oleinsäure und polymerstabilisierte Goldpartikel) wurde eine Verlangsamung der Fließgeschwindigkeit festgestellt. Mit einem theoretischen Modell konnte das Fließverhalten nur für enorm erhöhte Viskositätswerte des Fluids erklärt werden. Die Viskositätserhöhung wurde mit Partikelaggregaten, die den Ausfluss behindern, erklärt und diskutiert, unter der Annahme eines nicht - Newtonischen Fließverhaltens der Dispersionen in Schlitzgeometrien.

Gleichermaßen wurde die strukturelle Anordnung der Partikel in den Filmen hinsichtlich ihrer vertikalen und lateralen Verteilung untersucht. In dieser Arbeit werden vorläufige Ergebnisse präsentiert, die noch weiteren Studien bedürfen. Mit Neutronenreflexion sollte die Anordnung der Partikel orthogonal zur Oberfläche im Film analysiert werden. Eine qualitative Analyse lässt schließen, dass bei einer höheren Konzentration von Partikeln in Lösung, sich auch eine erhöhte Konzentration von Partikeln im dünnen Film befindet.

Zum ersten Mal wurden dünne flüssige Filme mit Kleinwinkelröntgenstreuung unter streifendem Einfall (GISAXS) analysiert. Mit Hilfe dieser Methode sollte eine laterale Anordnung der Partikel im Film untersucht werden. Mit Hilfe der rechnergestützten Analyse konnte die Aussage getroffen werden, dass ~ 6 nm große Teilchen in ~ 43 nm Abstand sich im Film befinden.

Zusammenfassend können sich mit dieser Arbeit die dünnen flüssigen Filme als eine wichtige Kernmethode der Untersuchung von nanofluidischen Prozessen, wie sie häufig in der Natur vorkommen, behaupten. Weiterführende Untersuchungen werden die noch bestehenden Fragen und Unklarheiten in der Zukunft klären können.

LITERATURE

1. Ducrée, J., *Microfluidics*. (expected in Springer: Berlin, 2010, www.myfluidix.com).
2. Mijatovic, D.; Eijkel, J. C. T.; van den Berg, A., Technologies for Nanofluidic Systems: Top-Down vs. Bottom-Up - A Review. *Lab Chip* **2005,** *5* (5), 492 - 500.
3. Eijkel, J. C. T.; Berg, A., Nanofluidics: What Is It And What Can We Expect From It? *Microfluid. Nanofluid.* **2005,** *1* (3), 249 - 267.
4. Israelachvili, J. N., *Intermolecular & Surface Forces*. Academic Press: London, 1992.
5. Atkins, P.; de Paula, J., *Physical Chemistry*. Oxford University Press: New York, 2002.
6. Langmuir, I., The Constitution and Fundamental Properties of Solids and Liquids - Part I Solids. *JACS* **1916,** *38*, 2221 - 2295.
7. Szyskowski, B. V., Experimentelle Studien über kapillare Eigenschaften der Wässerigen Lösungen von Fettsäuren. *Z. Phys. Chem.* **1908,** *64*, 385 - 414.
8. Binks, B. P., Particles as Surfactants - Similarities and Differences. *Curr. Opin. Colloid Interface Sci.* **2002,** *7*.
9. Holmberg, K., Natural Surfactants. *Curr. Opin. Colloid Interface Sci.* **2001,** *6* (2), 148 - 159.
10. Stubenrauch, C., Sugar Surfactants - Aggregation, Interfacial, and Adsorption Phenomena. *Curr. Opin. Colloid Interface Sci.* **2001,** *6*, 160 - 170.
11. Hill, K.; Rybinski, W.; Stoll, G., Ed. *Alkyl Polyglycosides: Technology, Properties, and Applications*; Wiley-VCH: Berlin, 1997.
12. Claesson, P.; Stubenrauch, C.; Krastev, R.; Johansson, I., Thin Film and Foam Properties of Sugar - Based Surfactants. In *Sugar-Based Surfactants: Fundamentals and Applications*, Ruiz, C., Ed. CRC Press: Boca Raton (USA), 2008; Vol. 143, pp 105 - 152, Chapter 4.
13. Stubenrauch, C.; Schlarmann, J.; Strey, R., A Disjoining Pressure Study of n-Dodecyl-beta-D-Maltoside Foam Films. *Phys. Chem. Chem. Phys.* **2002,** *4*, 4504 - 4513.
14. Muruganathan, R. M.; Krustev, R.; Ikeda, N.; Muller, H.-J., Temperature Dependence of the Gas Permeability of Foam Films Stabilized by Dodecyl Maltoside. *Langmuir* **2003,** *19*, 3062 - 3065.
15. Stubenrauch, C.; Cohen, R.; Exerowa, D., A pH-Study of n-Dodecyl-beta-D-Maltoside Foam Films. *Langmuir* **2007,** *23* (4), 1684 - 1693.
16. Muruganathan, R. M.; Krustev, R.; Muller, H.-J.; Möhwald, H.; Kolaric, B.; von Klitzing, R., Foam Films Stabilized by Dodecyl Maltoside. 1. Film Thickness and Free Energy of Film Formation. *Langmuir* **2004,** *20* (15), 6352 - 6358.
17. Exerowa, D., Effect of Adsorption, Ionic Strength and pH on Potential of Diffuse Electric Layer. *Kolloid Z Z Polym* **1969,** *232* (1), 703 - 710.
18. Kolarov, T.; Yankov, R. A.; Esipova, N.; Exerowa, D.; Zorin, Z., Charge Reversal At The Air - Water - Interface As Inferred From The Thickness Of Foam Films. *Colloid. Polym. Sci.* **1993,** *271* (5), 519 - 520.
19. Derjaguin, B. V.; Abrikosova, I. I.; Lifshitz, E. M., Direct Measurement of Molecular Attration Between Solids Separated by a Narrow Gap. *Q Rev Chem Soc* **1956,** *10* (3), 295 - 329.
20. Sheludko, A., Thin Liquid Films. *Adv. Colloid Interface Sci.* **1967,** *1*, 391 - 464.
21. Hamaker, H., The London - Van Der Waals Attraction Between Spherical Particles. *Physica* **1937,** *4*, 1058 - 1072.
22. Dzyaloshinskii, I. E.; Lifshitz, E. M.; Pitaevskii, L. P., *Zh. Eksp. Teor. Fiz.* **1959,** *37*, 229.
23. Derjaguin, B. V.; Landau, L., On the Repulsive Forces between Charged Colloid Particles and on the Theory of Slow Coagulation and Stability of Lyophobe Sols. *Trans. Faraday Soc.* **1940,** *36*, 203 - 211.

24. Verwey, E. J. W.; Overbeek, J. T. G., *The Theory of the Stability of Liophobic Colloids*; Elsevier: Amsterdam, 1948.

25. Exerowa, D.; Kruglyakov, P. M., Ed. *Foam and Foam Films - Theory, Experiment, Application*. Elsevier: Amsterdam, 1998; Studies in Interface Science Vol. 5.

26. Farajzadeh, R.; Krastev, R.; Zitha, P. L. J., Foam Film Permeability: Theory and Experiment. *Adv. Colloid Interface Sci.* **2008,** *137* (1), 27 - 44.

27. Ivanov, I. B., Ed. *Thin Liquid Films: Fundamentals and Applications*; Dekker: New York, 1988; Surfactant Science Series Vol. 29, p 1126.

28. Prud'homme, R. K.; Khan, S. A., Ed. *Foams: Theory, Measurements, and Applications*; Marcel Dekker, Inc.: New York, 1996; Surfactant Science Series Vol. 57, p 596.

29. Bergeron, V., Forces and Structure in Thin Liquid Soap Films. *J. Phys. Condens. Matter* **1999,** *11*, R215 - R238.

30. von Klitzing, R.; Muller, H.-J., Film Stability Control. *Curr. Opin. Colloid Interface Sci.* **2002,** *7* (1 - 2), 42 - 49.

31. Coons, J.; Halley, P.; McGlashan, S.; Tran-Cong, T., A Review of Drainage and Spontaneous Rupture in Free Standing Thin Films with Tangentially Immobile Interfaces. *Adv. Colloid Interface Sci.* **2003,** *105*, 3 - 62.

32. Manev, E. D.; Nguyen, A. V., Effects of Surfactant Adsorption and Surface Forces on Thinning and Rupture of Foam Liquid Films. *Int. J. Miner. Process.* **2005,** *77*, 1 - 45.

33. Warszynski, P.; Papastavrou, G.; Wantke, K.; Mohwald, H., Interpretation of Adhesion Force between Self-Assembled Monolayers Measured by Chemical Force Microscopy. *Colloid Surface A* **2003,** *214* (1 - 3), 61 - 75.

34. Becker, T.; Mugele, F., Nanofluidics: Viscous Dissipation in Layered Liquid Films. *Phys. Rev. Let.* **2003,** *91* (16), 166104-1 - 166104-4.

35. Klapp, S. H. L.; Qu, D.; von Klitzing, R., Long-Range Interactions between Soft Colloidal Particles in Slit-Pore Geometries. *J. Phys. Chem. B* **2007,** *111* (6), 1296 - 1303.

36. Frankel, S. P.; Mysels, K. J., Simplified Theory of Reflectometric Thickness Measurement of Structured Soap and Related Films. *J Appl Phys* **1966,** *37* (10), 3725 - 3728.

37. Kashchiev, D.; Exerowa, D., Nucleation Mechanism of Rupture of Newtonian Black Films. I. Theory. *J. Colloid Interface Sci.* **1980,** *77*, 501 - 511.

38. Exerowa, D.; Balinov, B.; Kashchiev, D., Nucleation Mechanism of Rupture of Newtonian Black Films : II. Experiment. *J. Colloid Interface Sci.* **1983,** *94*, 45 - 53.

39. Vrij, A., Light Scattering by Soap Films. *J. Colloid Interface Sci.* **1964,** *19* (1), 1 - 27.

40. Nierstrasz, V.; Frens, G., Marginal Regeneration in Thin Vertical Liquid Films. *J. Colloid Interface Sci.* **1998,** *207* (2), 209 - 217.

41. Vrij, A., Possible Mechanism for Spontaneous Rupture of Thin Free Liquid Films. *Discuss Faraday Soc* **1966,** (42), 23 - 33.

42. Vrij, A.; Overbeek, J. T. G., Rupture of Thin Liquid Films due to Spontaneous Fluctuations in Thickness. *JACS* **1968,** *90* (12), 3074 - 3078.

43. Stefan, J., Versuche über die Scheinbare Adhäsion. *Sitzungsber. Kaiserl. Akad. Wiss. Math. Naturwiss. Cl.* **1874,** *II* (69), 713 - 735.

44. Reynolds, O., On the Theory of Lubrication and Its Application to Mr. Beauchamp Tower's Experiments, Including an Experimental Determination of the Viscosity of Olive Oil. *Philos. Trans. R. Soc. London* **1886,** *177*, 157 - 234.

45. Angarska, J.; Manev, E. D., Effect of Surface Forces and Surfactant Adsorption on the Thinning and Critical Thickness of Foam Films. *Colloids Surf., A* **2001,** *190*, 117 - 127.

46. Langevin, D.; Sonin, A. A., Thinning of Soap Films. *Adv. Colloid Interface Sci.* **1994,** *51*, 1 - 27.

47. Eliseeva, O.; Fokkink, R.; Besseling, N.; Koopal, L., Thinning of Wetting Films Formed from Aqueous Solutions of Non-Ionic Surfactant. *J. Colloid Interface Sci.* **2006,** *301*, 210 - 216.

48. Németh, Z.; Sedev, R.; Ivanova, R.; Kolarov, T.; Exerowa, D., Thinning of Microscopic Foam Films Formed from a Mixture of Bovine Serum Albumin and Pluronic L62. *Colloids Surf., A* **1999,** *149*, 179 - 184.

49. Angarska, J.; Stubenrauch, C.; Manev, E. D., Drainage of Foam Films Stabilized with Mixtures of Non-Ionic Surfactants. *Colloids Surf., A* **2007,** *309* (1 - 3), 189 - 197.

50. Manev, E. D.; Nguyen, A. V., Critical Thickness of Microscopic Thin Liquid Films. *Adv. Colloid Interface Sci.* **2005,** *114*, 133 - 146.

51. Coons, J.; Halley, P.; McGlashan, S.; Tran-Cong, T., Bounding film drainage in common thin films. *Colloids Surf., A* **2005**.

52. Tombacz, E.; Bica, D.; Hajdu, A.; Illes, E.; Majzik, A.; Vekas, L., Surfactant Double Layer Stabilized Magnetic Nanofluids for Biomedical Application. *J. Phys. Condens. Matter* **2008,** *20* (20), 204103 6pp.

53. Wasan, D.; Nikolov, A. D., Thin Liquid Films Containing Micelles or Nanoparticles. *Curr. Opin. Colloid Interface Sci.* **2008,** *13* (3), 128 - 133.

54. Vassilieff, C. S.; Nickolova, B. N.; Manev, E. D., Thinning of Foam Films of Micellar Surfactant Solutions. *Colloid. Polym. Sci.* **2008,** *286* (4), 475 - 480.

55. Asnacios, A.; Espert, A.; Colin, A.; Langevin, D., Structural Forces in Thin Films made from Polyelectrolyte Solutions. *Phys. Rev. Let.* **1997,** *78* (26), 4974 - 4977.

56. Kristen, N.; von Klitzing, R., Effect of Polyelectrolyte/Surfactant Combinations on the Stability of Foam Films. *Soft Matter* **2010,** *6* (5), 849 - 861.

57. Sedev, R.; Kolarov, T.; Exerowa, D., Surface Forces in Foam Films from ABA Block Copolymer: A Dynamic Method Study. *Colloid. Polym. Sci.* **1995,** *273*, 906 - 911.

58. Horozov, T. S., Foams and Foam Films Stabilised by Solid Particles. *Curr. Opin. Colloid Interface Sci.* **2008,** *13* (3), 134 - 140.

59. Bergeron, V.; Cooper, P.; Fischer, C.; Giermanska-Kahn, J., Polydimethylsiloxane (PDMS)-Based Antifoams. *Colloids Surf., A* **1997,** *122*, 103 - 120.

60. Denkov, N., Mechanisms of Foam Destruction by Oil-Based Antifoams. *Langmuir* **2004,** *20* (22), 9463 - 9505.

61. Sethumadhavan, G. N.; Nikolov, A. D.; Wasan, D., Stability of Liquid Films Containing Monodisperse Colloidal Particles. *J. Colloid Interface Sci.* **2001,** *240*, 105 - 112.

62. Denkov, N. D.; Yoshimura, H.; Nagayama, K.; Kouyama, T., Nanoparticle Arrays in Freely Suspended Vitrified Films. *Phys. Rev. Let.* **1996,** *76* (13), 2354 - 2357.

63. Akbulut, M.; Alig, A.; Min, Y.; Belman, N.; Reynolds, M., Forces between Surfaces across Nanoparticle Solutions: Role of Size, Shape, and Concentration. *Langmuir* **2007,** *23*, 3961 - 3969.

64. Stöckle, S.; Blecua, P.; Möhwald, H.; Krastev, R., Dynamics of Thinning of Foam Films Stabilized byn-Dodecyl-β-maltoside. *Langmuir* **2010,** *26* (7), 4865 - 4872.

65. Toca-Herrera, J.-L. Wechselwirkungskräfte und Struktur in Phospholipid-Schaumfilmen. GCA-Verlag, 2000.

66. Müller-Buschbaum, P., A basic Introduction to Grazing Incidence Small Angle X-Ray Scattering. In *Applications of Synchrotron Light to Noncrystalline Diffraction in Materials and Life Sciences*, Ezquerra, T. A.; García-Gutiérrez, M.; Nogales, A.; Gómez, M., Eds. Springer Berlin Heidelberg, 2009; Vol. 776, pp 61 - 90, Chapter 3.

67. Naudon, A.; Thiaudiere, D., Grazing-incidence Small-Angle Scattering. Morphology of Deposited Clusters and Nanostructure of Thin Films. *J. Appl. Crystallogr.* **1997,** *30* (2, Part 5), 822 - 827.

68. Aksenenko, E. V., Software Tools to Interpret the Thermodynamics and Kinetics of Surfactant Adsorption. In *Surfactants: Chemistry, Interfacial Properties, Applications*, Möbius, D.; Miller, R.; Fainerman, V. B., Eds. Elsevier: 2001; Vol. 13, pp 619 - 648, 7.

69. Stubenrauch, C.; Miller, R., Stability of Foam Films and Surface Rheology: An Oscillating Bubble Study at low Frequencies. *J. Phys. Chem. B* **2004,** *108* (20), 6412 - 6421.

70. Santini, E.; Ravera, F.; Ferrari, M.; Stubenrauch, C., A Surface Rheological Study of non-Ionic Surfactants at the Water–Air Interface and the Stability of the Corresponding Thin Foam Films. *Colloids Surf., A* **2007,** *298*, 12 - 21.

71. Radoev, B.; Dimitrov, D.; Ivanov, I. B., Hydrodynamics of Thin liquid Films Effect of the Surfactant on the Rate of Thinning. *Colloid. Polym. Sci.* **1974,** *252*, 50 - 55.

72. Ivanov, I. B., Effect of Surface Mobility On The Dynamic Behaviour Of Thin Liquid-Films. *Pure Appl. Chem.* **1980,** *52* (5), 1241 - 1262.

73. Peters, R.; Beck, K., Translational Diffusion in Phospholipid Monolayers Measured by Fluorescence Microphotolysis. *Proc. Nat. Acad. Sci. U.S.A.-Biol. Sci.* **1983,** *80* (23), 7183 - 7187.

74. Jachimska, B.; Warszynski, P.; Malysa, K., Effects of Motion in n-hexanol Solution on the Lifetime of Bubbles at the Solution Surface. *Prog. Colloid Polym. Sci.* **2000,** *116*, 120 - 128.

75. Jachimska, B.; Warszynski, P.; Malysa, K., Influence of Adsorption Kinetics and Bubble Motion on Stability of the Foam Films Formed at n-Octanol, n-Hexanol and n-Butanol Solution Surface. *Colloids Surf., A* **2001,** *192* (1-3), 177 - 193.

76. Zhang, L.; Somasundraran, P.; Maltesh, C., Adsorption of n-dodecyl-beta-D-maltoside on Solids. *J. Colloid Interface Sci.* **1997,** *191* (1), 202 - 208.

77. Noy, A.; Park, H. G.; Fornasiero, F.; Holt, J., Nanofluidics in Carbon Nanotubes. *Nano Today* **2007,** *2* (6), 22 - 29.

78. Espert, A.; von Klitzing, R.; Poulin, P.; Colin, A.; Zana, R.; Langevin, D., Behavior of Soap Films Stabilized by a Cationic Dimeric Surfactant. *Langmuir* **1998,** *14* (15), 4251 - 4260.

79. Márquez-Beltrán, C.; Langevin, D., Electrostatic Effects in Films Stabilised by Non-Ionic Surfactants. *J. Colloid Interface Sci.* **2007,** *312* (1), 47 - 51.

80. Schelero, N.; von Klitzing, R., Ion-specific Effects on Stability and Interactions in Thin Aqueous Films. *7th Liquid Matter Conference* **2008**.

81. Toca-Herrera, J.-L.; Muller, H.-J.; Krustev, R.; Exerowa, D., Influence of Na+, Ca2+ on the Thickness and Free Energy of DMPC Foam Films. *Colloids Surf., A* **1998,** *144*, 319 - 326.

82. Angarska, J.; Tachev, K.; Kralchevsky, P.; Mehreteab, A.; Broze, G., Effects of Counterions and Co-ions on the Drainage and Stability of Liquid Films and Foams. *J. Colloid Interface Sci.* **1998,** *200* (1), 31 - 45.

83. Mileva, E.; Exerowa, D.; Tchoukov, P., Black Dots as a Detector of Self-Assembly in Thin Liquid Films. *Colloids Surf., A* **2001,** *186*, 83 - 92.

84. Kimberly, M.; Goldstein, J., Determination of pK, Values and Total Proton Distribution Pattern of Spermidine by Carbon- 13 Nuclear Magnetic Resonance Titrations. *Anal. Chem.* **1981,** *53* (6), 789 - 793.

85. Schulze-Schlarmann, J.; Buchavzov, N.; Stubenrauch, C., A Disjoining Pressure Study of Foam Films Stabilized by Tetradecyl Trimethyl Ammonium Bromide C14TAB. *Soft Matter* **2006,** *2* (7), 584 - 594.

86. May, S.; Iglic, A.; Rescic, J.; Maset, S.; Bohinc, K., Bridging Like-Charged Macroions Through Long Divalent Rodlike Ions. *J. Phys. Chem. B* **2008,** *112* (6), 1685 - 1692.

87. Maset, S.; Bohinc, K., Orientations of Dipoles Restricted by Two Oppositely Charged Walls. *J. Phys. A: Math. Theor.* **2007,** *40* (39), 11815 - 11826.

88. Exerowa, D., Foam and wetting films: electrostatic and steric stabilization. *Adv. Colloid Interface Sci.* **2003,** *104* (1-3), 1-24.

89. Bergeron, V., Disjoining Pressures and Film Stability of Alkyltrimethylammonium Bromide Foam Films. *Langmuir* **1997,** *13*, 3474 - 3482.

90. Bohinc, K.; Iglic, A.; May, S., Interaction Between Macroions Mediated by Divalent Rod-Like Ions. *Europhys. Lett.* **2004,** *68* (4), 494 - 500.

91. Teif, V., Ligand-Induced DNA Condensation: Choosing the Model. *Biophysical Journal* **2005,** *89* (4), 2574 - 2587.

92. Bloomfield, V., DNA Condensation by Multivalent Cations. *Biopolymers* **1998,** *44* (3), 269 - 282.

93. Hribar, B.; Vlachy, V., Evidence of Electrostatic Attraction between Equally Charged Macroions Induced by Divalent Counterions. *J. Phys. Chem. B* **1997,** *101* (18), 3457 - 3459.

94. Edwards, E.; Chanana, M.; Wang, D.; Möhwald, H., Stimuli-Responsive Reversible Transport of Nanoparticles Across Water/Oil Interfaces. *Angew. Chem. Int. Ed.* **2008,** *120* (2), 326 - 329.

95. Ha, T. H.; Kim, D. K.; Choi, M., Influence of Poly(ethylenimine) on the Monolayer of Oleic Acid at the Air/Water Interface. *J. Colloid Interface Sci.* **2000,** *226* (1), 98 - 104.

96. Liu, C.; Shan, Y.; Zhu, Y.; Chen, K., Magnetic Monolayer Film of Oleic Acid-Stabilized Fe_3O_4 Prticles Fabricated via Langmuir-Blodgett Technique. *Thin Solid Films* **2009,** *518* (1), 324 - 327.

97. Kwon, C.-W.; Yoon, T.-S.; Yim, S.-S.; Park, S.-H.; Kim, K.-B., The effect of Excess Surfactants on the Adsorption of Iron Oxide Nanoparticles During a Dip-Coating Process. *J. Nanopart. Res.* **2009,** *11* (4), 831 - 839.

98. Rosenson, R.; McCormick, A.; Uretz, E., Distribution of Blood Viscosity Values and Biochemical Correlates in Healthy Adults. *Clin Chem* **1996,** *42* (8), 1189 - 1195.

99. Carn, F.; Colin, A.; Pitois, O.; Vignes-Adler, M. l.; Backov, R. n., Foam Drainage in the Presence of Nanoparticle−Surfactant Mixtures. *Langmuir* **2009,** *25* (14), 7847 - 7856.

100. Krastev, R.; Mishra, N. C.; Gutberlet, T., Neutron Reflectivity from Black Foam Films. Part 2. *HMI Interne Z.* **2003**.

101. Penfold, J.; Staples, E.; Tucker, I.; Thomas, R.; Woodling, R.; Dong, C., The Structure of Mixed Nonionic Surfactant Monolayers at the Air-Water Interface: The Effects of Different Alkyl Chain Lengths. *J. Colloid Interface Sci.* **2003,** *262* (1), 235 - 242.

102. Chanana, M.; Jahn, S.; Georgieva, R.; Lutz, J.-F. o.; Bäumler, H.; Wang, D., Fabrication of Colloidal Stable, Thermosensitive, and Biocompatible Magnetite Nanoparticles and Study of Their Reversible Agglomeration in Aqueous Milieu. *Chem. Mater.* **2009,** *21* (9), 1906 - 1914.

103. Cubitt, R.; Fragneto, G., D17: The New Reflectometer at the ILL. *Appl Phys A-Mater* **2002,** *74*, S329 - S331.

104. Braun, C. *Parratt32 Fitting Routine for Reflectivity Data, Hahn-Meitner-Institut, Berlin*, 1997–1999.

105. Roth, S. V.; Döhrmann, R.; Dommach, M.; Kuhlmann, M.; Kröger, I.; Gehrke, R.; Walter, H.; Schroer, C.; Lengerler, B.; Müller-Buschbaum, P., Small-Angle Options of the Upgraded Ultrasmall-Angle X-Ray Scattering Beamline BW4 at HASYLAB. *Rev. Sci. Instr.* **2006,** *77*, 1 - 7.